Final Progress Report

Lean and Agile Precision Manufacturing Systems

Office of Naval Research
Grant No. N00014-95-1-G039

Submitted to:

Dr. Lawrence C. Schuette
Naval Research Laboratory
4555 Overlook Avenue, S.W.
Code 5707.5
Washington D.C. 20375-5337
schuette@enews1.nrl.navy.mil

Reported by:

Professor Alexander H. Slocum
Department of Mechanical Engineering
Massachusetts Institute of Technology
Room 3-445
77 Massachusetts Avenue
Cambridge, MA 02139-4307
slocum@mit.edu

DISTRIBUTION STATEMENT A
Approved for Public Release
Distribution Unlimited

20021112 056

1. Introduction

The primary goal of this research was to investigate how manufacturing activities could be configured so as to enable them to be lean (e.g., minimal inventory and set-up required) and agile (e.g., ability to respond rapidly and with minimal effort).

Accordingly, three areas of focus were identified, and in summary:

- *Precision fixturing:* Although many have studied fixturing, and the results in many cases have been improved modular fixturing systems, there remains significant need for greater precision at less cost. Accordingly, we chose to develop modular kinematic couplings, which can have micron and better precision, including design spreadsheets to enable them to be rapidly customized for particular applications.
- *Machine Design:* There is no shortage of innovative new machines, and one area that has received considerable interest is hexapods (Parallel Kinematic Machines or PKMs); however, our own experience with a hexapod we obtained with an NSF grant showed that they are not the cure-all for manufacturing that some had hoped. As a result, we studied their fundamental performance issues and created algorithms for analyzing machine performance. This led us to the design of a hybrid machine, which seems to provide the best compromise performance.
- *Machine Tool Spindles:* Working with the Mechanicsburg manufacturing equipment rebuilding depot, we developed a hydrostatic spindle as a retrofit for an existing large machine; however, we found that it is best of Depots to either utilize existing commercial technology, or that a company looking to develop (and support) new products should be a partner in such activities.

These areas are discussed in more detail below. Copies of resulting journal articles published and submitted for publication are attached to this report. Noted below are instances where the research began under the auspices of this grant, and then continued afterwards with support from other projects or with the PI's discretionary funds. The result is that we have been able to significantly leverage our research funds that provide a great deal more value for the ONR. Accordingly this final report is submitted at a time when all the work has been finally completed.

2. Precision Fixturing

For the past 15 years, we have been using three-groove kinematic couplings, which make contact at three sets of two points each between two bodies, to achieve fixturing repeatability on the micron and better level. For this project we assembled the knowledge we had, and added updates to the spreadsheet-based analysis programs. Then we added new designs for applications to fixturing robots and heavy pallets so they could be rapidly changed. This resulted in several fundamental journal publications that have significantly advanced the state of the art:

- M. Culpepper, "Design of Quasi-kinematic Couplings", submitted to *Journal of the International Societies for Precision Engineering and Nanotechnology*, June 2002
- M. Culpepper, A. Slocum, F. Shaikh, "Quasi-kinematic Couplings for Low-cost Precision Alignment of High-Volume Assemblies", submitted to *ASME Journal of Mechanical Design*, Sept. 2002
- R. Vallance, C. Morgan, A. Slocum, "Precisely Positioning Pallets in Multi-Station Assembly Systems", submitted to *Journal of the International Societies for Precision Engineering and Nanotechnology*, August 2002

This knowledge is now all contained in a comprehensive public access website www.kinematiccouplings.org which we continue to maintain. In addition, Dr. Martin Culpepper, who did his doctoral research in the laboratory at the time of this grant, is now an assistant professor at MIT and he is working with Dan Gearing of the DLA to develop specific application kinematic couplings for application in rapid fixturing for the DLA.

3. Machine Design

We had previously acquired a Hexel Corp. hexapod machine tool under an NSF grant, and we found that its performance was not much better than a traditional machine; however, the hexapod had a very small effective work volume. In addition, it suffered from surface finish problems that seemed to be caused by reversal motions required of the struts in order for the tool point to follow simple paths (such as a straight line or a plane). Accordingly, we analyzed just the kinematics of motion, and found that fundamentally, the complex geometry created the need for complex reversing moves amongst the actuators. Whenever an actuator reverses, there is a transition from static to dynamic friction and this force impulse can disrupt systems with modest compliance. The long thin struts of a hexapod, which are required to enable them to move fast, are such members. We accordingly used the new methods we developed for analyzing PKMs to also develop a concept for a hybrid machine and both are described in the journal article:[1]

- Son, S., Sarma, S., Slocum, A., "A Hybrid 5-Axis CNC Milling Machine", submitted to *Journal of the International Societies for Precision Engineering and Nanotechnology*, Sept. 2002.

4. Machine Tool Spindles

We worked with Bruce Davie (Defense Supply Center Richmond, Maintenance Depot Mechanicsburg) to see if we could retrofit a large planer mill with a hydrostatic spindle that would enable the machine top to also function as a large precision grinding machine. Dr. Kevin Wasson, who is now at Hardinge Inc. and in charge of their hydrostatic spindle program, which is where, all the spindle knowledge resides, designed the spindle and we had it manufactured and delivered to Mechanicsburg along with a 20 HP Fanuc spindle motor and controller. The spindle was initially activated and readied for use, but another project delayed its implementation. After several months, when it was finally installed, a few cuts were made, but then the spindle seized. It is inconclusive as to what happened and from this point on, we believe that the Depot should work with Hardinge Inc. to repair the spindle and bring it to commercial status.

---

[1] Note that this research continued after the official end date of this grant; however, since it was started by the grant, it was determined that we should submit this final report with the final results that we achieved. Note that Daewoo Corp. funded the development of the hybrid machine. Contact Prof. Sanjay Sarma at sesarma@mit.edu for more details.

We also investigated the potential for casting self-compensating hydrostatic bearings such that with simple ID and OD boring and turning operations respectively, hydrostatic radial support bearings could be created. These could be used for example as support bearings for large shafts or in particular quills for large boring mills. This effort was highly successful as is documented in the journal article that evolved from Dr. Kotilainen's Ph.D. thesis on this topic, where the manufacturing and design knowledge resides with Hardinge Inc.[2]

- Kotilainen, M., Slocum, A. "Manufacturing of Cast Monolithic Hydrostatic Journal Bearings", *Journal of the International Societies for Precision Engineering and Nanotechnology*, Vol. 25 (2001), pp. 235-244.

---

[2] For all hydrostatic enquiries, contact Dan Soroka, Hardinge, Inc., One Hardinge Drive, R&E, Elmira, NY 14902 dsoroka@hardinge.com (607) 734-2281 x2423

Submitted to "Precision
Engineering"
Journal of the ASPE

Design of Quasi-Kinematic Couplings

Martin L. Culpepper*

Room 3-449b
MIT Department of Mechanical Engineering
77 Massachusetts Avenue
Cambridge, MA 02139

Abstract

A quasi-kinematic coupling (QKC) is an alignment interface that can be used to make low-cost assemblies with sub-micron precision and/or sealing contact. Unlike kinematic couplings that rely on point contacts formed by mating balls in v-grooves, quasi-kinematic couplings are based on arc contacts formed by mating three balls with three axisymmetric grooves. Though a quasi-kinematic coupling is technically not an exact constraint coupling, proper design of the contacts can produce a weakly over constrained coupling that emulates an exact constraint coupling. This paper covers the practical design of quasi-kinematic couplings and derives the theory that predicts quasi-kinematic coupling stiffness. A metric of over constraint is presented and used to develop recommended practices for minimizing the over constraint in quasi-kinematic couplings. Experimental results are provided to show that quasi-kinematic couplings can provide repeatability (¼ micron) that is comparable to exact constraint couplings.

Keywords: Kinematic coupling, quasi-kinematic coupling, plastic deformation, exact constraint, fixture, repeatability, stiffness, assembly, photonics, automotive assembly, over constraint, precision optics

---

1. Introduction

1.1. Motivation

The need to improve performance has forced designers to tighten alignment tolerances for next generation assemblies. Where tens of microns were once sufficient, nanometer/micron level alignment tolerances are becoming common. Examples can be found in automotive engines, precision optics and photonic assemblies. Unfortunately, the new alignment requirements are beyond the practical capability (~ 5 microns) of most low-cost alignment technologies. The absence of a low-cost, sub-micron coupling has motivated the development of a new class of coupling interface, the quasi-kinematic coupling (QKC[1]) shown in Fig. 1-A.

---

*Phone: 617 452 2395; Fax: 509 693 0833; E-mail: culpepper@mit.edu

[1] US Patent No. 6, 193, 430

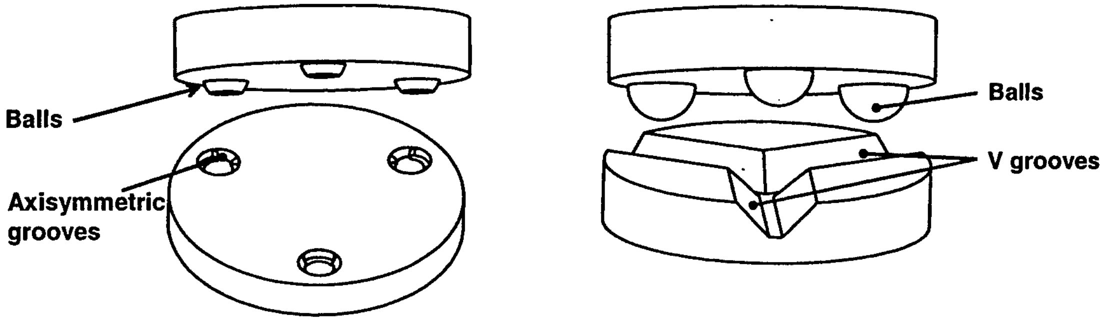

A: Quasi-kinematic coupling (QKC) B: Kinematic coupling (KC)

Fig. 1: Kinematic and quasi-kinematic couplings.

1.2. The need for a new precision coupling

To understand the need for a new class of precision coupling it is necessary to understand why the cost and performance characteristics of current technologies are incompatible with the dual requirements of low-cost and sub-micron precision. We will first examine the inadequacies of coupling types often used in manufacturing. The most common type, the pinned joint, is formed by mating pins from a first component into corresponding holes or slots in a second component. Obtaining micron level precision with these couplings is impractical due to the micron level tolerances that would be required on pins, holes and pin-hole patterns. Other well-known couplings such as tapers, dove-tails and rail-slots would also require micron level tolerances and need expensive finishing operations to reduce the effect of surface finish on alignment.

Let us now consider exact constraint couplings that are well known in precision engineering, but not frequently used in manufacturing. A common type of exact constraint coupling, a kinematic coupling (see Fig. 1-B), can provide better than one micron precision **Error! Reference source not found.** alignment. Unfortunately, they fail to satisfy three low-cost coupling requirements that are common in many manufacturing processes:

1. **Low-cost generation of fine surface finish** : Micron level kinematic couplings must use balls and grooves with ground or polished surfaces [2]. These secondary manufacturing operations make kinematic couplings cost prohibitive.

2. **Low-cost generation of alignment feature shape**: Making v-grooves for kinematic couplings requires more time and more complicated manufacturing processes than required by present low-cost technologies, i.e. pinned joints.

3. **Low-cost means to form sealed interfaces**: Kinematic couplings are not generally meant to form sealed interfaces unless they are equipped with flexures [3] [4] that add cost and complexity.

Having covered common manufacturing couplings and kinematic couplings, we now compare their cost and performance. Figure 2 was generated using the author's and other's[2] experience. The figure shows a clear performance gap between low-performance/low-cost couplings and high-performance/moderate-cost couplings. Clearly, the gap must be addressed if alignment is to be removed as the main obstacle to enabling low-cost, high-precision assemblies. The quasi-kinematic coupling was designed to address this gap.

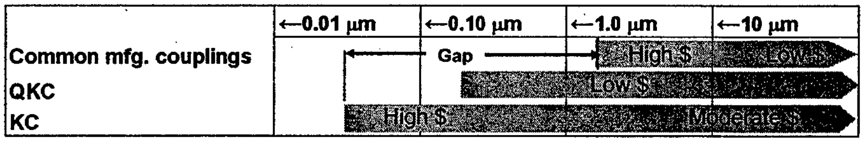

Fig. 2: Cost and precision of common couplings

1.3. Contents

Section 2 discusses the concept of the quasi-kinematic coupling and shows how it satisfies the low-cost coupling requirements in section 1.2. Section 3 provides the theory used to predict coupling stiffness and determine the degree of over constraint in quasi-kinematic coupling joints. Section 4 discusses the theory as implemented in a MathCAD program and section 5 provides experimental results that show quasi-kinematic couplings can provide performance comparable to exact constraint couplings. The implications of coupling cost are covered in section 6.

2. Quasi-Kinematic Coupling Concept

2.1. Similarities and differences between kinematic and quasi-kinematic couplings

From Fig. 1, we see that kinematic and quasi-kinematic couplings share similar geometric characteristics. A kinematic coupling consists of balls attached to a first component that mate with v-grooves in a second component. Quasi-kinematic couplings consist of axisymmetric balls attached to a first component that mate with axisymmetric grooves in a second component. Examples of axisymmetric geometries that form arc contacts are shown in Fig. 3. The orientation of joints in both couplings is also similar. To achieve good stability and balanced stiffness, joints are oriented with ball-groove contacts symmetric about the bisectors of the coupling triangle [2].

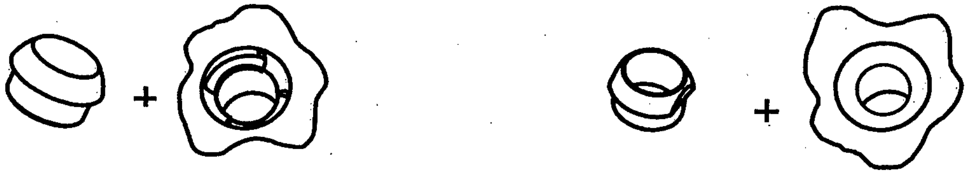

A: QKC joint with relieved groove **B: QKC joint with relieved ball**

Fig. 3: Two methods for forming quasi-kinematic coupling joints

---

[2] Discussions with Prof. A. H. Slocum, MIT Precision Engineering Group

The fundamental difference between kinematic couplings and quasi-kinematic couplings lies in the nature of the ball-groove contacts. Kinematic couplings establish six points of contact that provide deterministic constraint of six degrees of freedom. Quasi-kinematic couplings form six arcs of contact that introduce over constraint into the coupling. Although quasi-kinematic couplings are technically over constrained, clever design can produce a weakly over constrained mate that emulates a kinematic coupling.

Making this happen requires an understanding of how arc contacts over constrain the coupling. We will develop this understanding via Fig. 4. In the figure, we see the projections of ball-groove contact forces on the plane of coupling. The length of an arrow signifies the magnitude of a given constraint force. The diagram in Fig. 4-A shows that ideal kinematic couplings only provide constraint in directions normal to the bisectors of the coupling triangle. This is sufficient to achieve exact constraint. The arc contacts of the quasi-kinematic coupling in Fig. 4.-B offer constraint perpendicular to and along the bisectors of the coupling triangle. This is more than is required to achieve exact constraint, thus we have over constraint.

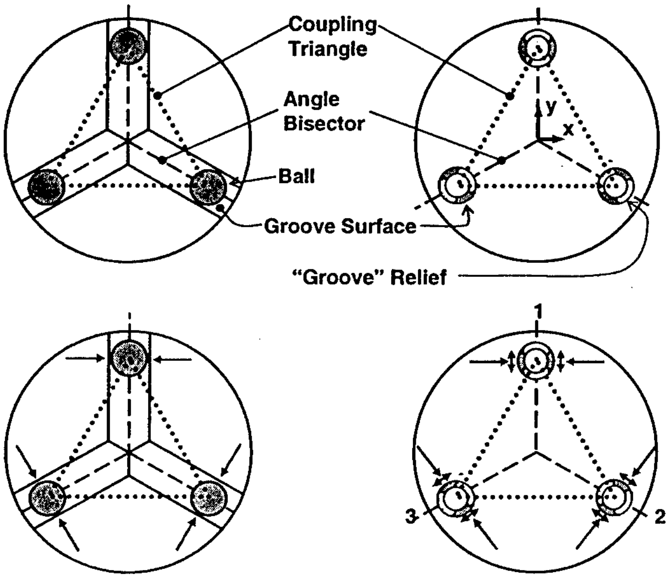

A: Ideal kinematic coupling **B: QKC: Groove relieved**

Fig. 4: Planar constraints in kinematic and quasi-kinematic couplings

The key to designing quasi-kinematic couplings is to minimize over constraint by minimizing the contact angle. The contact angle is defined by illustration in Fig. 5. The joint in Fig. 5 represents joint 1 in Fig. 4-B. Arrows representing the constraint per unit length of contact arc are shown on the left sides of Figs. 5-A and 5-B. By inspection, we can see that constraint contributions that are parallel to the angle bisectors (in the y direction) can be reduced by making the contact angle smaller. This in turn reduces the degree of over constraint in the joint. We will improve this qualitative example with a quantitative metric in section 3.7. For now we continue with a qualitative assessment of quasi-kinematic coupling attributes.

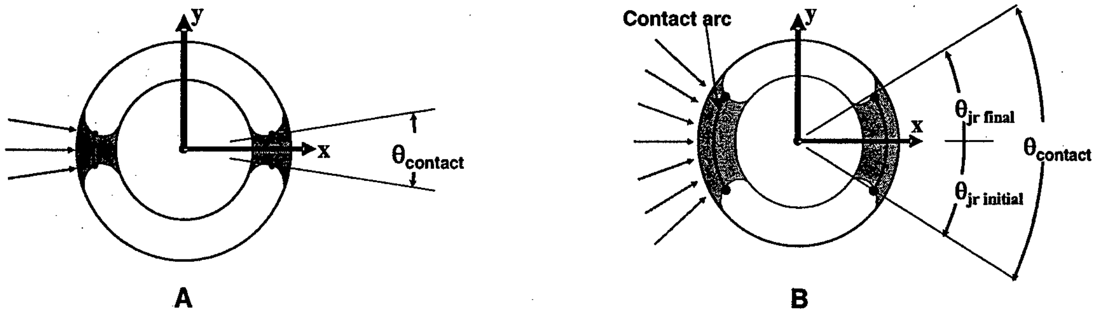

Fig. 5: Link between $\theta_{contact}$ and over constraint in quasi-kinematic couplings

2.2. QKCs that satisfy low-cost coupling requirements

We now assess the performance of quasi-kinematic couplings with respect to the low-cost coupling requirements from section 1.2.

1. **Low-cost generation of fine surface finish**: Quasi-kinematic coupling balls can be made from low-cost, polished spheres (i.e. bearings). By applying sufficient mating force, one can burnish the surface of the groove with the harder, finer surface of the ball. The result of this burnishing process is shown in Fig.6. A successful burnishing operation has two important requirements:
   - A ball with polished (or ground if sufficient) surface finish and Young's modulus more than ~ three to four times that of the groove [5].
   - Tangential sliding between the ball and groove surfaces [6] during mating. Contact without sliding does not remove asperities [7].

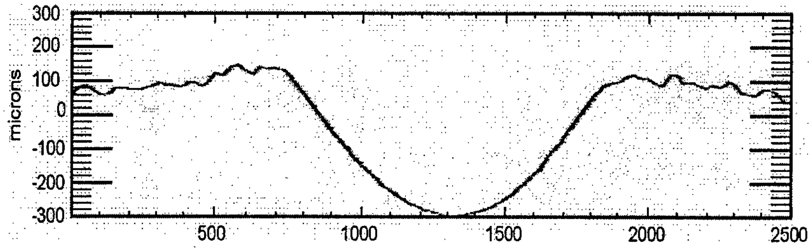

Fig. 6: Surface trace of burnished quasi-kinematic coupling groove

2. **Low-cost generation of alignment feature shape**: Quasi-kinematic coupling grooves are axisymmetric, thus they can be made in a "plunge/drill" operation using a counter sink or form tool. Groove reliefs can be cast, formed, milled, or drilled in place. The tools and processes required to form the groove seats are comparable to those required to make pinned joints.

Low-cost means to form sealed interfaces: It is possible to enable sealing contact by integrating compliance into a quasi-kinematic coupling joint. Using the ball design in Fig. 7-A, we add z compliance via the hollow core and side undercut. As shown in Fig. 7-B, a nesting force mates the balls and grooves. By increasing the nesting force, we can deform the ball-groove joints until the gap separating the coupled components closes. Gaps of several hundred microns can be closed if the ball-groove materials plastically deform during the first mate. When the coupling is unloaded, elastic recovery of the ball and groove materials restores a portion of the gap between the mated components. An initial gap between components is necessary to maintain the kinematic nature of the coupling in subsequent mates.

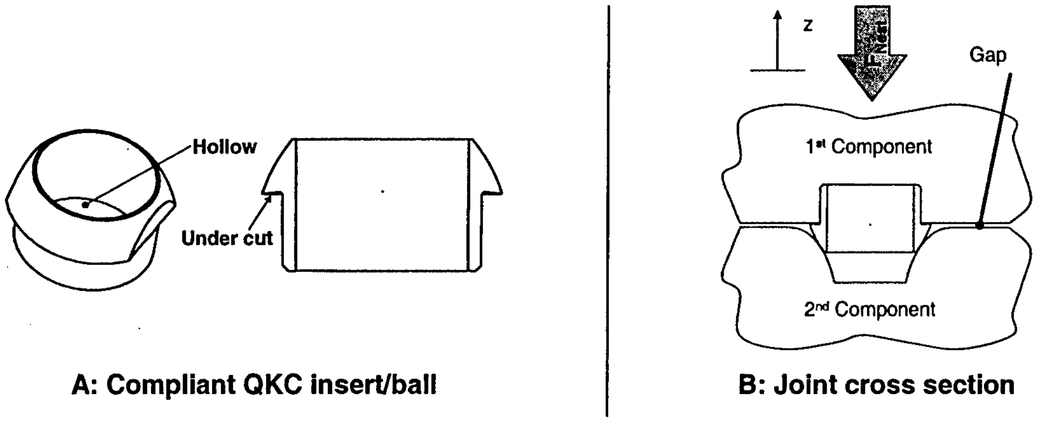
Hollow
Under cut
z
FNet
Gap
1st Component
2nd Component

A: Compliant QKC insert/ball **B: Joint cross section**

Fig. 7: Geometry of elements in a compliant quasi-kinematic coupling joint

3. Modeling QKC Stiffness

3.1. Analysis method

When analyzing kinematic couplings, contact forces and displacements may be assumed normal to the ball-groove contact, and modeled with "spring like" Hertzian point contacts [2] [8] [9] **Error! Reference source not found.**. When analyzing arc contacts, the direction of contact forces may generally not be assumed and the contacts can not be modeled as point contacts. An appropriate analysis method is outlined in 8-A. We preload a coupling with a desired displacement, impose an error displacement on this "perfectly" mated state, calculate ball-groove contact forces and then use these forces and the error displacements to calculate stiffness. This is a significant departure from the method (Fig. 8-B) used to evaluate kinematic couplings. The goal of sections 3.2 – 3.6 is to develop the theory required for stiffness modeling of quasi-kinematic couplings.

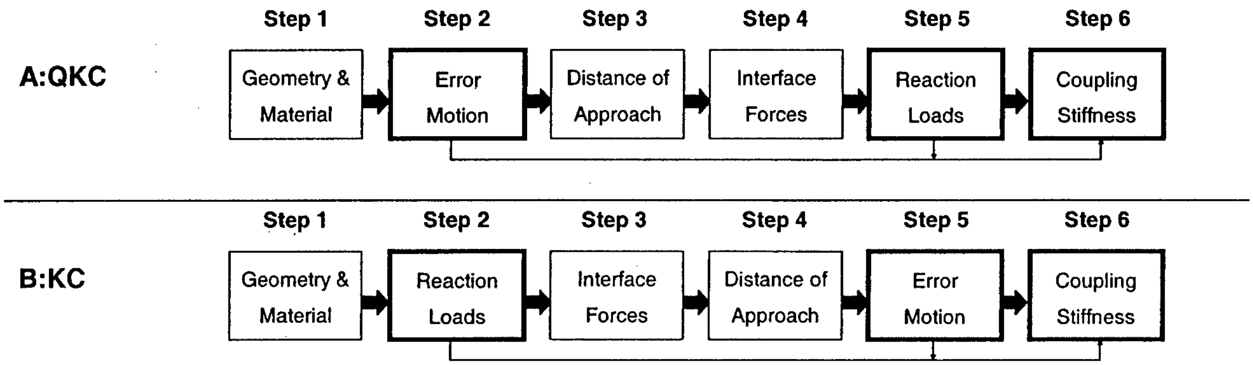
Step 1
Step 2
Step 3
Step 4
Step 5
Step 6
A:QKC
Geometry & Material
Error Motion
Distance of Approach
Interface Forces
Reaction Loads
Coupling Stiffness
Step 1
Step 2
Step 3
Step 4
Step 5
Step 6
B:KC
Geometry & Material
Reaction Loads
Interface Forces
Distance of Approach
Error Motion
Coupling Stiffness

Fig. 8: Stiffness modeling strategies for kinematic and quasi-kinematic couplings

3.2. Step 1: Material and geometry characteristics

The first step is to identify what the coupling components are made of and how they will be shaped and arranged. We will assume common material, shape and size within the set of balls and within groove sets.

Material characteristics

The Young's modulus and Poison's ratio of the ball and groove materials are needed to model elastic contact [11]. Modeling plastic deformation requires a tangent modulus and stress value at which the Young's and tangent modulus intersect. Figure 9 shows the values fitted to data from tests on a leaded steel.

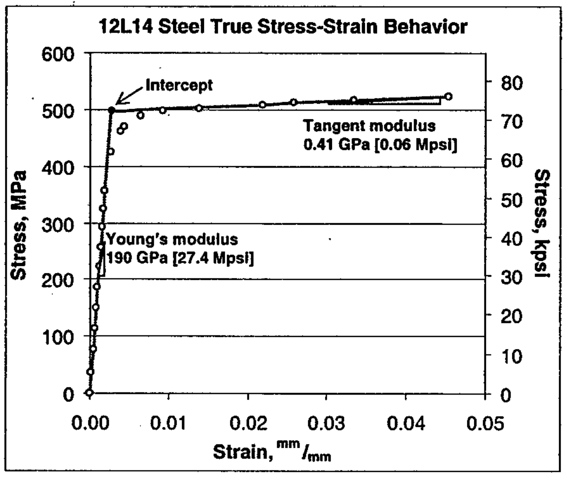

Fig. 9: Elastic-plastic behavior of 12L14 steel

Geometric characteristics

With the help of Figs. 10 and 11, we define important geometry characteristics. The first is the coupling coordinate system, *CCS*, that is attached to the coupling centroid of the grounded component (contains grooves). A displaced coordinate system, *DCS*, is attached to the centroid of the component that is displaced (contains balls) when coupling errors are present. When the coupling is mated with a pre-load displacement, but no error, the *CCS* and *DCS* are coincident.

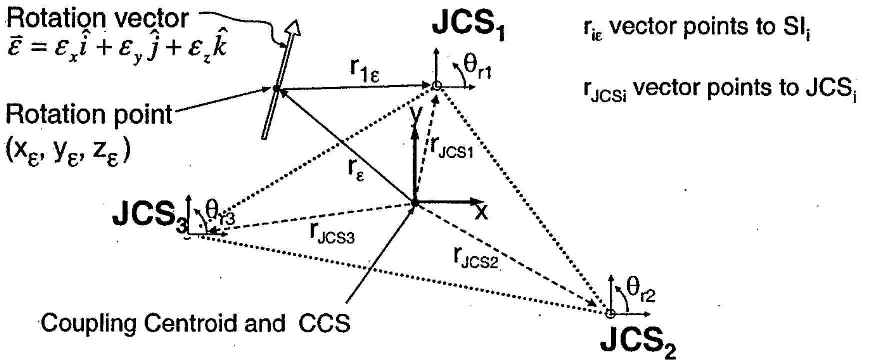
Rotation vector
$\bar{\varepsilon} = \varepsilon_x \hat{i} + \varepsilon_y \hat{j} + \varepsilon_z \hat{k}$
Rotation point
$(x_\varepsilon, y_\varepsilon, z_\varepsilon)$
JCS_1
$r_{1\varepsilon}$
θ_{r1}
$r_{i\varepsilon}$ vector points to SI_i
r_{JCSi} vector points to JCS_i
y
r_{JCS1}
r_ε
x
JCS_3
θ_{r3}
r_{JCS3}
r_{JCS2}
θ_{r2}
Coupling Centroid and CCS
JCS_2

Fig. 10: Geometry characteristics of quasi-kinematic couplings

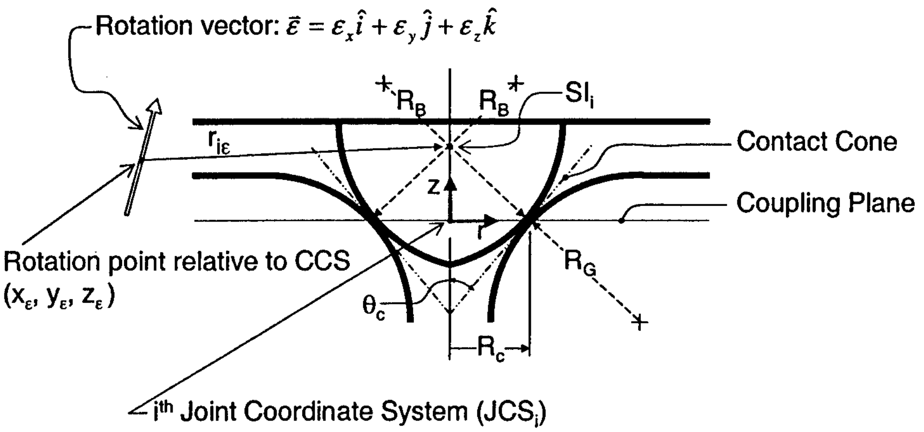
Rotation vector: $\vec{\varepsilon} = \varepsilon_x\hat{i} + \varepsilon_y\hat{j} + \varepsilon_z\hat{k}$
R_B
R_B
SI_i
$r_{i\varepsilon}$
Contact Cone
Coupling Plane
z
r
Rotation point relative to CCS
$(x_\varepsilon, y_\varepsilon, z_\varepsilon)$
θ_c
R_G
R_c
ith Joint Coordinate System (JCS_i)

R_G:	Groove radius	R_B:	Ball radius
R_c:	Contact radius	θ_c:	Half cone angle
$r_{i\varepsilon}$:	Ball's rotation moment arm	SI_i:	Symmetry intersect

Fig. 11: Geometry characteristics of quasi-kinematic coupling joints

Our analysis will now utilize subscripts *i* and *j* to refer to specific joints ($i = 1$ to 3) and contact arcs ($j = 1$ to 6) respectively. We define a joint coordinate system, JCS_i , for each joint. Each JCS_i measures position in r_i, θ_{ri}, and z_i as collectively shown by Figs. 10 and 11. The z axis of each JCS_i is perpendicular to the coupling plane and coincident with the respective groove's axis of symmetry. For each JCS_i, $\theta_{ri} = 0$ when the projection of the joint's r vector on the x-y plane of the CCS is parallel to the x axis of the CCS. We define a contact cone as the surface which contains all lines that run through the joint's axis of symmetry and are tangent to the ball and groove surfaces at contact. The cone is characterized by the half-cone angle, θ_c. Other variables that describe the size and location of coupling components are defined by illustration in Figs. 10 and 11.

3.3. Step 2: Imposed error motions

Ball-groove reaction force (therefore coupling stiffness) is a function of the compression of ball and groove material. This in turn depends on the error displacement of a ball's far field point, SI_i in Figs.11 and 12, from its pre-loaded position in the groove.

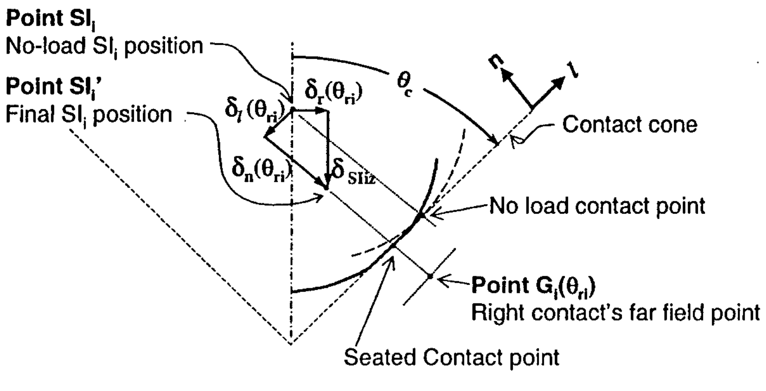
Point SI_i
No-load SI_i position
Point SI_i'
Final SI_i position
$\delta_r(\theta_{ri})$
$\delta_t(\theta_{ri})$
$\delta_n(\theta_{ri})$
δ_{SIiz}
θ_c
$\hat{n}$
$\hat{t}$
Contact cone
No load contact point
Point $G_i(\theta_{ri})$
Right contact's far field point
Seated Contact point

Fig. 12: Positions and motions of ball and groove far field points

The displacement of a ball's *SI* can be expressed as a combination of the translation ($\vec{\delta}_c$) of the *DCS* relative to the *CCS* and rotation ($\vec{\varepsilon}$) of the displaced component about a specified point (x_ε, y_ε, z_ε). This displacement can also be given as a combination of preload displacement and error displacement of a ball's SI_i relative to the *CCS*. Equation (1) expresses both possibilities:

$$\vec{\delta}_{SIi} = \vec{\delta}\Big|_{preload_{SIi}} + \vec{\delta}\Big|_{error_{SIi}} = \vec{\delta}_c + \vec{\varepsilon} \times \vec{r}_{i\varepsilon} = \begin{bmatrix} \delta_{SIix}\ \hat{i} \\ \delta_{SIiy}\ \hat{j} \\ \delta_{SIiz}\ \hat{k} \end{bmatrix} \tag{1}$$

In developing Eq. (1), we assume the coupling is built to limit rotation errors on the order of several μradians, thus small-angle approximations are valid. We also assume that good coupling design practices have been followed so that the coupled components can be considered as rigid bodies. The rigid body assumption requires that the mated components and their interfaces with the balls and grooves are more than ten times as stiff as the ball-groove contacts.

3.4. Step 3: Distance of approach between far field points in ball-groove joints

The compression of ball and groove material may vary about the arc contact. For example, consider a sphere mated in a cone. If we displace the sphere into and along the cone's axis of symmetry the compression about the resulting circular contact will be uniform. Subsequent displacement perpendicular to the axis of symmetry will lead to variations in compression about the contact. As reaction force depends upon the compression of material, we expect the force per unit length of contact arc will vary about the ball-groove contact.

A common metric used to describe material compression between contacting elements is the distance of approach, δ_n, between two far field points [11]. Figure 12 shows the distance of approach (as $\delta_n(\theta_{ri})$) between far field points, SI_i and $G_i(\theta_{ri})$, in a cross section through a joint cut at θ_{ri}. The distance of approach in a cross section is a function of the axial ($\vec{\delta}_{SIiz}$) and radial ($\vec{\delta}_r(\theta_{ri})$) displacement of the SI_i relative to the JCS_i. Equation (2) provides the axial and radial displacements as a function of ball displacement.

$$\begin{bmatrix} \delta_r(\theta_{ri})\ \ \hat{r} \\ \delta_{SIiz}\ \ \ \hat{k} \end{bmatrix} = \begin{bmatrix} \left(\delta_{SIix}^2 + \delta_{SIiy}^2\right)^{0.5} \cdot \cos\left[\theta_{ri} - \operatorname{atan}\left(\delta_{SIiy} / \delta_{SIix}\right)\right]\ \ \hat{r} \\ \delta_{SIiz}\ \ \hat{k} \end{bmatrix} \tag{2}$$

Using Fig. 12 and Eq. (2) we can produce the relationship for $\delta_n(\theta_{ri})$ given in Eq. (3).

$$\vec{\delta}_n(\theta_{ri}) = \left\{ -\left(\delta_{SIix}^2 + \delta_{SIiy}^2\right)^{0.5} \cos\left[\theta_{ri} - \operatorname{atan}\left(\delta_{SIiy} / \delta_{SIix}\right)\right] \cdot \cos(\theta_c) + \delta_{SIiz} \cdot \sin(\theta_c) \right\} \hat{n} \tag{3}$$

3.5. *Step 4: Modeling interface forces as a function of δ_n*

For solid ball-groove joints that experience elastic contact deformation, one may use classic line contact solutions to relate the distance of approach to the force per unit length of contact, $\vec{f}_n(\theta_{ri})$ **Error! Reference source not found. Error! Reference source not found.**. A more general, flexible approach is needed to model a wide range of contact situations. For instance consider pure elastic contact deformation, contact deformation in combination with integral compliance, or plastic contact deformation. Practical applications that use one or more of these contact situations were discussed in section 2.2. Given the material properties and geometry characteristics from section 3.2, we can obtain the relationship between $\vec{f}_n(\theta_{ri})$ and $\vec{\delta}_n(\theta_{ri})$. This can be accomplished using classical line contact solutions, FEA, or other suitable analyses from which results can be fit to the form of Eq. (4).

$$\vec{f}_n(\theta_{ri}) = K[\delta_n(\theta_{ri})]^b\ \hat{n} \tag{4}$$

In Eq. (4), *K* is a stiffness constant and the exponent b is used to reflect the rate of change in contact stiffness with changing $\vec{\delta}_n(\theta_{ri})$. Both *K* and *b* are functions of ball-groove material and geometry. Let us consider an example which illustrates what Eq. (4) can tell us about a coupling's performance. In Fig. 13, we see the contact behavior of a joint that has experienced plastic deformation during the first mate, i.e. as needed to close a gap. In subsequent couple-uncouple cycles, the load-unload behavior of the contact follows the right most curve as indicated. The slope of this particular curve is greater than unity thus the joint's stiffness increases with increasing preload or increasing error load. The geometry of the ball can be "tuned" to achieve different values of *b*, thus controlling how a coupling's stiffness increases with load.

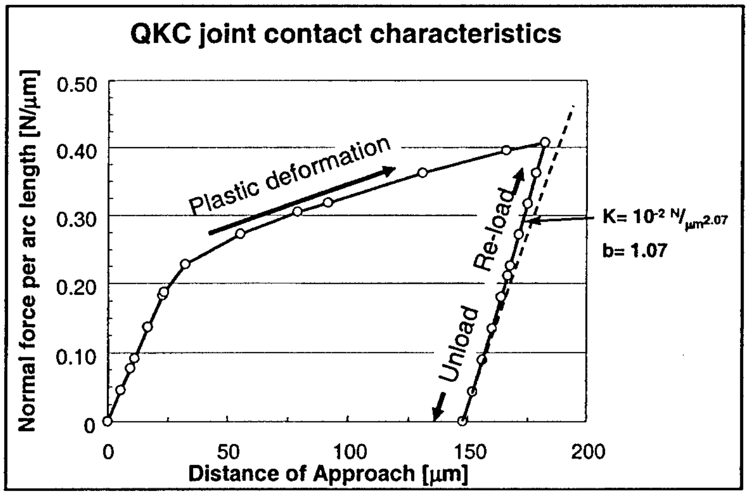

Fig. 13: Contact load-displacement (f_n vs. δ_n) behavior of a QKC joint
[$\theta_c = 32°$; $K = 1\times10^{-2}\dfrac{N}{\mu m^{2.07}}$; $b = 1.07$; $R_c = 0.66$ cm]

To ensure that contact is not lost between the ball and groove, we monitor a "constant contact" constraint, $\bar{\delta}_n(\theta_{ri})$ ≤ 0, along the arc of contact. If this is violated, the ball and groove have separated over some portion of the contact and our analysis may predict tensile contact forces. Clearly this invalidates the model.

3.6. Step 5: Reaction force on an arc contact

We define a unit vector, $\hat{s}(\theta_{ri}) = \hat{n}(\theta_{ri}) \times \hat{l}(\theta_{ri})$, that is tangent to the contact arc and changes orientation with θ_{ri}. This unit vector points into the page on the right side of Fig. 14-B and out of the page on the left side of Fig. 14-B.

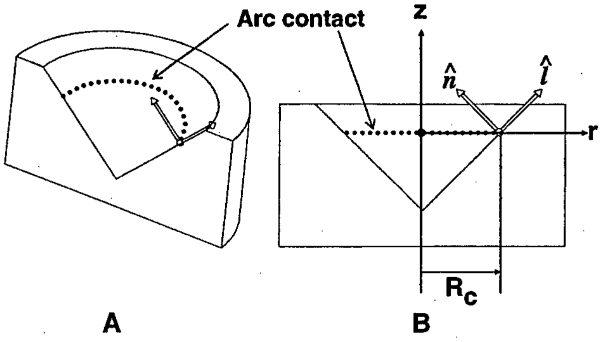

Fig. 14: Contact arc and $\hat{n}(\theta_{ri}), \hat{l}(\theta_{ri})$ coordinates for a cross section at $\theta = \theta_{ri}$

In Eq. (5) we calculate the resultant force on the arc contact via a line integral along the arc of contact.

$$\bar{F}_j = \int_{s_{initial}}^{s_{final}} \left[f_n(\theta_{ri})\hat{n}(\theta_{ri}) + f_l(\theta_{ri})\hat{l}(\theta_{ri}) + f_s(\theta_{ri})\hat{s}(\theta_{ri}) \right] ds \approx \int_{\theta_{jr\ initial}}^{\theta_{jr\ final}} \left[f_n(\theta_r)\hat{n}(\theta_{ri}) \right] R_c \, d\theta_{ri} \tag{5}$$

The limits of the integral are defined by the ends of the arc contact as illustrated in Fig. 5-B. The subscripts *n, l,* and *s* differentiate between unit contact forces in the subscripted directions. It is good design practice to minimize friction ($\mu_{static} < 0.10$) at a coupling's contacts to prevent tangential stress build up. In Eq. (5) we've assumed this practice in quasi-kinematic coupling design and take the contribution of the tangential contact forces as negligible compared to the contribution of the normal forces. If a rare application requires the tangential components, they can be added to the analysis. Using Eq. (4), Eq. (5) simplifies to Eq. (6).

$$\bar{F}_j = \int_{\theta_{jr\ initial}}^{\theta_{jr\ final}} \left\{ K[\delta_n(\theta_{ri})]^b \, \hat{n}(\theta_{ri}) \right\} R_c \, d\theta_{ri} \tag{6}$$

We now use the matrix in Eq. (7) to transform the unit contact force into the frame of the *CCS*.

$$\begin{bmatrix} \hat{n}(\theta_{ri}) \\ \hat{s}(\theta_{ri}) \\ \hat{l}(\theta_{ri}) \end{bmatrix} = \begin{bmatrix} -\cos(\theta_{ri})\cdot\cos(\theta_c) & -\sin(\theta_{ri})\cdot\cos(\theta_c) & \sin(\theta_c) \\ -\sin(\theta_{ri}) & \cos(\theta_{ri}) & 0 \\ \cos(\theta_{ri})\cdot\sin(\theta_c) & \sin(\theta_{ri})\cdot\sin(\theta_c) & \cos(\theta_c) \end{bmatrix} \cdot \begin{bmatrix} \hat{i} \\ \hat{j} \\ \hat{k} \end{bmatrix} \tag{7}$$

In combining Eqs. (6) and (7) we obtain Eq. (8) which provides the total reaction force for contact arc *j*:

$$\vec{F}_j = \begin{bmatrix} \int_{\theta_{jr\,initial}}^{\theta_{jr\,final}} \left\{ R_c\, K\left(\delta_n(\theta_{ri})\right)^b \left[-\cos(\theta_{ri}) \cdot \cos(\theta_c)\right] d\theta_{ri} \right\} \hat{i} \\ \int_{\theta_{jr\,initial}}^{\theta_{jr\,final}} \left\{ R_c\, K\left(\delta_n(\theta_{ri})\right)^b \left[-\sin(\theta_{ri}) \cdot \cos(\theta_c)\right] d\theta_{ri} \right\} \hat{j} \\ \int_{\theta_{jr\,initial}}^{\theta_{jr\,final}} \left\{ R_c\, K\left(\delta_n(\theta_{ri})\right)^b \left[\sin(\theta_c)\right] d\theta_{ri} \right\} \qquad \hat{k} \end{bmatrix} \tag{8}$$

When the contact forces are summed over six contact arcs as in Eq. (9), we obtain the reaction force between the mated components.

$$\vec{F}_{\text{Reaction}} = \sum_{j=1}^{6} \vec{F}_j \tag{9}$$

The reaction torque in Eq. (10) is the sum of torques about the coupling centroid due to each ball-groove reaction force ($\vec{F}_i$) and moment arm ($\vec{r}_{SIi}$) between the *CCS* and the respective ball's SI_i.

$$\vec{T}_{\text{Re}\,action} = \sum_{i=1}^{3} \vec{r}_{SIi} \times \vec{F}_i \tag{10}$$

Step 6: Stiffness calculation

Coupling stiffness in the direction of the error displacement is calculated as:

$$k_{\text{imposed}} = \frac{d(\text{Reaction})}{d(\text{Imposed Error Displacement})} \tag{11}$$

When we apply linear displacements, the reaction is the force given by Eq. (9). When we apply rotation displacements, the reaction is the torque given by Eq. (10).

3.7. Constraint metric

In section 2.1 we learned that some degree of over constraint is inherent in quasi-kinematic couplings. When designing them it is useful to have a metric that compares desired/undesired constraints in and between different joint designs. We will use the constraint metric as defined in Eq. (12).

$$CM_i = \frac{\text{Stiffness parallel to bisector}}{\text{Stiffness perpendicular to bisector}} = \frac{k_{i\ \|\text{Bisector}}}{k_{i\ \perp\text{Bisector}}} \tag{12}$$

Let us consider the joint design described by Fig. 15–A and Table 1.

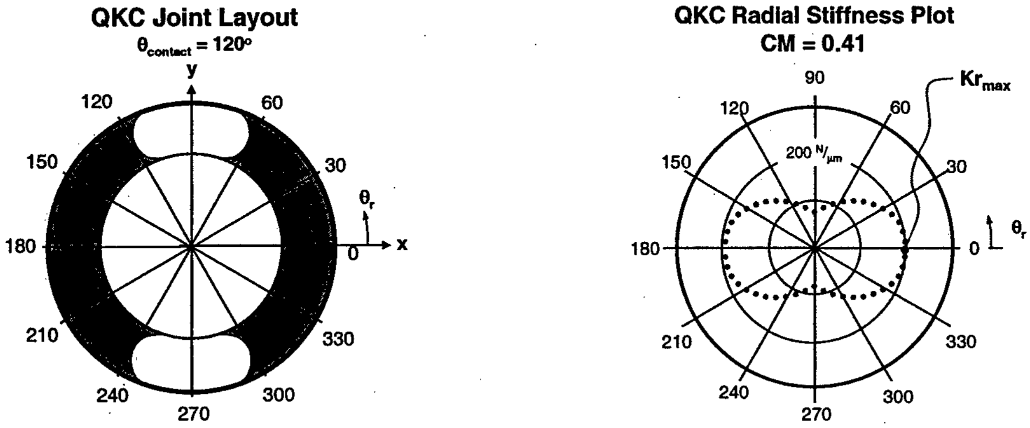
QKC Joint Layout

QKC Radial Stiffness Plot

CM = 0.41

A: Top view of QKC groove

B: Stiffness plot of QKC joint

Fig. 15: QKC joint orientation and stiffness

[θ_c= 45°; $\theta_{contact}$= 120°; $K = 1\times10^{-2}\dfrac{N}{\mu m^{2.07}}$; b =1.07; R_c= 0.66 cm; $\delta_{z\text{-}preload}$ = -60 μm]

Table 1: Example QKC joint design characteristics

Design variable	Value	
R_c:	0.66 cm	[0.204 in]
$\delta_{z\text{-}preload}$:	-60 μm	[-0.0024 in]
K:	$1\times10^{-2}\dfrac{N}{\mu m^{2.07}}$	[$2948850\dfrac{lbf}{in^{2.07}}$]
b:	1.07	
$\theta_{contact}$:	120°	
θ_c:	45°	

The joint's radial stiffness plot, shown in Fig. 15-B, was generated using the theory in sub-sections 3.2 – 3.6. We can use results from the theory (or estimate values from Fig. 15-B) to determine the constraint metric for this joint.

$$CM = \left.\frac{\mathrm{k}(90^\circ)}{\mathrm{k}(0^\circ)}\right|_{Fig.15} = \frac{80\dfrac{N}{\mu m}}{195\dfrac{N}{\mu m}} = 0.41 \tag{13}$$

3.8. Making use of the constraint metric

In quasi-kinematic couplings, the *CM* is unity for $\theta_{contact}$ = 180° (gross over constraint) and approaches 0 as $\theta_{contact} \rightarrow$ 0°. The desire to emulate exact constraint couplings compels us to specify the lowest possible contact angle. It is clear however, that one can not specify $\theta_{contact}$ ~ 0° and obtain a coupling with reasonable stiffness. The key is simultaneous consideration of the constraint metric and the coupling's stiffness in directions of interest. We will demonstrate this approach via a hypothetical application.

Consider a 120° coupling (grooves spaced at 120°) that must resist z moments about its' centroid. The design calls for 125 $^{N}/_{\mu m}$ as the lowest value for the maximum radial stiffness of a joint (Kr_{max} would be 195 $^{N}/_{\mu m}$ in Fig. 15-B). The plot in Fig. 16 shows the effect of $\theta_{contact}$ on our constraint and stiffness metrics. Given this plot, we could justify choosing a contact angle as low as 60° with a $CM = 0.10$. It is interesting to note that the trade-off between stiffness and constraint is a favorable transaction for large contact angles.

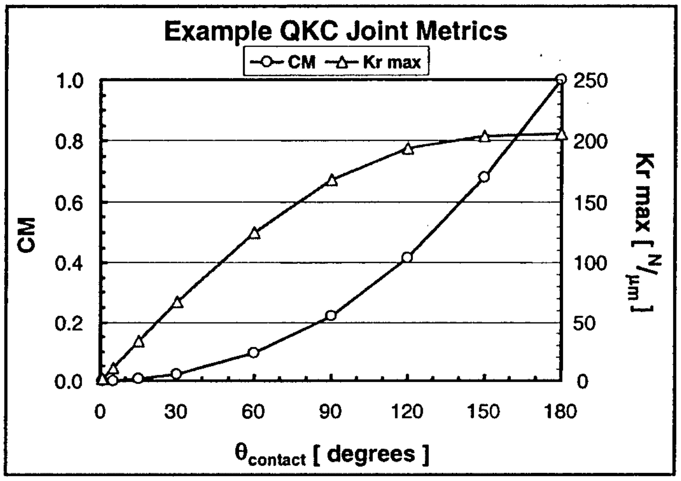

Fig. 16: Comparing performance metrics of quasi-kinematic couplings

4. Testing the MathCAD Model[3]

The theory developed in section 3 was implemented in a MathCAD program and checked by running the following tests:

- Imposed translation errors in the z direction produced only net z forces.
- Imposed rotation errors about the z axis of the *CCS* produced only net z moments.
- Imposed displacements along one bisector of a 120° coupling (i.e. in the y direction for the coupling in Fig. 4-B) did not produce net y or z moments.
- The x and y reaction forces are 0 when θ_c is 90° (groove becomes a flat).
- When θ_c is set to 0° the ball will loose contact with the groove (now a cylinder) for any radial displacement. The model detects this as a violation of the "constant contact" constraint.

---

[3] The MathCAD document can be found in the appendix.

5. Experimental Results

A form of quasi-kinematic coupling has been used in precision automotive assemblies[4] to provide $^2/_3$ micron repeatability in journal bearing assemblies [14] [15]. To meet unusual stiffness requirements, the joints were not placed in the orientations that best emulate exact constraint couplings. These joints were also designed with large contact angles ($\theta_{contact} = 120°$, $CM = 0.41$) to increase coupling stiffness. Though this design serves as proof of sub-micron performance, it is not a good means to demonstrate the best performance of quasi-kinematic couplings.

An experiment was run to determine how repeatability would compare to that of a common kinematic coupling when the contact angle ($\theta_{contact} = 60°$, $CM = 0.10$) and joint orientations were set to better emulate a kinematic coupling. The test coupling in Fig. 17-A was manufactured with less than 25 micron mismatch between the axis of symmetry of any ball and mated groove. The results of repeatability tests with lubricated joints are provided in Fig. 17-B. The results show the coupling repeats in-plane to ¼ micron after an initial wear-in period. These results compare more favorably with the sub-micron performance ($^1/_{10}$ micron) of well designed and lubricated kinematic couplings [16].

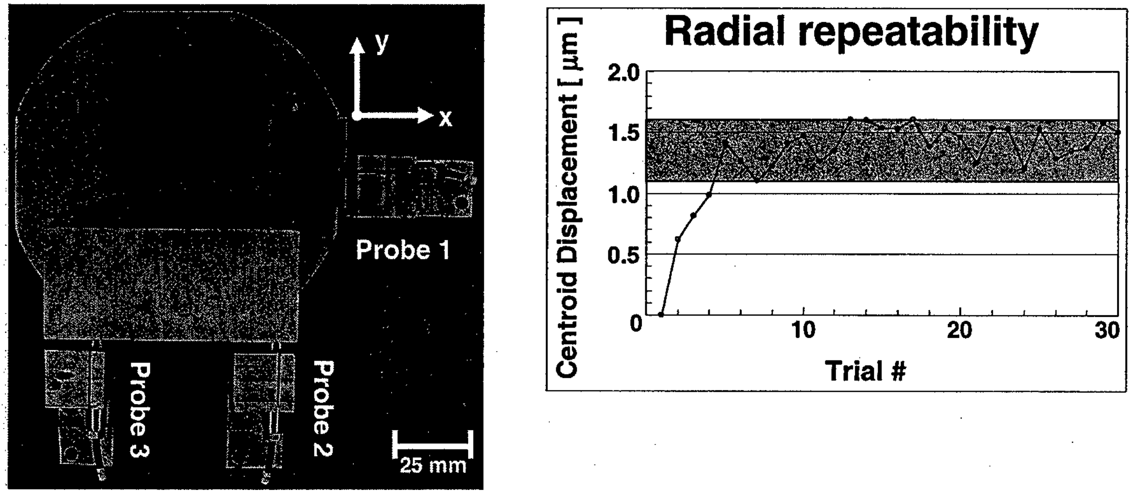

A: QKC test setup

B: QKC centroid coupling error (x-y plane)

Fig. 17: QKC test setup and repeatability results
[$\theta_c = 32°$; $\theta_{contact} = 60°$; $K = 1\times10^{-2}\dfrac{N}{\mu m^{2.07}}$; $b = 1.07$; $R_c = 0.66$ cm; 25 N preload]

6. Coupling Cost

The quasi-kinematic coupling elements used in the automotive assemblies and test coupling resemble the elements shown in Fig. 3-A. These ball-groove sets cost approximately one dollar when manufactured in volumes greater than 100,000 couplings per year. When manufactured in volumes of less than several hundred per year, a ball-groove set may cost $60. This is in contrast to several hundred dollars one could pay for high-performance kinematic couplings.

---

[4] US Patent pending

7. Conclusions and Issues for Further Research

This paper has provided the means to calculate coupling stiffness and determine the degree of over constraint in quasi-kinematic coupling joints. The theory used to model coupling stiffness has been implemented in MathCAD and tested. Experimental results show that properly designed quasi-kinematic couplings can provide precision alignment that is comparable to kinematic couplings. Characteristics such as low-cost, ease of manufacture, ability to form sealed joints and sub-micron performance will make the coupling an enabling technology. This will be particularly important for high-precision, high-volume assemblies in automotive, photonics, optical and other general product assemblies. Subsequent research activities will include developing the means to address the effects of mismatch between ball and groove patterns in quasi-kinematic couplings.

8. Acknowledgments

This work was sponsored by the Ford Motor Company and a grant from the Defense Logistics Agency AQP. The author wishes to thank them for their financial and technical assistance.

9. Appendix

The MathCAD program discussed in section 4 is appended for inspection.

QUASI KINEMATIC COUPLING STIFFNESS MODELING TOOL

CHANE ONLY VARIABLES IN SHADED BOXES, ALL OTHERS ARE CALCULATED VALUES:

LOCATION OF JOINTS IN X, Y. LOCATION OF COUPLING PLANE IN Z

Location of joint coordinate systems (JCSi) relative to an arbitrary coordinate system:
Worksheet will calculate the position of the coupling centroid based on this input.

JCS3 must be left most joint, JCS2 is right most joint, JCS1 has greater y value than JCS2 and JCS3

$$JCS_i := \begin{pmatrix} x \cdot in \\ y \cdot in \\ z \cdot in \end{pmatrix}$$

$$JCS_1 := \begin{pmatrix} 0.0000 \cdot in \\ 3.0000 \cdot in \\ 0 \cdot in \end{pmatrix}$$

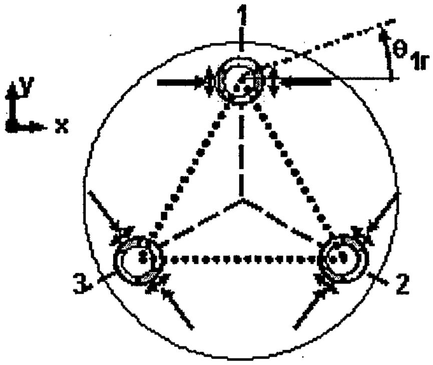

$$JCS_3 := \begin{pmatrix} -2.5981 \cdot in \\ -1.5000 \cdot in \\ {JCS_1}_2 \end{pmatrix}$$

$$JCS_2 := \begin{pmatrix} 2.5981 \cdot in \\ -1.5000 \cdot in \\ {JCS_1}_2 \end{pmatrix}$$

Fig. A-1: Definition of joint positions

Calculate position of coupling centroid (xcc, ycc, zcc) relative to arbitrary coordinate system:

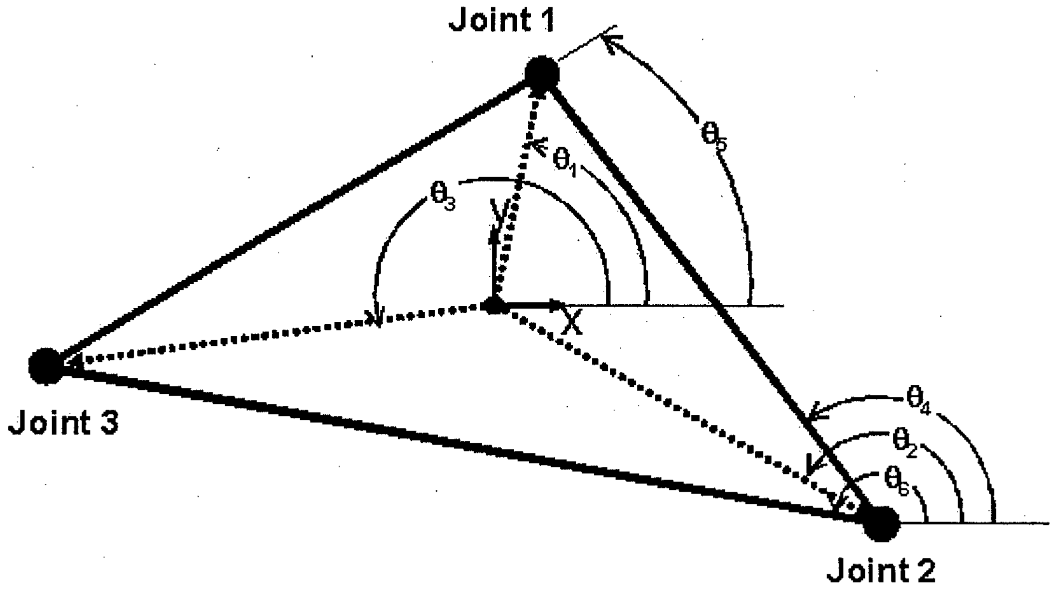

Fig. A-2: Definition of coupling triangle's bisector angles and side angles

$$\theta_4 := \mathrm{atan2}\left(JCS1_0 - JCS2_0, JCS1_1 - JCS2_1\right) \qquad \theta_5 := \mathrm{atan2}\left(JCS1_0 - JCS3_0, JCS1_1 - JCS3_1\right)$$

$$\theta_6 := \mathrm{atan2}\left(JCS3_0 - JCS2_0, JCS3_1 - JCS2_1\right)$$

$$\theta_1 := \frac{1}{2}\cdot\left(\theta_4 + \theta_5\right) \qquad \theta_2 := \frac{1}{2}\cdot\left(\theta_4 + \theta_6\right) \qquad \theta_3 := \frac{1}{2}\cdot\left[\left(\theta_5 + \theta_6\right) + \pi\right]$$

$$CCS_x := \frac{\left(JCS3_1 - JCS2_1 - \tan\left(\theta_3\right)\cdot JCS3_0 + \tan\left(\theta_2\right)\cdot JCS2_0\right)}{\tan\left(\theta_2\right) - \tan\left(\theta_3\right)}$$

$$CCS_y := \tan\left(\theta_2\right)\cdot\left(CCS_x - JCS2_0\right) + JCS2_1 \qquad CCS_z := JCS1_2$$

Coupling Coordinate System Relative To Arbitrary Coordinate System:

$$CCS_{cc} := \begin{pmatrix} CCS_x \\ CCS_y \\ CCS_z \end{pmatrix} \qquad CCS_{cc} = \begin{pmatrix} 0.0000 \\ 0.0000 \\ 0.0000 \end{pmatrix} \mathrm{in}$$

Joint Coordinate System Positions Vectors Relative To Coupling Center:

$$r_{JCS1} := JCS_1 - CCS_{cc} \qquad r_{JCS2} := JCS_2 - CCS_{cc} \qquad r_{JCS3} := JCS_3 - CCS_{cc}$$

$$\left|r_{JCS1}\right| = 3\,\mathrm{in} \qquad \left|r_{JCS2}\right| = 3\,\mathrm{in} \qquad \left|r_{JCS3}\right| = 3\,\mathrm{in}$$

JOINT DIMENSIONS AND CONTACT CHARACTERISTICS

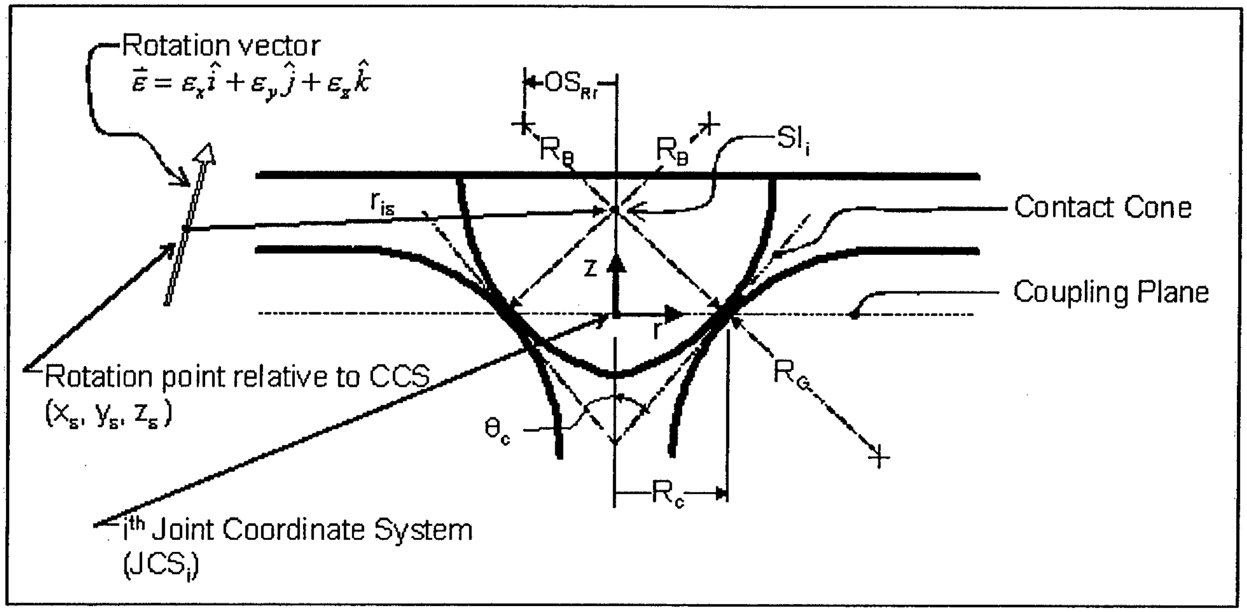
Rotation vector
$\vec{\varepsilon} = \varepsilon_x\hat{i} + \varepsilon_y\hat{j} + \varepsilon_z\hat{k}$
OS_{Rr}
R_B
R_B
SI_i
r_{is}
Contact Cone
Coupling Plane
z
r
Rotation point relative to CCS
(x_s, y_s, z_s)
θ_c
R_G
R_c
i^{th} Joint Coordinate System
(JCS_i)

Fig. A-3: Definition of QKC joint geometry charachteristics

Half Cone Angle: $\theta_c := 45 \cdot \mathrm{deg}$

Ball Center Radial Offset: (shown negative in A-3) $O_{SRr} := -0.0752 \cdot \mathrm{in}$

Ball Radius: $R_B := 0.3946 \cdot \mathrm{in}$

Contact Radius: $R_c := R_B \cdot \cos(\theta_c) + O_{SRr}$

Tangential Stiffness/Resistance Coefficients:
set = 0 per assumptions in section 3.6

$\mu_{Tl} := 0$

$\mu_{Ts} := 0$

Groove Contact Angle

$\theta_{contact} = 120 \cdot \mathrm{deg}$

Pre-load Vector
relative to Coupling Coordinate System (CCS):

$$\delta_{preload} := \begin{pmatrix} 0 \dfrac{0.0002}{5.08} \cdot \mathrm{in} \\ 0 \dfrac{0.0002}{5.08} \cdot \mathrm{in} \\ -10 \dfrac{0.0002}{5.08} \cdot \mathrm{in} \end{pmatrix}$$

Error Translation Vector
relative to Coupling Coordinate System (CCS):

$$\delta_{error} := \begin{pmatrix} 0 \dfrac{0.0002}{5.08} \cdot \mathrm{in} \\ 0 \dfrac{0.0002}{5.08} \cdot \mathrm{in} \\ 0 \dfrac{0.0002}{5.08} \cdot \mathrm{in} \end{pmatrix}$$

Rotation Vector and Point of Rotation
relative to Coupling Coordinate System (CCS)

$$\varepsilon := \begin{bmatrix} \left(0 \cdot 10^{-6}\right) \\ \left(0 \cdot 10^{-6}\right) \\ \left(0 \cdot 10^{-6}\right) \end{bmatrix} \cdot \mathrm{rad}$$

$$r_\varepsilon := \begin{pmatrix} 0 \\ 0 \\ 0 \end{pmatrix} \cdot \mathrm{in}$$

$$\delta_c := \delta_{preload} + \delta_{error}$$

VARIABLES FOR CONTACT MECHANICS AND UNIT CONTACT FORCES

VARIABLES FOR NORMAL CONTACT FORCE VS. DISPLACEMENT CURVE FIT:

Joint 1

$b_1 := 1.07$

$c_1 := 1 + b_1$

$K_1 := 2948850 \dfrac{\mathrm{lbf}}{\mathrm{in}^{c_1}}$

Joint 2

$b_2 := 1.07$

$c_2 := 1 + b_2$

$K_2 := 2948850 \dfrac{\mathrm{lbf}}{\mathrm{in}^{c_1}}$

Joint 3

$b_3 := 1.07$

$c_3 := 1 + b_3$

$K_3 := 2948850 \dfrac{\mathrm{lbf}}{\mathrm{in}^{c_1}}$

-------------------------------- END USER INPUT --------------------------------

PROCEED TO END OF SHEET FOR CALCULATED REACTION FORCE/TORQUE

ANGLE LIMITS OF ARC CONTACTS

Arc Contact Angular Limits (used for line contact integration):

$\theta_{jrfinal}$ must ALWAYS be greater than in $\theta_{jrinitial}$ and numeric values of both must be less than or equal to 360 degrees.For example, consider when a contact crosses the x axis (See A-4)

- Incorrect assignment: $\theta_{jrfinal} = 60^{\circ}$ and $\theta_{jrinitial} = 300^{\circ}$
- Correct assignment: $\theta_{jrfinal} = 60^{\circ}$ and $\theta_{jrinitial} = -60^{\circ}$

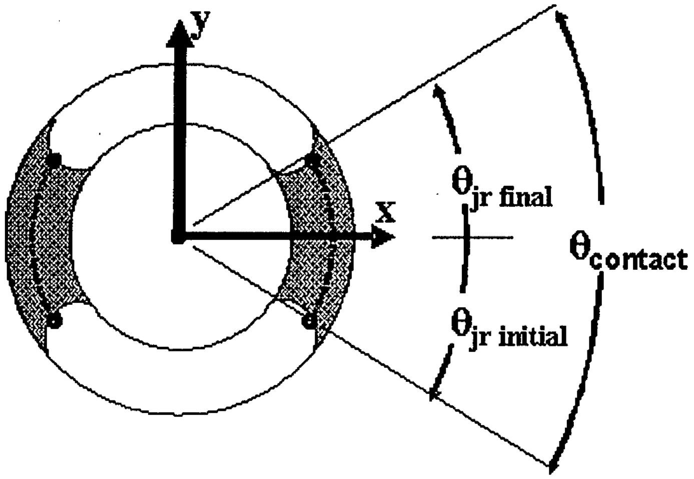

Fig. A-4: Definition of contact angles [i.e. for $\theta_{rf} = 60^{\circ}$ and $\theta_{ri} = -60^{\circ}$]

Joint 1, FIRST ARC, j = 1:

$\theta_{1rinitial} := \theta_1 + \frac{(\pi - \theta_{contact})}{2}$ $\quad \theta_{1rfinal} := \theta_{1rinitial} + \theta_{contact}$ $\quad \theta_{1rinitial} = 120\mathrm{deg}$ $\quad \theta_{1rfinal} = 240\mathrm{deg}$

Joint 1, SECOND ARC, j = 2:

$\theta_{2rinitial} := \theta_{1rinitial} - \pi$ $\quad \theta_{2rfinal} := \theta_{2rinitial} + \theta_{contact}$ $\quad \theta_{2rinitial} = -60\mathrm{deg}$ $\quad \theta_{2rfinal} = 60\mathrm{deg}$

Joint 2, FIRST ARC, j = 3:

$\theta_{3rinitial} := \theta_2 + \frac{(-\pi - \theta_{contact})}{2}$ $\quad \theta_{3rfinal} := \theta_{3rinitial} + \theta_{contact}$ $\quad \theta_{3rinitial} = 0\mathrm{deg}$ $\quad \theta_{3rfinal} = 120\mathrm{deg}$

Joint 2, SECOND ARC, j = 4:

$\theta_{4rinitial} := \theta_{3rinitial} + \pi$ $\quad \theta_{4rfinal} := \theta_{4rinitial} + \theta_{contact}$ $\quad \theta_{4rinitial} = 180\mathrm{deg}$ $\quad \theta_{4rfinal} = 300\mathrm{deg}$

Joint 3, FIRST ARC, j = 5:

$\theta_{5rinitial} := \theta_3 + \frac{(\pi - \theta_{contact})}{2}$ $\quad \theta_{5rfinal} := \theta_{5rinitial} + \theta_{contact}$ $\quad \theta_{5rinitial} = 240\mathrm{deg}$ $\quad \theta_{5rfinal} = 360\mathrm{deg}$

Joint 3, SECOND ARC, j = 6:

$\theta_{6rinitial} := \theta_{5rinitial} - \pi$ $\quad \theta_{6rfinal} := \theta_{6rinitial} + \theta_{contact}$ $\quad \theta_{6rinitial} = 60\mathrm{deg}$ $\quad \theta_{6rfinal} = 180\mathrm{deg}$

CALCULATED POSITION CHANGE OF SYMMETRY INTERCEPTS

$$r_{SI1} := r_{JCS1} + \begin{pmatrix} 0 \\ 0 \\ R_c \cdot \tan(\theta_c) \end{pmatrix} \qquad r_{SI2} := r_{JCS2} + \begin{pmatrix} 0 \\ 0 \\ R_c \cdot \tan(\theta_c) \end{pmatrix} \qquad r_{SI3} := r_{JCS3} + \begin{pmatrix} 0 \\ 0 \\ R_c \cdot \tan(\theta_c) \end{pmatrix}$$

$$r_{1\varepsilon} := r_{SI1} - r_{\varepsilon} \qquad r_{2\varepsilon} := r_{SI2} - r_{\varepsilon} \qquad r_{3\varepsilon} := r_{SI3} - r_{\varepsilon}$$

$$\delta_{SI1} := \delta_c + \varepsilon \times r_{1\varepsilon} \qquad \delta_{SI2} := \delta_c + \varepsilon \times r_{2\varepsilon} \qquad \delta_{SI3} := \delta_c + \varepsilon \times r_{3\varepsilon}$$

$$\delta_{SI1} = \begin{pmatrix} 0.00000 \\ 0.00000 \\ -0.00039 \end{pmatrix} \text{in} \qquad \delta_{SI2} = \begin{pmatrix} 0.00000 \\ 0.00000 \\ -0.00039 \end{pmatrix} \text{in} \qquad \delta_{SI3} = \begin{pmatrix} 0.00000 \\ 0.00000 \\ -0.00039 \end{pmatrix} \text{in}$$

IN-PLANE TRANSLATION OF SYMMETRY INTERCEPTS

$$\delta_{1rmax} := \left[\left(\delta_{SI1_0}\right)^2 + \left(\delta_{SI1_1}\right)^2\right]^{\frac{1}{2}} \qquad \delta_{2rmax} := \left[\left(\delta_{SI2_0}\right)^2 + \left(\delta_{SI2_1}\right)^2\right]^{\frac{1}{2}} \qquad \delta_{3rmax} := \left[\left(\delta_{SI3_0}\right)^2 + \left(\delta_{SI3_1}\right)^2\right]^{\frac{1}{2}}$$

$$\delta_{1rmax} = 0\,\text{in} \qquad \delta_{2rmax} = 0\,\text{in} \qquad \delta_{3rmax} = 0\,\text{in}$$

$$\theta_{1rmax} := \text{atan2}\left(\delta_{SI1_0}, \delta_{SI1_1} + 10^{-99} \cdot \text{in}\right) \qquad \theta_{2rmax} := \text{atan2}\left(\delta_{SI2_0}, \delta_{SI2_1} + 10^{-99} \cdot \text{in}\right)$$

$$\theta_{3rmax} := \text{atan2}\left(\delta_{SI3_0}, \delta_{SI3_1} + 10^{-99} \cdot \text{in}\right)$$

$$\theta_{1rmax} = 90\text{deg} \qquad \theta_{2rmax} = 90\text{deg} \qquad \theta_{3rmax} = 90\text{deg}$$

NORMAL DISPLACEMENT FUNCTIONS

$$\delta_{1n}(\theta_r) := -\delta_{1rmax} \cdot \cos(\theta_r - \theta_{1rmax}) \cdot \cos(\theta_c) + \delta_{SI1_2} \cdot \sin(\theta_c)$$

$$\delta_{2n}(\theta_r) := -\delta_{2rmax} \cdot \cos(\theta_r - \theta_{2rmax}) \cdot \cos(\theta_c) + \delta_{SI2_2} \cdot \sin(\theta_c)$$

$$\delta_{3n}(\theta_r) := -\delta_{3rmax} \cdot \cos(\theta_r - \theta_{3rmax}) \cdot \cos(\theta_c) + \delta_{SI3_2} \cdot \sin(\theta_c)$$

FUNCTIONS FOR UNIT FORCE VS DISTANCE OF APPROACH

$$f_{n1}(\theta_r) := K_1 \cdot \left(\left|\delta_{1n}(\theta_r)\right|\right)^{b_1} \qquad f_{n2}(\theta_r) := K_2 \cdot \left(\left|\delta_{2n}(\theta_r)\right|\right)^{b_2} \qquad f_{n3}(\theta_r) := K_3 \cdot \left(\left|\delta_{3n}(\theta_r)\right|\right)^{b_3}$$

BALL-GROOVE CONTACT ARC FORCES

Provides the force on groove surfaces, NOT the force on the ball surface(s)

JOINT 1, FIRST ARC, j = 1:

$$F_{j1} := R_c \cdot \begin{bmatrix} \displaystyle\int_{\theta_{1rinitial}}^{\theta_{1rfinal}} -f_{n1}(\theta_r) \cdot \left(-\cos(\theta_r) \cdot \cos(\theta_c) - \mu_{Ts} \cdot \sin(\theta_r) + \mu_{Tl} \cdot \cos(\theta_r) \cdot \sin(\theta_c)\right) d\theta_r \\ \displaystyle\int_{\theta_{1rinitial}}^{\theta_{1rfinal}} -f_{n1}(\theta_r) \cdot \left(-\sin(\theta_r) \cdot \cos(\theta_c) + \mu_{Ts} \cdot \cos(\theta_r) + \mu_{Tl} \cdot \sin(\theta_r) \cdot \sin(\theta_c)\right) d\theta_r \\ \displaystyle\int_{\theta_{1rinitial}}^{\theta_{1rfinal}} -f_{n1}(\theta_r) \cdot \left(\sin(\theta_c) + \mu_{Tl} \cdot \cos(\theta_c)\right) d\theta_r \end{bmatrix}$$

JOINT 1, SECOND ARC, j = 2:

$$F_{j2} := R_c \cdot \begin{bmatrix} \displaystyle\int_{\theta_{2rinitial}}^{\theta_{2rfinal}} -f_{n1}(\theta_r) \cdot \left(-\cos(\theta_r) \cdot \cos(\theta_c) - \mu_{Ts} \cdot \sin(\theta_r) + \mu_{Tl} \cdot \cos(\theta_r) \cdot \sin(\theta_c)\right) d\theta_r \\ \displaystyle\int_{\theta_{2rinitial}}^{\theta_{2rfinal}} -f_{n1}(\theta_r) \cdot \left(-\sin(\theta_r) \cdot \cos(\theta_c) + \mu_{Ts} \cdot \cos(\theta_r) + \mu_{Tl} \cdot \sin(\theta_r) \cdot \sin(\theta_c)\right) d\theta_r \\ \displaystyle\int_{\theta_{2rinitial}}^{\theta_{2rfinal}} -f_{n1}(\theta_r) \cdot \left(\sin(\theta_c) + \mu_{Tl} \cdot \cos(\theta_c)\right) d\theta_r \end{bmatrix}$$

$$F_{i1} := F_{j1} + F_{j2}$$

JOINT 2, FIRST ARC, j = 3:

$$F_{j3} := R_c \cdot \begin{bmatrix} \displaystyle\int_{\theta_{3rinitial}}^{\theta_{3rfinal}} -f_{n2}(\theta_r) \cdot \left(-\cos(\theta_r) \cdot \cos(\theta_c) - \mu_{Ts} \cdot \sin(\theta_r) + \mu_{Tl} \cdot \cos(\theta_r) \cdot \sin(\theta_c)\right) d\theta_r \\ \displaystyle\int_{\theta_{3rinitial}}^{\theta_{3rfinal}} -f_{n2}(\theta_r) \cdot \left(-\sin(\theta_r) \cdot \cos(\theta_c) + \mu_{Ts} \cdot \cos(\theta_r) + \mu_{Tl} \cdot \sin(\theta_r) \cdot \sin(\theta_c)\right) d\theta_r \\ \displaystyle\int_{\theta_{3rinitial}}^{\theta_{3rfinal}} -f_{n2}(\theta_r) \cdot \left(\sin(\theta_c) + \mu_{Tl} \cdot \cos(\theta_c)\right) d\theta_r \end{bmatrix}$$

JOINT 2, SECOND ARC, j = 4:

$$F_{j4} := R_c \cdot \begin{bmatrix} \displaystyle\int_{\theta_{4rinitial}}^{\theta_{4rfinal}} -f_{n2}(\theta_r) \cdot \left(-\cos(\theta_r) \cdot \cos(\theta_c) - \mu_{Ts} \cdot \sin(\theta_r) + \mu_{Tl} \cdot \cos(\theta_r) \cdot \sin(\theta_c)\right) d\theta_r \\ \displaystyle\int_{\theta_{4rinitial}}^{\theta_{4rfinal}} -f_{n2}(\theta_r) \cdot \left(-\sin(\theta_r) \cdot \cos(\theta_c) + \mu_{Ts} \cdot \cos(\theta_r) + \mu_{Tl} \cdot \sin(\theta_r) \cdot \sin(\theta_c)\right) d\theta_r \\ \displaystyle\int_{\theta_{4rinitial}}^{\theta_{4rfinal}} -f_{n2}(\theta_r) \cdot \left(\sin(\theta_c) + \mu_{Tl} \cdot \cos(\theta_c)\right) d\theta_r \end{bmatrix}$$

$$F_{i2} := F_{j3} + F_{j4}$$

JOINT 3, FIRST ARC, j = 5:

$$F_{j5} := R_c \cdot \begin{bmatrix} \displaystyle\int_{\theta_{5rinitial}}^{\theta_{5rfinal}} -f_{n3}(\theta_r) \cdot \left(-\cos(\theta_r) \cdot \cos(\theta_c) - \mu_{Ts} \cdot \sin(\theta_r) + \mu_{Tl} \cdot \cos(\theta_r) \cdot \sin(\theta_c)\right) d\theta_r \\ \displaystyle\int_{\theta_{5rinitial}}^{\theta_{5rfinal}} -f_{n3}(\theta_r) \cdot \left(-\sin(\theta_r) \cdot \cos(\theta_c) + \mu_{Ts} \cdot \cos(\theta_r) + \mu_{Tl} \cdot \sin(\theta_r) \cdot \sin(\theta_c)\right) d\theta_r \\ \displaystyle\int_{\theta_{5rinitial}}^{\theta_{5rfinal}} -f_{n3}(\theta_r) \cdot \left(\sin(\theta_c) + \mu_{Tl} \cdot \cos(\theta_c)\right) d\theta_r \end{bmatrix}$$

JOINT 3, FIRST ARC, j = 6 :

$$F_{j6} := R_c \cdot \begin{bmatrix} \displaystyle\int_{\theta_{6rinitial}}^{\theta_{6rfinal}} -f_{n3}(\theta_r) \cdot \left(-\cos(\theta_r) \cdot \cos(\theta_c) - \mu_{Ts} \cdot \sin(\theta_r) + \mu_{Tl} \cdot \cos(\theta_r) \cdot \sin(\theta_c)\right) d\theta_r \\ \displaystyle\int_{\theta_{6rinitial}}^{\theta_{6rfinal}} -f_{n3}(\theta_r) \cdot \left(-\sin(\theta_r) \cdot \cos(\theta_c) + \mu_{Ts} \cdot \cos(\theta_r) + \mu_{Tl} \cdot \sin(\theta_r) \cdot \sin(\theta_c)\right) d\theta_r \\ \displaystyle\int_{\theta_{6rinitial}}^{\theta_{6rfinal}} -f_{n3}(\theta_r) \cdot \left(\sin(\theta_c) + \mu_{Tl} \cdot \cos(\theta_c)\right) d\theta_r \end{bmatrix}$$

$$F_{i3} := F_{j5} + F_{j6}$$

FORCE ON EACH ARC CONTACT AND BETWEEN BALL AND GROOVE

$F_{j1} = \begin{pmatrix} -116 \\ 0 \\ -140 \end{pmatrix} \text{lbf}$ $F_{j2} = \begin{pmatrix} 116 \\ 0 \\ -140 \end{pmatrix} \text{lbf}$ $F_{i1} = \begin{pmatrix} 0 \\ 0 \\ -279 \end{pmatrix} \text{lbf}$

$F_{j3} = \begin{pmatrix} 58 \\ 100 \\ -140 \end{pmatrix} \text{lbf}$ $F_{j4} = \begin{pmatrix} -58 \\ -100 \\ -140 \end{pmatrix} \text{lbf}$ $F_{i2} = \begin{pmatrix} -0 \\ 0 \\ -279 \end{pmatrix} \text{lbf}$

$F_{j5} = \begin{pmatrix} 58 \\ -100 \\ -140 \end{pmatrix} \text{lbf}$ $F_{j6} = \begin{pmatrix} -58 \\ 100 \\ -140 \end{pmatrix} \text{lbf}$ $F_{i3} = \begin{pmatrix} 0 \\ 0 \\ -279 \end{pmatrix} \text{lbf}$

REACTION FORCE AND TORQUE

$F_{Reaction} := F_{j1} + F_{j2} + F_{j3} + F_{j4} + F_{j5} + F_{j6}$

$$\boxed{F_{Reaction} = \begin{pmatrix} 0 \\ 0 \\ -838 \end{pmatrix} \text{lbf}}$$

$$F_{radial} := \left[\left(F_{Reaction_0}\right)^2 + \left(F_{Reaction_1}\right)^2 \right]^{\frac{1}{2}}$$

$$\boxed{F_{radial} = 0 \, \text{lbf}}$$

$T_{Reaction} := r_{SI1} \times F_{i1} + r_{SI2} \times F_{i2} + r_{SI3} \times F_{i3}$

$$\boxed{T_{Reaction} = \begin{pmatrix} 0 \\ 0 \\ 0 \end{pmatrix} \text{in} \cdot \text{lbf}}$$

VERIFY CONSTANT CONTACT CONDITION

Should the any of these graphs cross $\delta_{ni}(\theta_r) = 0$; the analysis is not valid

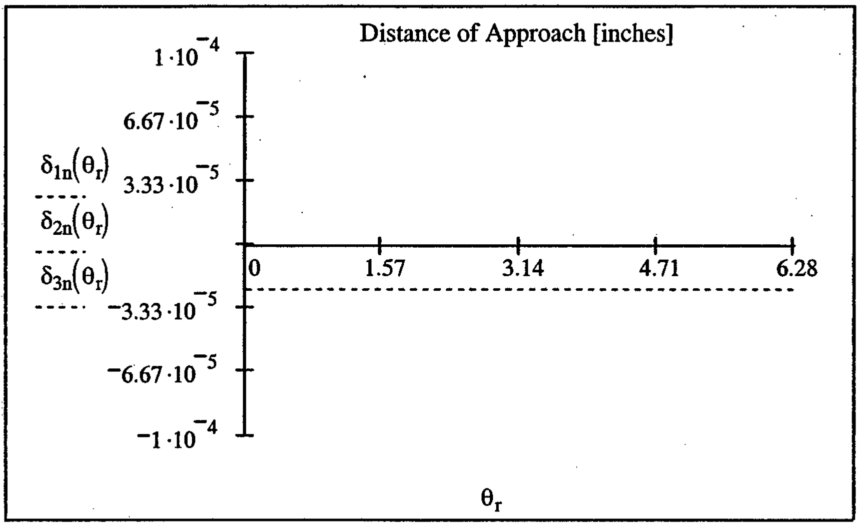

Fig. A-5: Constant Contact Assumption Monitor Plot

STIFFNESS CALCULATION

PROCEDURE (LINEARIZE FOR SMALL DISPLACEMENTS):

- IMPOSE PRELOAD ON THE JOINT, RECORD CORRESPONDING REACTION (R_1)
- IMPOSE AN ERROR Δ_ε (LINEAR OR ROTARY) & RECORD CORRESPONDING REACTION (R_2)

k ~ absolute $| (R_2-R_1) / \Delta_\varepsilon |$

References

[1] Slocum AH. Kinematic couplings for precision fixturing -Part I: Formulation of design parameters. Prec Eng 1988;10;85-91.

[2] Slocum AH. Design of three-groove kinematic couplings. Prec Eng 1992;14;67-73.

[3] Slocum AH, Mueller L, Braunstein D. Flexural mount kinematic couplings and method. United States Patent 5,678,944.

[4] Culpepper ML, Slocum AH, Shaikh FZ. Compliant kinematic couplings for use in manufacturing and assembly. Proceedings of the 1998 ASME International Mechanical Engineering Congress and Exposition, Anaheim, CA. 1998. pp. 611-18.

[5] Suh NP. In pursuit of the lower limit of friction coefficient in dry sliding. Proceedings of the 1993 ASME Winter Annual Meeting, New Orleans, LA. 1993. pp. 1-8.

[6] Johnson KL. Deformation of a plastic wedge by a rigid flat die under the action of a tangential force. Journal of Mechanics and Physics of Solids. 1968. pp. 395-402.

[7] Childs TH. The persistence of asperities in indentation experiments. Wear. 1973. pp. 3-17.

[8] Schmiechen P, Slocum AH. Analysis of kinematic systems: A generalized approach. Prec Eng 1996;19;11-18.

[9] Hale LC, Slocum AH. Optimal design techniques for kinematic couplings. Prec Eng;25;114-27.

[10] Schouten CH, Rosielle PCJN, Schellekens PHJ. Design of a kinematic coupling for precision applications. Prec Eng;20;46-52.

[11] Johnson KL. Contact mechanics. Cambridge, United Kingdom. Cambridge University Press. 1985. pp. 85-9.

[12] Hale LC. Principles and techniques for designing precision machines. PhD Thesis. Cambridge, MA. MIT. 1999. pp. 422.

[13] Oiwa T, Kyusojin A. Development of precise cylindrical grinding by ball centers-contact stiffness between ball and centre hole. Prec Eng 1999;12;37-42.

[14] Culpepper ML, Slocum AH, Shaikh FZ. Quasi-kinematic couplings for precision automotive assemblies. Proceedings of the 1999 ASME-ICE Fall Conference, Ann Arbor, MI. 1999. pp. 61-6.

[15] Culpepper ML. Design and application of compliant quasi-kinematic couplings. PhD Thesis. Cambridge, MA. MIT. 2000. pp. 89-108.

[16] Slocum AH, Donmez A. Kinematic couplings for precision fixturing- Part 2: Experimental determination of repeatability and stiffness. Prec Eng 1988;10;115-22.

Submitted to the ASME Journal of Mechancial Design, September 2002

Quasi-kinematic Couplings for Low-cost Precision Alignment of High-volume Assemblies

Martin L. Culpepper[1*], Alexander Slocum[2] and F. Zafar Shaikh[3]

1. Precision Systems Design & Manufacturing Lab
Massachusetts Institute of Technology
Cambridge, MA 02139
culpepper@mit.edu

2. Precision Engineering Research Group
Massachusetts Institute of Technology
Cambridge, MA 02139
slocum@mit.edu

3. Scientific Research Laboratory
Ford Motor Company
Dearborn, MI 48120
fshaikh@ford.com

Abstract

Quasi-kinematic couplings (QKCs) are alignment devices that incorporate elastic averaging and exact constraint principles to achieve low-cost precision alignment. This paper shows QKCs can be used for low-cost precision alignment in high-volume assembly applications. This is demonstrated via case study of the alignment process of automotive main journal bearings. Results of experiments show QKC performance of 0.35 microns compared to 4.85 microns for a dowel pin alignment design. Statistical analyses predict the QKC will meet 5 micron alignment requirements in 99.999% of all assembly cycles. Compared to the pin-hole design, the QKC uses 60% fewer piece parts and costs 36% less.

Keywords: Kinematic coupling, quasi-kinematic coupling, alignment, assembly, fixture, repeatability, stiffness, assembly, precision, automotive, elastic averaging

---

1. INTRODUCTION

Precision alignment is often a main cause of yield, cost and performance problems in medium and high-volume assembly processes. For instance, the cost associated with photonic component alignment can exceed more than half of the product cost while assembly process yields may be as low as 10%. Other industries such as automotive and aerospace face similar alignment problems in engines, frame assembly and sheet metal assemblies. The problems with cost, yield, and performance stem from the use of "off the shelf" alignment technologies that are not well suited to the combination of low-cost and precision. For instance, pin-hole joints are often used even though they are usually not stiff enough to prevent micron

---

[*] Corresponding author: Phone: 617 452 2395; Fax: 509 693 0833

level misalignments from assembly loads. These joints can also suffer from cost and quality problems due to their over constrained nature.

Precision alignment requires the kinematic constraint of six degrees of freedom. This can be accomplished by establishing six points of contact via the kinematic couplings in Fig. 1. Unfortunately, these couplings are not suited to high-volume applications which require sealing between components. This has been addressed for some applications by flexural kinematic couplings [1] [2], but these devices are not well-suited for mass production due to the cost of integrated flexures.

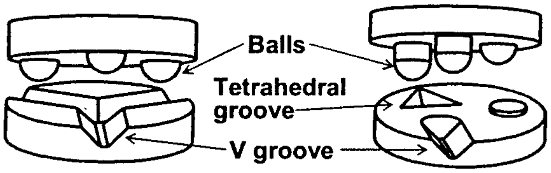

Fig. 1: Three-groove and flat-groove-tetrahedron kinematic coupling types

A new alignment device, the quasi-kinematic coupling (QKC), is specially designed to meet simultaneous low-cost and micron level precision requirements. The coupling utilizes plastic deformation to form itself in place (minimizes precision fabrication costs) and to allow the aligned components to be clamped together (sealing contact) [3] [4] [5]. Although QKCs have achieved ¼ micron alignment performance in controlled experiments [6], proving the hypothesis that QKCs can be used in product-driven applications requires examination of cost constraints and the effects of manufacturing variation. With this paper we use a case study to prove this hypothesis via experimental and statistical treatment of alignment performance.

2. QUASI-KINEMATIC COUPLING CONCEPT

2.1. Description of the QKC concept

The QKC shown in Fig. 2 is designed to emulate the constraint characteristics of a three-groove kinematic coupling. While the three-groove coupling forms six point contacts, the axi-symmetric balls and grooves of the quasi-kinematic couplings form six arcs of contact. Although quasi-kinematic couplings are technically over constrained, clever design can produce a weakly over constrained mate which emulates a kinematic coupling mate [6]. This is done by minimizing the length of the contact arcs (which decreases coupling stiffness) until a desired level of coupling stiffness is reached. The benefits of switching from kinematic to the QKC design include lower assembly and fabrication costs of the axi-symmetric balls and grooves. In addition, the costs associated with reducing alignment hysteresis (from friction and surface finish effects) are minimized through a well-known brinelling technique [7] [8] [9].

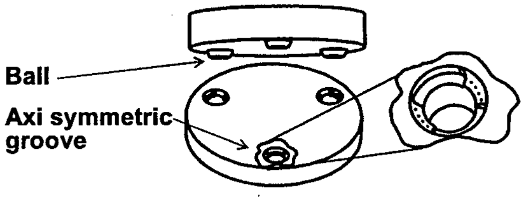

Fig. 2: Quasi-kinematic coupling (contact arcs shown as dotted lines)

2.2. Function of QKCs

Cross sections of a QKC joint in various states are shown in Fig. 3. The "ball" (in cross hatch) is a crowned insert which is pressed into the top component. The initial separating gap in Fig. 3B must exist to ensure that all ball-groove contacts engage. Although the six arc contacts can be made to provide several hundred $^{N}/_{micron}$ stiffness, additional stiffness, load capacity and sealing contact can be obtained when a preload source (for instance the bolt in Fig. 3C) forces the ball-groove material to comply, thereby closing the gap. Application of sufficient preload causes contact between the aligned components to assume all motion constraint and provide a sealed interface. In Fig. 3D, the preload has been removed and a portion of the gap restored by elastic recovery of the ball and groove materials. This is necessary to prepare the QKC for subsequent alignment cycles. This three-piece joint design is used in the case study.

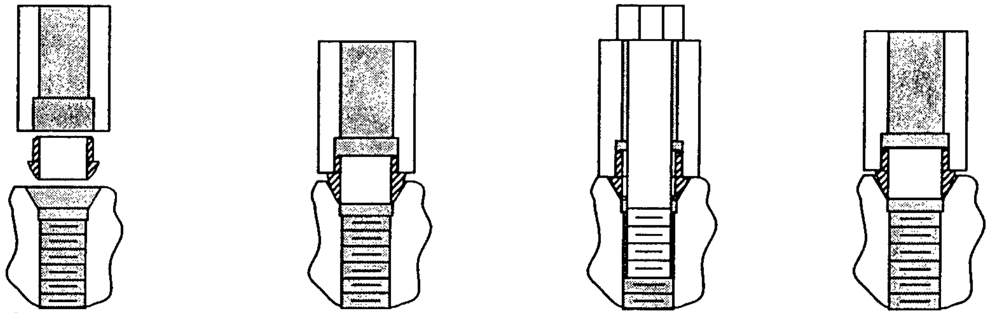

A: Joint components B: Mated joint C: Bolt closes joint D: Gap recovers

Fig. 3: Mating cycle of a QKC joint

Two designs that can be used to achieve six arcs of contact (assuming three joints are used) are shown in **Fig.** 4. The significance of the contact imprints in the figure will be addressed in section 5.2.

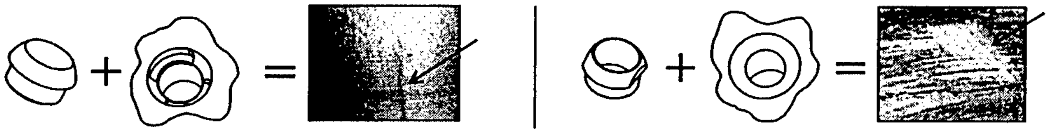

A: Groove relieved B: Ball relieved

Fig. 4: QKC joint designs and corresponding contact imprint patterns

3. CASE STUDY: FORD DURATEC ENGINE ASSEMBLY

3.1. Description of Duratec journal bearing alignment

The Duratec is a high-performance six cylinder engine made in quantities of ~ 300, 000 units/year. The Duratec's crank shaft and main journal bearings are housed between the block and bedplate. A block and bedplate pair is shown partially assembled in **Fig.** 5A. A monolithic bedplate design, with cast-in main bearing caps, is used to decrease the number of parts which must be assembled. The means used to manufacture and align the components must limit the half bore centerline misalignment, δ_r (shown in **Fig.** 5B), to less than ± 5 microns. Failure to do so may results in unacceptable levels of bearing friction (low fuel economy) and low bearing load capacity.

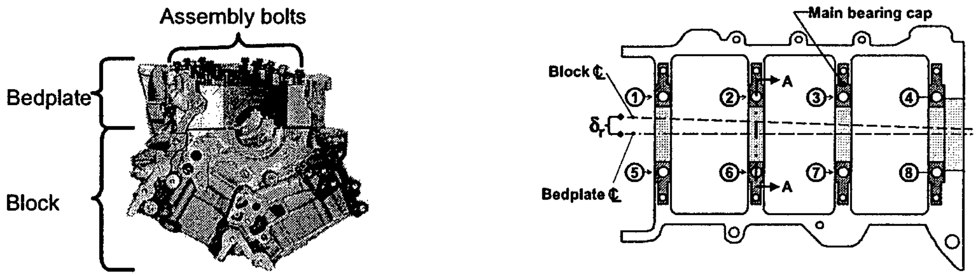
Assembly bolts
Bedplate
Block
Main bearing cap
Block ℄
δ_r
Bedplate ℄
A
A
①
②
③
④
⑤
⑥
⑦
⑧

A: Block-bedplate assembly B: Centerline misalignment, δ_r and dowel pin locations

Fig. 5: Main components affecting Duratec journal bearing alignment

3.2. Original design and assembly process

In the original design, alignment was achieved using 8 pin-hole joints. The parts were then clamped in place via the assembly bolts shown in **Fig.** 5. The rough geometry of the half bores were then simultaneously finished machined. Although two dowel pin joints may seem sufficient to align this design, the elastic averaging of 8 pin-hole joints was required to achieve reasonable repeatability. The location and configuration of the pin-hole joints are shown in **Fig.** 5B and Fig. 6 respectively. Although the 8 pin-hole design meets the 5 micron alignment specifications (4.85 microns), the design is grossly over constrained and thus tight tolerances on the size (± 0.008 mm) and placement (± 0.04 mm) of 16 holes are required.

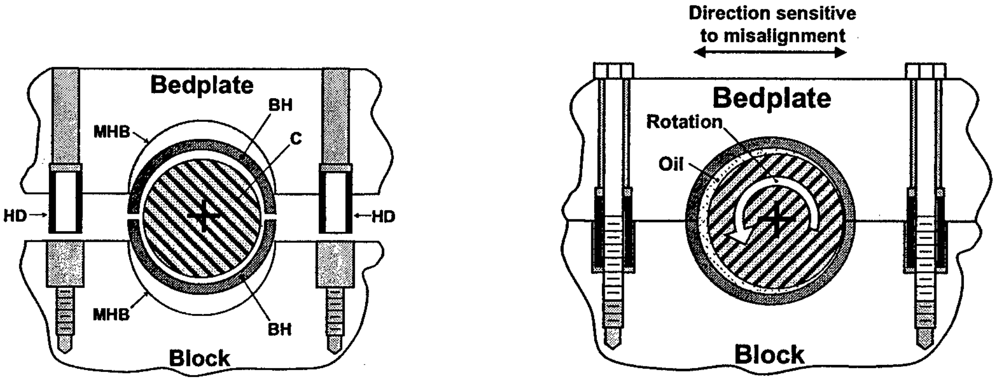
Bedplate
BH
MHB
C
HD
HD
MHB
BH
Block
Direction sensitive to misalignment
Bedplate
Rotation
Oil
Block

A: During final assembly B: In operation

HD = Hollow dowel
MHB = Machined half bore
C = Crank journal
BH = Bearing half

Fig. 6: Cross section through conventional journal bearing assembly (Section A-A in Fig. 5B)

3.3. Main design requirements and constraints for the Duratec alignment and clamping system

Design requirements and constraints are summarized in Table 1 and Table 2 respectively.

Table 1: Main design requirements for engine alignment and clamping

Requirement		Explanation
1.	-5 microns < δ_r < 5 microns	Required for acceptable bearing friction and load capacity
2.	Bolt preload = 9850 ± 1150 $^{lbf}/_{bolt}$	Required to ensure load capacity and prevent fatigue of bolts

Table 2: Main design constraints for engine alignment and clamping

Constraint		Explanation
1.	No change in major equipment	Proving new equipment would require a plant shut down
2.	Balls installed at old pin locations	Manufacturing line was designed to work around protruding hollow dowel pins so the QKC balls must reside within these areas to prevent interference with existing equipment
3.	Cost less than pin-hole design	Total cost per engine must not increase
4.	Sealed block-bedplate interface	Intimate contact (with sealant) required to prevent oil leaks

4. DESIGN AND IMPLEMENTATION

The main design challenges and decisions are reflected in the following sub-sections. These decisions are driven by the desire to minimize alignment error, so it is best to start the design process by quantifying sources of error.

4.1. Root sources of alignment error

The major contributors to assembly alignment error are provided in Table 3. The following sub-sections provide brief explanations of some of the sources and their effects on alignment.

Table 3: Sources of variation affecting alignment error

Load	Distribution	Mean	Standard Deviation
Separating gap	Normal	225 microns	$\sigma = 25$ microns
Journal 1 measured hysteresis error*	Normal	0 microns	$\sigma = 0.02$ microns
Journal 4 measured hysteresis error*	Normal	0 microns	$\sigma = 0.06$ microns
Coefficient of friction	Normal	0.09	$\sigma = 0.013$
$F_{c\text{-shear}}$	Normal	0 N	$\sigma = 30$ N
Direction of $F_{c\text{-shear}}$	Uniform	Values between 0° and 360° equally likely	

*Measured via alignment test where other sources of variation were tightly controlled.

Bearing crush force

The bearing halves are sized so that their end faces contact before the block and bedplate. This is done to load the bearings and "crush" them; thereby properly conforming them to the shape of the machined half bore geometries. This process, bearing crush, starts at a block-bedplate separation of 150 microns and continues until the bedplate and block make contact. The reaction force between the bearing halves, the crush force, can be a source of alignment variation. When corresponding bearing halves are symmetrically oriented about the bedplate-block contact plane (*x-y* plane in **Fig.** 7), the bearing crush force is perpendicular to the contact plane and therefore does not act to shear the bedplate and block. In practice, the bearing halves will be rotated in the bore and some fraction of the crush force, $F_{c\text{-}shear}$, can act to shear the block and bedplate. As the amount and direction of the bearing rotation within the half bores can vary, $F_{c\text{-}shear}$ can vary in magnitude and direction. This is indicated by "double pointing" arrows in **Fig.** 7.

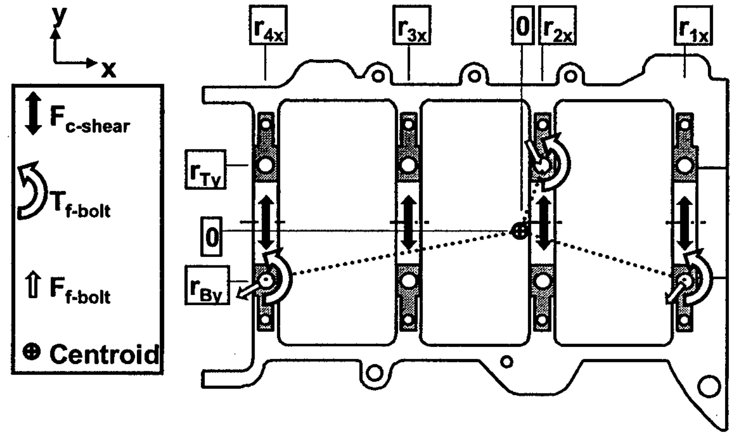

r_{1x} = 0.116 m
r_{2x} = 0.007 m
r_{3x} = -0.095 m
r_{4x} = -0.204 m
r_{Ty} = 0.048 m
r_{By} = -0.041 m

Fig. 7: Assembly loads on bedplate

Local joint gap

Variation in gap between the block and bedplate leads to variation in the bolt force required to close the gap. This can translate into variations in the friction torque, $T_{f\text{-}bolt}$, and friction side load, $F_{f\text{-}bolt}$, exerted between the bolt head and bedplate. These loads, shown in **Fig.** 7, can lead to relative movement between the block and bedplate. The direction of $F_{f\text{-}bolt}$ may also contribute to variation in aligned position. It is assumed that it is equally likely that $F_{f\text{-}bolt}$ may act in any direction parallel to the contact plane.

The upper bound on gap is set by contact stresses in the 12L14 steel balls and 319 aluminum grooves in the block. Experiments show contact stresses in the balls and grooves are acceptable for an upper gap limit of 300 microns [10]. The specifications for the gap were subsequently set at 225 ± 75 microns which is within the capability of the existing manufacturing equipment.

4.2. Joint locations and contact arc orientations

Joint location

Positioning the joints (see Fig. 3 for review of joint geometry) such that they form the largest triangle possible provides maximum resistance to variations in torque loads on the bedplate. Given constraint number two from Table 2, the best joint locations are shown in Fig. 8A and Fig. 8B.

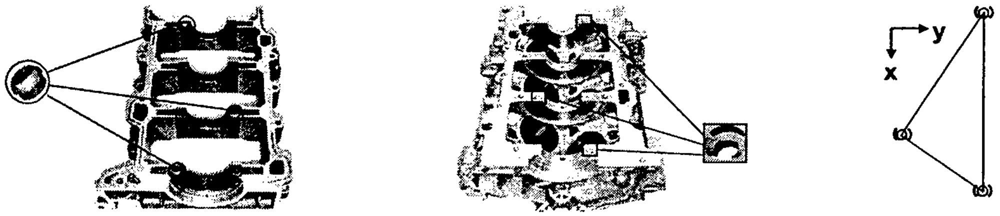

A: Bedplate B: Block C: Joint orientation

Fig. 8: Position and orientation of QKC joints in the Duratec block and bedplate

Using these positions allows the QKC balls to be press fit into holes which previously held the old dowel pins (i.e. no tooling change). Given the tooling shown in Fig. 9, the grooves can be simultaneously produced at the same time holes are drilled for the assembly bolts. In the figure, cast-in or machined reliefs are machined with a form tool to produce a relieved groove design.

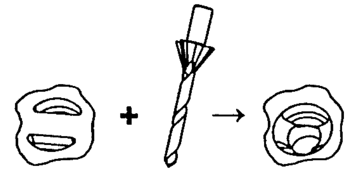

Fig. 9: Form tool used to make concentric grooves and thru-holes

Contact orientation

The orientation of the arc contacts, shown in **Fig.** 8C, was set to provide maximum stiffness to oppose δ_r in the y direction. In this orientation, the arc contacts provide enough constraint along the axis of the crank bore to achieve sufficient repeatability. Though it may seem this design over constrains the alignment, the balls were designed so that they plastically deform during the first mate, thereby forming themselves to match the pattern of the grooves.

4.3. Joint and coupling stiffness

Quasi-kinematic coupling stiffness theory [6] was used to develop joint designs with the required stiffness characteristics. In **Fig.** 10 the in-plane stiffness of an individual joint has been superimposed over the joint's groove to help show how in-plane stiffness varies with direction.

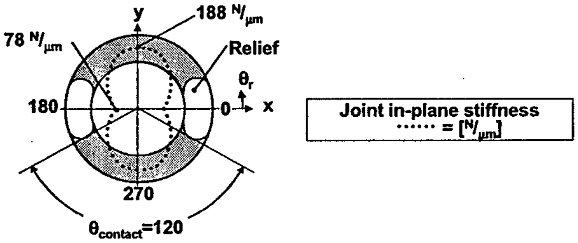

Fig. 10: Stiffness characteristics of a Duratec QKC joint

These stiffness characteristics were used in combination with quasi-kinematic coupling theory and joint locations/orientations from section 4.2 to determine overall coupling stiffness:

$$\begin{bmatrix} k_x \\ k_y \\ k_{\theta z} \end{bmatrix}_{@\, centroid} = \begin{bmatrix} 234 \, {}^{N}\!/_{micron} \\ 563 \, {}^{N}\!/_{micron} \\ 9.1 \, {}^{N-m}\!/_{microradian} \end{bmatrix} \tag{1}$$

Given the coupling stiffness, loads on the bedplate and the model of load-bedplate interaction in **Fig.** 7, alignment errors can be calculated by dividing the total force/torque on the bedplate by the appropriate coupling stiffness.

5. CONTROLLED EXPERIMENTS FOR BEST CASE PERFORMANCE VERIFICATION

5.1. Test set up and procedure

The setup used to characterize alignment performance is shown in **Fig.** 11. In-plane movements between the block and bedplate were determined by measuring the relative movement of the block and bedplate fixtures (rigidly attached to respective components) with three capacitance probes. Each trial consisted of taking position readings, disassembling the components, reassembling them, and then taking a final reading. To avoid clamping-in errors, the bolts through the three QKC joints were tightened before other assembly bolts. Sources of alignment variation were either eliminated (bearings were removed) or minimized by careful application of bolt torques.

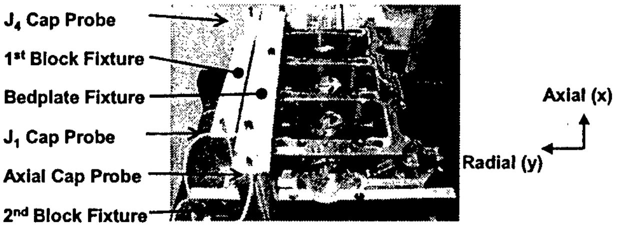

Fig. 11: Test stand for Duratec alignment experiments

5.2. Choice of relieved ball design over relieved groove design

The relieved groove design has advantages with respect to fabrication (reliefs can be cast-in) and assembly (balls do not require orientation). However, it was not clear if there would be a difference in alignment hysteresis due to the difference in geometries of the two joint designs. An experiment was conducted to determine which of the QKC joint designs in **Fig.** 4 would provide the best performance. The results of alignment tests are shown in **Fig.** 12A (previously reported in [5]) and **Fig.** 12B. It is clear the relieved ball design works best. The reason lies in the difference between the deformed shaped of the balls. When the ball in **Fig.** 4A is pressed into the relieved groove, the ball deforms over the edge of the groove relief which then leaves a sharp imprint in the ball surface. In contrast, the relieved ball design shows signs of asperity brinelling, but does not exhibit a concentrated impression. We hypothesize that the high stress and sliding contact between ball and relieved groove at the sharp imprints leads to the generation of wear particles. These particles interfere with the ball-groove mate, thereby increasing mating hysteresis. The absence of wear particles in the relieved ball design and their presence [10] in relieved groove experiments supports this hypothesis.

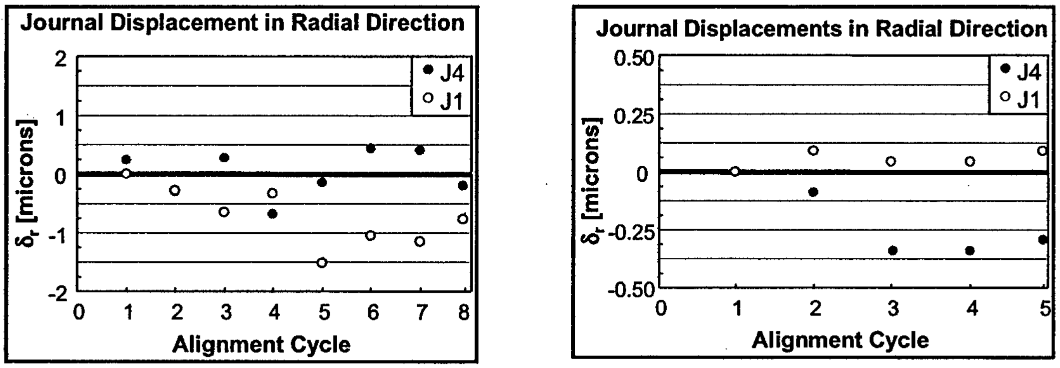

A: Groove relieved B: Ball relieved

Fig. 12: Alignment hysteresis at journals 1 and 4 for competing QKC joint designs

5.3. Comparison between pin-hole and QKC design

The characteristics and performance of the pinned and QKC designs are listed in Table 4. The increase in feature placement tolerance is due to the ability of the QKC to reduce mismatch between the ball and groove patterns via their form-in-place quality. The reduction in cost is due in large part to the reduction in precision pieces, e.g. three screw machined pegs vs. 8 precision ground pins.

Table 4: Comparison of engine alignment designs obtained from controlled experiment

Design characteristics	Pinned joint design	Quasi-kinematic design
Precision pieces	8 dowel pins	3 balls
Precision features	16 holes	3 holes and 3 grooves
Feature placement tolerance	± 0.04 mm	± 0.08 mm
Average centerline error range*	4.85 microns	0.35 microns
Normalized cost per engine**	1.00	0.64

*Average of journal 1 and 4 alignment error ranges ** Based upon 300,000 engines/year

5.4. Design compatibility with manufacturing process and long-term validation of prototype engine

It was necessary to verify that the design was compatible with the existing manufacturing line. This was done by fabricating two block and bedplate pairs equipped with QKC elements, then sending them through the existing manufacturing line. The QKC block-bedplate pairs were inserted after operations where the dowel pin holes were manufactured. One of the engines has been placed in a test car which has logged over 60,000 miles to date and is still in operation. The other engine was disassembled to look for any assembly irregularities due to the new design. No irregularities were found.

6. EFFECT OF PROCESS VARIATIONS ON ALIGNMENT PERFORMANCE

6.1. Statistical modeling and analysis

A statistical analysis was performed via a spread sheet that uses the data in Table 3 to assign gaps, bearing forces and friction loads as random variables. A copy of the spread sheet is provided in the appendix. The random variables, the model shown in **Fig.** 7 and coupling stiffness characteristics are then used to calculate alignment error. Within the model, $F_{f\text{-}bolt}$ may be less than the maximum value of sliding friction possible between the bolt head and bedplate. A friction fraction coefficient, α, is used to capture this in the model. When $\alpha = 1$, friction side loads can be (though they are random variables) the maximum value of sliding friction. When $\alpha = 0$, friction side loads do not exist. Though unlikely, this could happen if the axis of the bolt and axis of the wrench spindle are always coincident. In practical applications, α can be used to capture the effect of flexible couplings or compliance between bolt and spindle which mitigates mismatch between the rotation axis of the wrench spindle and a bolt's rotation axis.

6.2. Results of statistical analyses

Results showed the most variation in alignment at the 4th journal bearing. The frequency plot and statistical data for $\alpha = 1$ are shown in **Fig.** 13. The bimodal shape is a result of two "sub-populations" of likely alignment positions; the first is associated with displacement due to the sum of torques and the second due to the sum of forces. One can think of this in the following terms, it is very likely that a force, torque or combination of the two will lead to non-zero alignment error. Specific combinations of forces and torques are required to achieve near zero alignment error. Given the bimodal shape, it is misleading to rely solely on the mean and standard deviation of the analysis when quantifying alignment performance. Instead, we consider the number of trials that fall within the bounds of the 5 micron alignment requirements and find that 99.999% of all cases fall within specification.

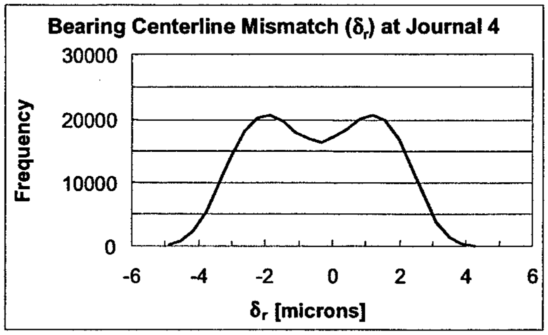

Journal 4 radial alignment (δ_r) for $\alpha = 1$

Mean	-0.4 microns
σ	1.8 microns
Minimum δ_r	-5.1 microns
Maximum δ_r	4.2 microns
-5 < % trials < 5 microns	99.999 %

Fig. 13: Results of statistical alignment analysis ($\alpha = 1$)

Results for other values of α are summarized in Table 5. These results show how important the management of $F_{f\text{-}bolt}$ is to improving alignment in the Duratec QKC.

Table 5: Effect of α on journal 4 alignment error (δ_r in microns)*

α	Mean	σ	Minimum	Maximum
0.0	-0.3	0.2	-1.1	0.7
0.1	-0.4	0.3	-1.5	0.8
0.5	-0.4	0.9	-2.7	2.8
1.0	-0.4	1.8	-5.1	4.2

*Note, $T_{f\text{-}bolt}$ is not affected by α as rotary sliding contact always occurs between bolt and bedplate during clamping

7. CONCLUSIONS

The results of this work show that QKCs can be used to achieve low-cost precision alignment (better than 5 microns) in high-volume assembly applications. Experimental results showed 0.35 micron alignment repeatability when sources of variation are controlled. This is a significant improvement over the 4.85 microns capability of the previous alignment design. Statistical analyses of worst case assembly process variations showed the QKC will meet 5 micron alignment requirements in 99.999% of all assembly cycles. Compared to the original alignment design, the QKC design uses 60% fewer piece parts, costs 36% less and possesses feature placement/size tolerances that are twice as large. Prototype engines equipped with QKCs were manufactured with existing equipment to prove design compatibility with the existing engine manufacturing process. A prototype engine equipped with a QKC has powered a test car for over 60, 000 miles to date and continues to run without complications.

8. ACKNOWLEDGMENTS

Funding for this work was provided by the Ford Motor Company and a grant from the Defense Logistics Agency AQP. The authors wish to thank them for their financial and technical assistance.

9. REFERENCES

[1] Culpepper, M. L., Slocum, A. H., Shaikh, F. Z., "Compliant Kinematic Couplings for Use In Manufacturing And Assembly," Proceedings of the 1998 ASME International Mechanical Engineering Congress and Exposition.

[2] Slocum, A. H., Mueller, L., Braunstein, D., 1997, "Flexural Mount Kinematic Couplings and Method", United States Patent No. 5,678,944, pp. 1 - 10.

[3] Culpepper, M. L., Slocum, A. H., "Quasi-Kinematic Coupling and Method for Use in Assembling and Locating Mechanical Components and the Like," US Patent No. 6, 193, 430, February 2001.

[4] Culpepper, M. L., Slocum, A. H., Shaikh, F. Z. and Vrsek, G., "Quasi-Kinematic Couplings for Use in Automotive Assembly," Issued under US Serial No. 09293-442.

[5] Culpepper M. L., Slocum A. H., Shaikh, F. Z., "Quasi-kinematic Couplings for Precision Automotive Assemblies", Proceedings of the 1999 ASME-ICE Fall Conference, Ann Arbor, MI, 1999, pp. 61-6.

[6] Culpepper M. L., "Design of Quasi-Kinematic Couplings", Submitted to Precision Engineering 2002. Draft available at: http://psdam.mit.edu/patents-publications/Design%20of%20Quasi-Kinematic%20Couplings.pdf.

[7] Bald, H., Wulf, Witte, "Positioning Device," U.S. Patent No 4 070 120, 1978.

[8] Johnson, K. L., "Deformation of a Plastic Wedge by a Rigid Flat Die Under the Action of a Tangential Force", Journal of Mechanics and Physics of Solids, 1968, pp. 395 - 402.

[9] Childs, T. H., "The Persistence of Asperities in Indentation Experiments", Wear, 1973, pp. 3 - 17.

[10] Culpepper M. L., "Design and Application of Compliant Quasi-kinematic Couplings", PhD Thesis, Cambridge, MA, MIT, 2000, pp. 89-108.

10. APPENDIX: SPREADSHEET FOR STATISTICAL ANALYSIS

Duratec QKC Statistical Repetabilty Analysis

Martin Culpepper

Mating gap and bolt force

	Initial gap Minimum microns	Mean microns	Maximum microns	σ microns	Value microns	Final gap Value microns	Fbolt Value N
Journal 1-Top	0	0	0	0	0	0	0
Journal 1-Bot	**150**	225	**300**	25	**155**	35	3357
Journal 2-Top	150	225	300	25	**177**	38	3609
Journal 2-Bot	0	0	0	0	0	0	0
Journal 3-Top	0	0	0	0	0	0	0
Journal 3-Bot	0	0	0	0	0	0	0
Journal 4-Top	0	0	0	0	0	0	0
Journal 4-Bot	150	225	300	25	**255**	47	4511

Crush force

	Fcrush Minimum N	Mean microns	Maximum N	σ microns	Value Fx N	Value Fy N
Journal 1-Top	0	0.0	0.0	0	0	0
Journal 1-Bot	**-90.0**	0.0	**90.0**	30	0	**90**
Journal 2-Top	-90.0	0.0	90.0	30	0	**1**
Journal 2-Bot	0.0	0.0	0.0	0	0	0
Journal 3-Top	-90.0	0.0	90.0	30	0	**10**
Journal 3-Bot	0.0	0.0	0.0	0	0	0
Journal 4-Top	-90.0	0.0	90.0	30	0	**-50**
Journal 4-Bot	0	0	0	0	0	0

Bolt head friction loads **α: 1.00** Friction fraction coefficient (at max is 1, meaning full friction loads apply)

	Coefficient of friction Minimum —	Mean —	Maximum —	σ —	Value —	Ffriction Value N	θ_{Fbolt} radians	Fx N	Fy N	Tbolt Value N-m
Journal 1-Top	0.00	0.00	0.00	0.00	0.00	0	0.00	0	0	0
Journal 1-Bot	**0.05**	0.09	**0.12**	0.01	**0.07**	235	**3.00**	-233	33	0
Journal 2-Top	0.05	0.09	0.12	0.01	**0.10**	361	**2.80**	-340	121	0
Journal 2-Bot	0.00	0.00	0.00	0.00	0.00	0	0.00	0	0	0
Journal 3-Top	0.00	0.00	0.00	0.00	0.00	0	0.00	0	0	0
Journal 3-Bot	0.00	0.00	0.00	0.00	0.00	0	0.00	0	0	0
Journal 4-Top	0.00	0.00	0.00	0.00	0.00	0	0.00	0	0	0
Journal 4-Bot	0.05	0.09	0.12	0.01	**0.09**	406	**1.30**	109	391	0

Coefficent of friction

Bearing joint positions **>>-> Friction error loads**

	rx m	ry m	Fcrush loads Fx m	Fy m	Tz N-m	Ffriction loads Fx N	Fy N	Tz N-m	Tz-Friction N-m	Fx-Total N	Fy-Total N	Tz-Total N-m
Journal 1-Top	**0.116**	**0.048**	0	0	0	0	0	0	0	0	0	0
Journal 1-Bot	0.116	**-0.041**	0	90	10	-233	33	-6	0	-233	123	5
Journal 2-Top	**0.007**	0.048	0	1	0	-340	121	17	0	-340	122	17
Journal 2-Bot	0.007	-0.041	0	0	0	0	0	0	0	0	0	0
Journal 3-Top	**-0.095**	0.048	0	10	-1	0	0	0	0	0	10	-1
Journal 3-Bot	-0.095	-0.041	0	0	0	0	0	0	0	0	0	0
Journal 4-Top	**-0.204**	0.048	0	-50	10	0	0	0	0	0	-50	10
Journal 4-Bot	-0.204	-0.041	0	0	0	109	391	-75	0	109	391	-75
									Σ:	**-464.1**	**596.2**	**-44.3**

Coupling stiffness

Kx	**234**	N/micron	**Ky**	**563**	N/micron	**Kθz**	**9.06**	N-m/microradian

Coupling centroid error motions

δx	**-1.983**	microns	**δy**	1.059	microns	**δθz**	-4.889	microradians

Journal error motions in sensitive direction

	rx microns	ry microns	δx(Σforces) microns	δy(Σforces) microns	δy(θz) micro-radians	Coupling hysteresis (friction/surface finish) minimum microns	mean microns	maximum microns	σ microns	value	δy-total microns	δy-max microns
Journal 1	116078	3200	-1.983	1.059	-0.567	**-0.050**	0.000	**0.050**	0.017	**0.00**	**0.492**	2.056
Journal 4	-203900	3200	-1.983	1.059	0.997	**-0.175**	0.000	**0.175**	0.058	**0.00**	**2.056**	

Precisely Positioning Pallets in Multi-Station Assembly Systems

R. Ryan Vallance*, Chris Morgan*, and Alexander H. Slocum†

* Mechanical Engineering, University of Kentucky, 277 Ralph G. Anderson Building, Lexington, KY 40506
Ph: 859-257-1279, Fax: 859-257-3304, vallance@engr.uky.edu

† Department of Mechanical Engineering, RM 3-445 77 Massachusetts Ave., Massachusetts Institute of
Technology, Cambridge, MA 02139, Ph: 617-253-0012, Fax: 617 258-6427, slocum@mit.edu

Abstract

In multi-station assembly systems, common for mass-customization manufacturing strategies, the product being assembled is held in a fixture attached to a pallet, and the pallet is conveyed between workstations. In high-precision assembly systems, variation in the position of the pallet is one of the largest sources of variation within the error budget, reducing quality and yields. Conventional approaches to locating pallets use pins and bushings, and a method for predicting their repeatability is presented. This paper also presents an exact constraint approach using a new split-groove kinematic coupling, which reduces variation in pallet location by an order of magnitude.

Keywords: kinematic couplings, split-groove coupling, pallets, flexible assembly systems, and assembly automation

1. Introduction

Nearly all products require that manufactured parts be assembled together into a final product. The assembly process is either conducted manually or automatically using assembly machines. The term "assembly automation", popularized around World War II, refers to the mechanized feeding, placement, and fastening of manufactured components into complete a product assembly. Since tooling and equipment is often dedicated to a particular product, automated assembly is generally reserved for mass-produced components, where the expense of custom tooling and equipment can be distributed over many units. During the 1970s and 1980s, much engineering and research effort concentrated on exchanging hard automation for flexible automation by incorporating re-programmable equipment such as robots and computer controlled machinery. Flexible automation prolonged the life of capital equipment, and consequently, automated assembly became economical for lower-volume production.

More recently, reduced time-to-market and shortened product life cycles provided further incentive for flexible automation using computer-controlled equipment. For these reasons, automated assembly machinery is now common for many products.

To achieve economical production, assembly tasks are frequently executed simultaneously on several product units using multiple machines. This generally requires that the machines or workstations be organized into an assembly system, and the products are then transported between machines or manual workstations. There are three principal categories of assembly systems: synchronous, non-synchronous, or continuous assembly systems. Synchronous systems cyclically index the products to individual machines simultaneously with fixed frequency. In non-synchronous systems, the assembly machines operate independently, and the index time depends upon the task time at each machine. Non-synchronous systems therefore employ buffers between the machines or stations to accommodate different task times at each station. In continuous systems, the product remains in constant motion, and the tasks are performed while the product travels.

All three types of assembly systems require that the product be transported through the system. In synchronous and non-synchronous systems, the product units are stationary at each assembly machine or workstation. Therefore the product unit must be statically positioned with respect to each assembly machine. A common approach is to hold each product unit in a fixture attached to an assembly pallet as illustrated in Fig 1a. Then the pallets can be moved synchronously or non-synchronously throughout the assembly system using a pallet transportation system. Multi-station assembly systems often use conveyor belts as illustrated in Fig 1b, and they generally operate non-synchronously.

This paper presents designs and techniques for precisely positioning assembly pallets at individual machines within assembly systems. Two separate approaches, pins-in-holes and exact constraint, are compared on the basis of stiffness and positional repeatability. It is shown that the repeatability of the exact constraint approach is much better than with the pins-in-holes approach. Although the static stiffness of the pins-in-holes approach can be greater, the stiffness of exact constraint is usually sufficient for most assembly tasks. Therefore, in precision assembly systems, the advantage of positional repeatability using exact constraint often outweighs additional improvement in static stiffness.

2. Positioning with Pins in Holes

A common technique for positioning one body with respect to another is to mate a set of pins (fixed in one body) inside a set of holes (in the second body). This pins-in-holes (PIH) technique is non-deterministic since contact between the two bodies may or may not occur. If contact occurs, it is difficult to anticipate the locations of contact, quantity, or sizes of any contact regions. This uncertainty arises from manufacturing errors in:

1) distances between the pins or holes,
2) diameters of the pins or holes,
3) straightness of the pins or holes,
4) parallelism of the pins or holes, and
5) cylindricity of the pins or holes.

Since PIH approaches are non-deterministic, their performance (repeatability and stiffness) is difficult to analyze or predict a priori, especially if more than two pins and two holes are used. The relation between design parameters (e.g. diameter of pins, clearance between pins and holes, distances between pins/holes) and performance cannot be expressed analytically for PIH configurations. As a result, it is often necessary to experimentally measure the repeatability and stiffness with actual manufacturing errors. For these reasons, we are limited to estimating planar repeatability for PIH designs employing only two pins and two holes (Section 2.2) and a qualitative discussion of static stiffness (Section 2.3).

2.1 Design of Pins-in-Holes Positioning Technique

A PIH positioning system may use any quantity of pins and holes, and as the quantity of pins and holes increases, the precision of the positioning improves and the stiffness increases. However, systems with more than two holes and two pins require tighter tolerances to prevent binding while mating the two objects. If the clearance between the pins and holes is insufficient to accommodate manufacturing errors then binding occurs, and large forces are necessary to elastically deform the pins and holes. Design precautions, which degrade the precision and stiffness, are necessary to reduce the chance of binding due to manufacturing errors.

The most obvious and common design precaution is to increase the clearance between the outer diameter (OD) of the pins and the inner diameter (ID) of the holes by manufacturing the holes slightly larger than the pins. This precaution accommodates many types of manufacturing errors, but dramatically reduces repeatability and stiffness of the PIH design. Another precaution reduces the sensitivity to manufacturing errors in the roundness, straightness, and parallelism by minimizing the length of engagement between the pin and hole. This is frequently accomplished using pins with large rounds or bullet noses that lead into shorter cylindrical regions, such as those shown in Fig 2. A third design precaution uses one round pin (Fig 2a) and one diamond shaped pin (Fig 2b) to reduce the sensitivity to a difference in the distance between pins and the distance between holes. The diamond pin is manufactured with two sharp corners and two rounded corners. The rounded corners have approximately the radius of an equivalent round pin. The distance between the two sharp corners should be less than the diameter of an equivalent round pin, and the distance between the two rounded corners is approximately equal to the diameter of an equivalent round pin. The diamond pin is oriented during assembly so that one of the sharp corners points directly toward the round pin. This insures that the rounded corners point perpendicular to a line connecting the centers of the two pins.

Fig 3 illustrates an industry standard pallet that uses the PIH positioning technique [1]. In this pallet system, two of the design precautions are applied. A round pin is used along with a diamond pin, and the tolerances are such that clearance is guaranteed between the pins and holes. The pallet is constructed of a steel or aluminum plate surrounded with a polyimide frame. Hard bushings with ground bores are pressed into the plate, and hard pins with ground surfaces are attached to the machine or assembly station (represented by plate in Fig 3).

The geometry, dimensions, and tolerance for the ground pins and bushings for pallet system illustrated in Fig 3 are summarized in Table 1. According to the tolerance specifications, the minimum pin diameter is 11.952 mm (0.4705 in), and the maximum bushing bore diameter is 12.0178 mm (0.4731 in). Hence, the worst-case diametric clearance is about 66 μm (0.0026 in). The manufacturer of the pallet system illustrated in Fig 3 specifies that their pallets are repeatable to within ±50 μm (±0.002 in) [1].

2.2 *Estimating Precision of Pins-in-Holes Positioning*

The precision, or 2D repeatability, of a particular PIH design is difficult to predict a priori since the pallet's position is non-deterministic and depends upon manufacturing errors. However, an estimate of the worst-case limit on repeatability can be obtained as an envelope that bounds possible translation and rotational errors. This section presents a technique for determining that envelope for PIH designs that use a bullet-nose round pin, a bullet-nose diamond pin, and two bushings. The clearance is assumed sufficient to prevent binding. The diameter and geometric form of the pins and holes is assumed perfect (roundness and straightness), and contact is assumed to occur only around the circumference of the pins. The clearance between a pin and hole, c, is defined in Eq (1) to be the difference between the nominal diameter of the pins, D_p, and nominal diameter of the holes, D_h.

$$c = D_h - D_p \tag{1}$$

Fig 4 illustrates the errors between two rigid bodies connected with a PIH design using two pins and two holes. The distance between the two pins is d_p, and the distance between the two holes is d_h. The clearance between the pins and holes is exaggerated for illustrative purpose. Since PIH is a planar positioning technique, we are only concerned with errors in three degrees of freedom: translation in the *x* direction, translation in the *y* direction, and a rotation angle. Two crosshatched circles represent the pins in the stationary object (machine base or workstation). The errors are measured in a reference coordinate system with origin, O, located at the center of Pin 1 with x-axis pointing towards the center of Pin 2.

The coupled body (pallet) is shown in two distinct orientations. The two orientations are the extreme cases of rotational error, limited when Hole 2 contacts Pin 2. In the first orientation (solid lines with crosshatching), Pin 2 contacts Hole 2 at Point A, and in the second orientation (dashed lines without crosshatching) Pin 2 contacts Hole 2 at Point B. Both orientations are illustrated with the same translation error, $\vec{\delta}$, that has components δ_x and δ_y in the *x* and *y* directions of the reference coordinate system located at the center of Pin 1.

The potential range of rotational error, θ, depends upon the direction and magnitude of the translation error, $\vec{\delta}$. For instance, a translation error solely in the x direction with magnitude equal to the clearance will not permit any rotational error, but a translation error solely in the y direction with magnitude equal to the clearance permits rotational error. Therefore, an expression for the range of permissible rotational error as a function of translation errors is needed to evaluate the potential repeatability errors of a PIH design.

The centers of Hole 2 in the two extreme orientations lie at the intersections of two theoretical circles, labeled as Circle A and Circle B in Fig 4. The center of Circle A is at the center of Hole 1 (Point C), and its radius is equal to the distance between the two holes, d_h. Circle A represents the locus of points traced by the center of Hole 2 when a rotation occurs about Point C. Points that lie on Circle A satisfy Eq (2).

$$(x-\delta_x)^2+(y-\delta_y)^2={d_h}^2 \tag{2}$$

The center of Circle B is at the center of Pin 2, and its radius equals the difference between the radii of the hole and pin. The radius of Circle B equals the maximum distance between the center of Pin 2 and Hole 2 that can ever occur. Points that lie on Circle B satisfy Eq (3), which is written in terms of the diametric clearance, c.

$$(x-d_p)^2+y^2=\frac{c^2}{4} \tag{3}$$

In the two extreme orientations, the center of Hole 2 could be located at either Point D or E. The coordinates of Points D and E in the reference coordinate system can be determined by solving Eqs (2) and (3) as a system of simultaneous non-linear equations. The coordinates of Point D and Point E are designated as (x_D, y_D) and (x_E, y_E), respectively, and can be readily calculated using iterative techniques. Once the coordinates points D and E are determined, the lengths of edges along triangle CDE can be calculated. The lengths of the triangles edges (l_{DE}, l_{CD}, and l_{CE}) are given by Eqs (4)-(6).

$$l_{DE}=\left[(x_E-x_D)^2+(y_E-y_D)^2\right]^{1/2} \tag{4}$$

$$l_{CD}=\left[(x_D-\delta_x)^2+(y_D-\delta_y)^2\right]^{1/2} \tag{5}$$

$$l_{CE}=\left[(x_E-\delta_x)^2+(y_E-\delta_y)^2\right]^{1/2} \tag{6}$$

The potential range of rotational error, θ, equals the angle between the edges CD and CE. Since the three edges' lengths are known, the angle θ can be calculated using the Law of Cosines as shown in Eq (7).

$$\theta=f(\delta_x,\delta_y)=\cos^{-1}\left\{\frac{{l_{CD}}^2+{l_{CE}}^2-{l_{DE}}^2}{2\,l_{CD}\,l_{CE}}\right\} \tag{7}$$

Although Eqs (2)-(7) yield a general solution, the analysis for most PIH systems, including pallet positioning, can be approximated with a simpler closed-form solution that does not require iterative methods. The approximate solution is derived with a few reasonable assumptions. Small clearances are assumed so that D_h and D_p are approximately equal, and the distances between the two pins and two holes are assumed to be equal (so that d_p equals d_h). The coordinates for Point D and Point E approximated with these assumptions is distinguished using ^ above the variables, $(\hat{x}_D, \hat{y}_D)$ and $(\hat{x}_E, \hat{y}_E)$. The approximate coordinates in the *x*-direction, $\hat{x}_D$ and $\hat{x}_E$, are equal; their value is simply the sum of the translation error in the x direction and the distance between the pins as given in Eq (8). The approximate y coordinates, $\hat{y}_D$ and $\hat{y}_E$, for the centers of Hole 2 in both orientations are given by Eq (9) and Eq (10), respectively.

$$\hat{x}_D \approx \hat{x}_E \approx \delta_x + d_p \tag{8}$$

$$\hat{y}_D \approx \left[\frac{c^2}{4} - \delta_x^{\ 2}\right]^{1/2} \tag{9}$$

$$\hat{y}_E \approx -\left[\frac{c^2}{4} - \delta_x^{\ 2}\right]^{1/2} \tag{10}$$

For most applications, the distance between the pins is much greater than the clearance ($d_p >> c$), and therefore l_{CD} and l_{CE} are approximately equal the distance between the pins, d_p. Substituting the approximate coordinates from Eq (8) - (10) and d_p for l_{CD} and l_{CE} into Eq (7) yields a closed-form estimate for the potential range of orientation error, $\hat{\theta}$. Note that the approximate range of angular error does not depend upon δ_y.

$$\hat{\theta} = f(\delta_x) = \cos^{-1}\left(1 - \frac{c^2}{2\,d_p^{\ 2}} + \frac{2\,\delta_x^{\ 2}}{d_p^{\ 2}}\right) \tag{11}$$

From Eq (11), it is evident that the maximum rotational error, $\hat{\theta}_{\max}$, occurs when the translation error is zero ($\delta_x = 0$). Accordingly, the approximate maximum rotation error is given in Eq (12). This result matches engineering intuition in that reducing the clearance and increasing the distance between pins reduces rotational errors.

$$\hat{\theta}_{\max} = \cos^{-1}\left[1 - \frac{c^2}{2\,d_p^{\ 2}}\right] \tag{12}$$

Finally, an envelope bounding the repeatability errors for a particular PIH design can be specified. Due to the circular perimeter of holes and pins, the translations in both the x and y directions are limited within a circle of radius $c/2$; hence the translation errors are bounded by $-c/2$ and $c/2$. The rotational errors are bounded within $-\hat{\theta}_{\max}/2$ and $\hat{\theta}_{\max}/2$.

A visual interpretation of these limits to repeatability errors is obtained by graphically plotting $\theta_{\max}$ or $\hat{\theta}_{\max}$ as a function of δ_x and δ_y. The translation errors in the *x* and *y* directions are plotted along the *x* and *y* axes, and the range of rotational error is plotted along the z-axis. Fig 5 shows a graph of the repeatability limits for the examplary PIH pallet system shown in Fig 3 with $d_p = 287.5$ mm and $c = 0.0661$ mm. The range of rotational errors shown in Fig 5 was determined using the approximate solution method. For this particular PIH pallet system, the maximum range of rotational error is calculated to be around 2.3×10^{-4} radians. This rotational error is amplified over the length of the pallet into a translation error of around 0.07 mm. For this analysis, the difference between the estimated solution and the solution obtained by solving the simultaneous equations is only -4.2×10^{-7} %, and thus the approximate solution is adequate.

2.3 Stiffness of Pins-in-Holes Positioning

All assembly pallets are subjected to disturbance forces that occur during assembly operations. At each workstation, these forces have particular magnitudes, act in particular directions, and are applied at particular positions on the pallet, fixture, or workpiece. Disturbance forces produce elastic deformation in the pallet, fixture, workpiece, and at the contact regions between the pallet and the workstation. The contact stiffness due to the pallet's positioning technique affects the amount of deflection and errors that result from disturbance forces. In precision assembly systems, the fixture and pallet are stiff to minimize errors due to elastic deformation. Hence elastic errors at the contact points are generally not negligible in the error budget and should be considered when evaluating a pallet positioning technique.

For PIH designs, the stiffness of the contact regions depends upon the clearances between the pins and holes, the size and quantity of any contact areas, amount of friction between the coupled bodies, and the degree of loading. Because of manufacturing variation in pallets, pins, and bushings, these parameters cannot be known deterministically, and therefore the static stiffness of a PIH design cannot be predicted a priori. Therefore, the relationship between PIH design parameters and static stiffness is discussed qualitatively.

Disturbance forces applied in the *z* direction (parallel to the axis of the pins) are typically transferred directly from the pallet to the workstation without transmitting much of the force through contact areas between the pins and holes. The contact areas in the *z* direction are often large flat surfaces on the bottom of the pallet and large flat surfaces on the workstations. The stiffness in the *z* direction depends, however, upon the geometry of the pallet and the elastic modulus of the materials. In the commercial pallet system, a polyimide frame contacts a metal plate in the workstation. With suitable construction and materials, substantial static stiffness in the *z* direction is obtainable, and reasonable estimates of stiffness in the *z* direction can be determined using elasticity models or finite element analyses (FEA)*. Fig 6 shows the results of an FE analysis of the commercial pallet subjected to a force of 1 N in the center of the pallet. The static deflection is about 1.52×10^{-7} m, providing static stiffness of about 6.58×10^{6} N/mm.

Typically, the pins are used only for positioning, and so clamping forces are often applied to achieve lateral stiffness. With strong clamping forces, the stiffness for a particular PIH design can be quite large. However, if the pins are not initially in contact with the holes, then sliding (translation and/or rotation) might occur until the pins contact the holes, and the range of possible sliding errors can be estimated using the model described in Section 2.2. If clamping forces are insufficient and sliding occurs, then disturbance forces applied to the pallet in the tangential direction are transmitted from the pallet to the workstation through conforming contact between the pins and holes. When contact exists between the pin and holes, the stiffness depends upon the size of the contact area between the pins and the holes. With tight clearances (slip-fits and/or press-fits) and large engagement lengths, the stiffness is typically sufficient for pallets. However, this greatly compromises the ease of placing the pallet on the workstation and separating the pallet from the workstation. Thus most PIH pallet systems typically maintain clearance between the pins and holes and rely on clamping for lateral stiffness.

3. Positioning with Exact Constraint Devices

An alternative approach for positioning pallets uses exact constraint devices between the pallets and workstations [2]. The term "exact constraint" refers to the fact that the pallet is neither over constrained nor under constrained [3]; sufficient constraints are applied to restrict exactly six degrees of freedom. Kinematic couplings are one form of exact constraint devices. Designers of instrumentation and optical systems have used kinematic couplings for many years [4,5,6,7,8], but their application in manufacturing processes and machines is more recent

---

* If the stiffness of the workstation is great compared to the stiffness of the pallet, then a reasonable FEA model can be obtained using zero-displacement boundary conditions on the pallet's bottom surface. If the stiffness of the workstation's structure is comparable or less stiff than the pallet, then the workstation structure should also be included in the FEA model.

[9,10]. In pallet positioning, we consider the two bodies to be the machine base and the pallet. The challenge is to provide static stiffness and prevent tipping of the pallet when subjected to a variety of disturbance forces.

Kinematic couplings connect two bodies through contact at six points, exactly enough for static equilibrium. Six independent contact points ensures that the coupled body (pallet) is statically determinant but not over-constrained. Kinematic couplings come in a few alternative configurations that differ according to the relative locations of the six contact points, the geometry of the contacting surfaces, their preload mechanism, and the contacting materials. The two most common configurations are the Kelvin coupling and the three-groove coupling [4]. The Kelvin coupling, illustrated in Fig 7a, establishes six contact points by mating three balls on the first body with the surfaces of a tetrahedron, a vee-groove, and a flat on the second body. The three-groove coupling, illustrated in Fig7b, establishes six contact points by mating three balls on the first body with the surfaces of three vee-grooves on the second body. The new split-groove coupling in Fig7c establishes six contact points by mating four balls with two vee-grooves and a split vee-groove in the second body. The split-groove coupling increases tipping resistance compared to other configurations and makes the design amenable for supporting rectangular plates as found in pallets.

Kinematic couplings gain two significant advantages by ensuring that the body is statically determinant. First, no elastic strain or deformation is induced in the coupled body due to forced congruence at additional contact points or surfaces. The second advantage is that a preferred relative position and orientation between the two bodies exists (due to minimizing potential energy). Unfortunately, since the contact between the bodies is limited to six points, the reactions at the contact points are distributed over very small areas; thus Hertzian stresses at the contact points are large when large disturbance forces are applied to the pallet (or in some cases the workstation). The elastic strain at the contact points that arises with the contact stress also limits the static stiffness between the coupled bodies. In addition, unless the preload is sufficiently high, loads applied to the pallet may cause the pallet to tip.

3.1 Design of Split-Groove Kinematic Couplings

Since many aspects of kinematic couplings can be analyzed, the design procedure enables a deterministic [11] approach. Several design and analysis aspects of kinematic couplings are described in precision engineering literature [12,13], so a comprehensive presentation of the methods is not necessary here. Instead, a synopsis of the procedure is presented along with appropriate references to supplementary literature. Fig 8 illustrates a procedure for designing kinematic couplings that consists of design and analysis phases. The first step in the design phase is to select a configuration for the kinematic coupling. Although the most common configurations are the Kelvin coupling and the three-groove coupling, the new split-groove coupling presented here is more suitable for integration with conveyor lines and rectangular pallets. In these applications, the area beneath the pallet needs to remain clear to not interfere with a conveying or indexing system.

The second design step is to select the topography of the contacting surfaces. The topography considers the geometric shape of the contacting surfaces and whether the pallet contains the vee-grooves or balls. A simple topography is the case of a spherical surface contacting a flat surface on the assembly workstation. This topography is easy to analyze and produce since precise balls are readily available for tooling applications and smooth flat surfaces are easily manufactured. Depending upon the application, other topographies such as those illustrated in Fig 9 may be employed. For instance, employing conforming geometry such as a ball in a canoe can dramatically reduce contact stresses and increase contact stiffness. VanDoren described this technique to locate machinery modules for semiconductor manufacturing equipment [14].

The third design step is to select appropriate materials for the contact points. The perfect material should have a high yield strength to withstand contact stresses, high hardness to minimize wear, and high toughness to prevent brittle fractures on the surface. For achieving greatest repeatability, the contacting materials should also have low friction (lubricant may be used in some cases). Schouten et al. [15] showed that hysteresis due to friction can be dramatically reduced by cutting flexures into the grooves to give them tangential compliance while maintaining high stiffness in direction of contact. Appropriate materials therefore include ceramics like tungsten carbide, silicon nitride, alumina, as well as hardened tool or stainless steels.

The final step is to design a method for preloading the pallet to the assembly workstation. Preload refers to a bias force that ensures contact between the pallet and the workstation regardless of disturbance forces. As described by Slocum [16], preload is essential in achieving precision, and two fundamental means are employed in mechanical systems: opposed geometry and applied external forces. Since opposed geometry (as used in recirculating ball bearings) requires the manufacture of extra high precision surfaces, applying external forces is often more economical. One method for implementing opposed-force preloading in pallet systems is to incorporate permanent magnets in the pallet and/or workstation as applied in metrology equipment [17].

3.2 Analysis of Pallets with Split-Groove Kinematic Couplings

The analysis phase illustrated in Fig 8 consists of six steps. First, a model of the kinematic coupling's geometry and dimensions is constructed using position vectors that locate the contact points. All applied forces or moments should be represented as vectors, and the application points of the forces should be specified with corresponding position vectors. The third step is to calculate the reaction forces at the six contact points by solving the simultaneous equations derived from static equilibrium. The directions of the reaction forces are known a priori since they are normal to the contacting surfaces. The sign of the reaction forces indicates whether the coupling remains in static equilibrium under the applied loads; if it is not, then both the geometry of the configuration and alternative configurations should be reconsidered.

If the coupling remains in static equilibrium for all possible assembly forces or moments, then the next step is to calculate the stress, strain, and elastic deformation produced at the contact points by the reaction forces. The final step is to determine the errors at the locations of the assembly operations that result from the translation or rotation of the pallet due to the elastic deformation at the contact points. This step is essential since small rotations of the pallet produce translation errors that are amplified by the distance to the assembly operation.

The geometry of a split-groove kinematic coupling is described with position vectors that are based in a Cartesian coordinate system located at the coupling centroid within the plane of the balls' centers. Six position vectors, $\vec{P}_{C_i}$, locate the contact points, and four position vectors, $\vec{P}_{B_j}$, locate the balls' centers. Six unit vectors, $\vec{n}_i$, act through the contact points, normal to the contacting surfaces. The six normal vectors point in the direction from the groove surfaces and towards the balls' centers. These vectors are all illustrated in Fig 10, and can be expressed parametrically as functions of the designer's preferred dimensions, e.g. coupling length, width, coupling angle, and ball diameter.

Following the approach presented by Schmiechen and Slocum [13], the equations of static equilibrium are written in matrix form as shown in Eq (13). The system matrix, $[K]$, relates the applied loads, $\vec{L}_A$, to the reaction forces at the contact points, $\vec{R}_C$. $[K]$ is calculated using the position and normal vectors as shown in Eq (14). $\vec{L}_A$ is a 6x1 vector of forces and moments that is calculated as the sum of loads due to weight, $\vec{L}_W$, preload forces, $\vec{L}_P$, and disturbance forces $\vec{L}_D$ as shown in Eq (15). Any forces or moments that arise due to assembly operations are treated as disturbance loads. The six reaction forces at the contact points are calculated as the components of the 6x1 vector $\vec{R}_C$.

$$\vec{R}_C = -[K]^{-1}\vec{L}_A \tag{13}$$

$$[K] = \begin{bmatrix} \vec{n}_1 & \vec{n}_2 & \vec{n}_3 & \vec{n}_4 & \vec{n}_5 & \vec{n}_6 \\ \vec{P}_{C_1}\times\vec{n}_1 & \vec{P}_{C_2}\times\vec{n}_2 & \vec{P}_{C_3}\times\vec{n}_3 & \vec{P}_{C_4}\times\vec{n}_4 & \vec{P}_{C_5}\times\vec{n}_5 & \vec{P}_{C_6}\times\vec{n}_6 \end{bmatrix}_{6x6} \tag{14}$$

$$\vec{L}_{A6x1} = \vec{L}_W + \vec{L}_P + \vec{L}_D = \begin{bmatrix} \left(\vec{F}_{W_i}\right)_{3x1} \\ \left(\vec{P}_W \times \vec{F}_W\right)_{3x1} \end{bmatrix} + \sum_{i=1}^{l} \begin{bmatrix} \left(\vec{F}_{P_i}\right)_{3x1} \\ \left(\vec{P}_{P_i} \times \vec{F}_{P_i}\right)_{3x1} \end{bmatrix} + \sum_{j=1}^{m} \begin{bmatrix} \left(\vec{F}_{D_i}\right)_{3x1} \\ \left(\vec{P}_{D_i} \times \vec{F}_{D_i}\right)_{3x1} \end{bmatrix} \tag{15}$$

After determining the reaction forces in $\vec{R}_C$, the distribution of stress near the contact points should be evaluated, and material failure should be considered. This is generally done assuming Hertzian contact [18,19], and Slocum [20] provides a convenient form of the equations. The magnitude of the stress, strain, and deformation at the contact points depends upon the topography at the contact points (Fig 9) and the contacting materials. Ductile materials are likely to fail due to shear stress beneath the contacting surface, and brittle materials are likely to fail due to tensile stress near the edge of the contact area. If a comparison of the maximum stresses with the material strength indicates failure, then the design can be improved by changing dimensions, materials, or contact topography.

In the three configurations of kinematic couplings illustrated in Fig 7, a sphere contacts a flat surface. For this simple case, the contacting surfaces are axi-symmetric about the surface normal vector, and so the contact area at the ith contact point is circular. The radius of the circular contact area, a_i, is given in Eq (15) as a function of the reaction force at the contact point, R_{C_i}, the diameter of the contacting sphere, D_{S_i}, and the equivalent modulus of elasticity, E_e. Eq (17) gives E_e in terms of the moduli of elasticity and Poisson's ratios for the sphere and flat surfaces.

$$a_i = \left(\frac{3R_{C_i}D_{S_i}}{8E_e}\right)^{1/3} \quad \text{for } i = 1 \ldots 6 \tag{16}$$

$$E_e = \frac{1}{\left(\dfrac{1-\nu_S{}^2}{E_S} + \dfrac{1-\nu_f{}^2}{E_F}\right)} \tag{17}$$

For the case of a sphere contacting a flat surface, Johnson [19] gives simple expressions for the maximum shear stress and maximum tensile stress. Eq (18) gives the the maximum shear stress at the ith contact point, $\tau_{\max_i}$, which should be considered for ductile material failure. The maximum tensile stress at the ith contact point, $\sigma_{\max_i}$, should be considered for failure of brittle materials, and it depends upon Poisson's ratio for the contacting material and is given in Eq (19).

$$\tau_{\max_i} \approx \frac{0.47 R_{C_i}}{\pi a_i^{\,2}} \tag{18}$$

$$\sigma_{\max_i} \approx \frac{(1-2\upsilon)R_{C_i}}{2\pi a_i^{\,2}}. \tag{19}$$

The compressive reaction forces at the contact points produce strain in the contacting bodies so that the ith sphere and flat approach each other by distance, δ_{C_i}, which can be calculated with Eq (20). The deformations at all six contact points are grouped into a 6x1 vector, $\vec{\delta}_C$.

$$\delta_{C_i} = \left(\frac{18 R_{C_i}^{\,2}}{16 D_{S_i} E_e^{\,2}}\right)^{1/3} \tag{20}$$

Due to the deformation at the six contact points, a rigid pallet translates and rotates with respect to a coordinate system in the machine base. Since this motion is undesirable, so it is referred to as the pallet's error motion. The rigid body translations and rotations are components of a vector, $\vec{\delta}_E$, as shown in Eq (21), and they are measured in the Cartesian coordinates at the coupling's centroid (Fig 10). As shown by Schmiechen and Slocum [13], $\vec{\delta}_E$ can be calculated using the transpose of the inverted system matrix and the contact deformation vector as shown in Eq (22).

$$\vec{\delta}_E = \left[\delta^x \quad \delta^y \quad \delta^z \quad \varepsilon^x \quad \varepsilon^y \quad \varepsilon^z\right]^T \tag{21}$$

$$\vec{\delta}_E = \left([K]^{-1}\right)^T \vec{\delta}_C \tag{22}$$

Homogenous transformation matrices (HTMs) provide an effective method to represent translations and rotations between successive coordinate systems, and an introduction to this approach is available from Craig [21]. The translations $\left(\delta^x, \delta^y, \delta^z\right)$ and rotations $\left(\varepsilon^x, \varepsilon^y, \varepsilon^z\right)$ associated with the pallet's error motion are therefore collected in the HTM given in Eq (23), assuming small rotation angles. $[T_E]$ represents the transformation between coordinate systems at the coupling centroid in the machine base and pallet that differ by the error motion. The position of a point on the pallet or fixture after the error motion is then determined by premultiplying a position vector that locates the point with $[T_E]$.

$$[T_E]=\begin{bmatrix} 1 & -\varepsilon^z & \varepsilon^y & \delta^x \\ \varepsilon^z & 1 & -\varepsilon^x & \delta^y \\ -\varepsilon^y & \varepsilon^x & 1 & \delta^z \\ 0 & 0 & 0 & 1 \end{bmatrix} \tag{23}$$

Small rotations that occur at the coupling centroid produce displacement errors at other positions on the pallet or fixture. To assess this effect on assembly operations, it is necessary to calculate the position error, $\vec{P}_E$, at each point on the fixture or pallet where assembly operations are conducted. Each operating point should be located with a position vector, $\vec{P}_o$, measured in the coupling's centroid coordinate system. The position error, expressed in Eq (24), is then the difference between the position of the operating point before and after the error motion.

$$\vec{P}_E=[T_E]\vec{P}_o-\vec{P}_o \tag{24}$$

3.3 Conditions for Tipping due to Disturbance Loads

It is likely that assembly operations will subject a pallet to a range of disturbance forces, and so the combination of the pallet weight and preload forces should be sufficient to prevent tipping or sliding of a kinematically coupled pallet. This condition is satisfied when contact exists at the six contact points as indicated when the reaction forces at the contact points are all positive. This condition is expressed in Eq (25), where R_{C_i} is the reaction at the ith contact point and a component of the reaction force vector, $\vec{R}_C$.

$$R_{C_i}>0 \qquad \text{for } i=1...6 \tag{25}$$

The condition may be rewritten in terms of the applied loads and row vectors from the inverted system matrix [2]. In Eq (26), the condition is expressed as the dot product between the ith row vector of the inverted system matrix, $\vec{K}_{R_i}^{-1}$, and the disturbance load, $\vec{L}_D$, should be less than the dot product between $\vec{K}_{R_i}^{-1}$ and the sum of the loads due to weight and preload. As demonstrated in the following section, this condition can be used to graphically visualize a bounded region, limited by the six values on the right hand side of Eq (26), in which the kinematic coupling should not tip due to in sufficient preloading.

$$\vec{K}_{R_i\,6x1}^{-1} \cdot \vec{L}_{D6x1} < \vec{K}_{R_i\,6x1}^{-1} \cdot \left(\begin{bmatrix} \left(\vec{F}_W\right)_{3x1} \\ \left(\vec{P}_W \times \vec{F}_W\right)_{3x1} \end{bmatrix} + \sum_{i=1}^{l} \begin{bmatrix} \left(\vec{F}_{P_i}\right)_{3x1} \\ \left(\vec{P}_{P_i} \times \vec{F}_{P_i}\right)_{3x1} \end{bmatrix} \right) \quad \text{for } i = 1 \ldots 6 \tag{26}$$

3.4 Pallets Employing Split-Groove Kinematic Couplings

The procedures described in Sections 3.1 through 3.3 were applied in the design of a split-groove kinematic coupling for improving the commercial pallet system [2]. The pins and bushings within the commercial pallet were not used; instead, a split-groove kinematic coupling was incorporated into a fixture that fastened onto the commercial pallet. Hard stainless steel (440C) tooling balls were fastened to the fixture plate, and hard stainless steel (440C) vee-grooves were incorporated into the assembly workstation. The split-groove configuration made it possible for the vee-grooves to straddle the width of the pallets' conveyor system and eliminated the need for a vee-groove in the center of the conveyor system. The pallet was preloaded into the vee- grooves using a set of 12 permanent magnets, 6 in the fixture plate and 6 in the machine base. The magnetic preload was sufficient to ensure that the pallet remained in equilibrium for a range of disturbance forces, but the preload was not excessive for manually removing the pallet off of the workstation. Fig 11 shows photographs of the split-groove kinematic pallet system. The vee-grooves and the permanent magnets in the workstation base can be seen in Fig 11a. Fig 11b shows the bottom of the pallet plate that contains four balls and six preload magnets. Fig11c shows the fixture and pallet kinematically coupled to the workstation base.

The dimensions of the split-groove kinematic coupling are listed in Table 2. Using these dimensions, the position vectors to the contact points and normal vectors illustrated in Fig 10 are determined, and the components of the vectors are summarized in Table 3 and Table 4. The system matrix, [*K*], shown in Eq (27) is calculated by substituting the components of the position vectors and normal vectors into Eq (14). Knowing the system matrix and any applied forces enables the determination of the reaction forces at the contact points with Eq (13). The critical contact stress at each contact point is determined using the Hertzian relations for a sphere contacting a flat surface, Eqs (16)-(19), and the errors are evaluated using Eqs (20)-(24). These calculations are not presented here, since examples are available in prior literature by Schmeichen and Slocum [13] and Johnson [19].

$$[K] = \begin{bmatrix} -0.578 & 0.578 & 0.578 & -0.578 & 0.000 & 0.000 \\ -0.408 & 0.408 & -0.408 & 0.408 & 0.707 & -0.707 \\ 0.707 & 0.707 & 0.707 & 0.707 & 0.707 & 0.707 \\ 71.842 & 71.842 & -71.842 & -71.842 & -69.597 & 69.597 \\ 50.773 & 50.773 & 50.773 & 50.773 & -152.103 & -152.103 \\ 87.973 & -87.973 & 87.973 & -87.973 & 152.103 & -152.103 \end{bmatrix} \tag{27}$$

Since the pallet is subject to a range of disturbance forces, it is necessary to ensure that the pallet will not tip using the condition presented in Section 3.3. Within the assembly workstation, the forces applied to the kinematically coupled pallet include the pallet's weight, six preload forces, and disturbance forces that occur during the assembly operations. The weight of the pallet is approximately 64.7 N, and the preload is the result of six pairs of neodemium permanent magnets that each generates a force of about 22.3 N. During assembly operations, an insertion force of about 135 N presses downward on the pallet. The insertion forces are applied along a line that is parallel to the x-axis between x = -96.84 mm and x = 225.3 mm; the y-coordinate and z-coordinate are –44.37 mm and 89.10 mm, respectively. A summary of the force components and the position vectors that locate the application points of the forces are listed in Table 5.

The six conditional functions given in Eq (28) were determined from Eq (26) and are associated with each contact point. Evaluating the right-side of Eq (26) yields a constant value, but the left-side of the inequality is a function of the component of the insertion force in the z direction, F_D^z, which may vary between 0 N and –135 N, and the *x*-coordinate where the insertion force is applied, P_D^x, which may vary between –96.84 mm and 225.3 mm. In this particular case, the conditional functions for contact points 1 and 2 are identical, the functions for points 3 and 4 are identical, and the functions for points 5 and 6 are identical.

$$\begin{gathered}
0.265F_D^z - 44.37\cdot(0.0035)F_D^z - 0.0012(P_D^x F_D^z) < 32.8 \\
0.265F_D^z - 44.37\cdot(0.0035)F_D^z - 0.0012(P_D^x F_D^z) < 32.8 \\
0.265F_D^z + 44.37\cdot(0.0035)F_D^z - 0.0012(P_D^x F_D^z) < 36.8 \\
0.265F_D^z + 44.37\cdot(0.0035)F_D^z - 0.0012(P_D^x F_D^z) < 36.8 \\
0.177F_D^z + 0.0025(P_D^x F_D^z) < 70.5
\end{gathered} \tag{28}$$

The values on the left side of the inequalities are plotted as contours in Fig 12a, b, and c. A bold contour indicates the boundary associated with the constants given on the right side of Eq (28). In the regions where values in the contour plots are less than the constant, the corresponding ball remains in contact with the flat surface. Fig12d shows the intersection of the boundaries for each contact point and the boundaries of the disturbance region. Since the equilibrium boundaries are outside the disturbance region, the pallet remains in equilibrium without tipping.

3.5 Precision of Kinematically Coupled Pallets

Kinematic couplings are known for their ability to precisely position one object with respect to another with extreme repeatability [15,24]. The principal reason for any non-repeatable behavior is the interaction between friction and structural compliance. Although analytical methods for relating design parameters to repeatability are not thoroughly developed, Hale suggested the relation given in Eq (29) as an estimate of repeatability [22]. Hale derived the estimate as if the coupling's compliance in all directions is equal to a single Hertzian contact carrying a load P and having a relative radius, R, and elastic modulus, E [23].

$$\rho \equiv \frac{f}{k} \approx \mu \left[\frac{2}{3R}\right]^{1/3} \left[\frac{P}{E}\right]^{2/3} \tag{29}$$

Since friction forces are uncertain and inconsistent, analytical techniques for assessing repeatability should be treated only as estimates. For this reason, accurate assessments of a kinematic coupling's repeatability should be determined experimentally. For instance, Slocum experimentally measured the repeatability of a three-groove coupling (356 mm diameter) and found that its axial and radial repeatability were on the order of 0.30 μm [24]. Schouten, Rosielle and Schellekens measured the repeatability of a kinematic coupling that incorporated flexures for tangential compliance at the contact points and found that the hysteresis was reduced by a factor of 10x to less than 0.1 μm [15].

The repeatability of the split-groove kinematic pallet shown in Fig 11 was assessed experimentally. The experiments were conducted on the apparatus shown in Fig 13, which duplicated the geometry of the machine base in the assembly workstation, including the vee-grooves, the split vee-groove, and the preload magnets. The pallet was lifted and dropped onto the grooves by a pneumatically actuated lift-plate. The lift-plate was guided by die set bushings, and it separated from the pallet at the bottom of travel to prevent over constraining the pallet's position. Capacitive displacement sensors were mounted around the perimeter of the pallet to measure the variation in the position of the pallet. Each sensor provided an analog signal (±10 V) proportional to the change in the distance between the face of the sensor and a steel target attached to the pallet (±50 μm). A 16-bit data acquisition system measured signals between ±5 V, providing a resolution around 0.76 nm/bit.

In factory-like environmental conditions, the split-groove kinematic pallet was lifted and dropped thousands of times over two days, and the gap distance was measured each time. Fig 14 shows a plot of the four sensors' displacement measurements in microns. The relative expansion and contraction of the pallet and fixture due to ambient temperature cycles produced cyclic fluctuations with a period of about 24 hours and maximum amplitude of about 10 μm in Sensor 1. The pneumatic system's air pressure produced additional periodic fluctuations with a period of approximately 2 hours. Even with the periodic fluctuations associated with the thermal and pneumatic cycles, the pallet was repeatable to within ±5 μm. This represents a 10X improvement over the conventional pallet that employed pins-in-holes, which is only repeatable to about ±50 μm.

4. Conclusion

Mass customization strategies are generating renewed interested in flexible manufacturing and assembly systems, even in products requiring high precision. To reduce the amount of manufacturing variation, it is necessary to consider the precision of alternative techniques for locating pallets at workstations. The conventional approach uses pins-in-holes, but the precision of this technique is often limited by the clearances between locating bushings and pins. A method for estimating the amount of expected variation in the position and orientation of a pallet that uses the pins-in-holes technique was presented. Kinematic couplings provide an alternative technique, which exactly constrains the location and orientation of the pallet. The procedure and analyses used in designing kinematically couplings is presented and demonstrated in designing a new split-groove kinematic coupling for assembly pallets, which gives the appearance of four-point support thus enhancing pallet stability. Experimental measurements of the kinematically coupled pallet demonstrated an order of magnitude reduction in the variability of the pallet's location compared to the conventional pins-in-holes technique. Therefore, split-groove kinematic couplings provide great advantage for achieving precise locations of pallets in multi-station assembly systems.

Acknowledgements

This work was supported by Teradyne Connection Systems and a grant from the Defense Logistics Agency AQP.

Nomenclature

a_i = Radius of contact area at contact point i

c = Clearance between pin and hole

D_p = Diameter of pins

d_p = Distance between pins

D_h = Diameter of holes
D_{S_i} = Diameter of sphere at contact point i
d_h = Distance between holes
E_e = Equivalent modulus of elasticity
E_f = Modulus of elasticity for flat surface
E_s = Modulus of elasticity for spherical surface
$[K]$ = Kinematic coupling's system matrix
$\vec{L}_A$ = Vector (6x1) of applied forces and moments
$\vec{L}_D$ = Vector (6x1) of disturbance forces and moments
$\vec{L}_P$ = Vector (6x1) of preload forces and moments
$\vec{L}_w$ = Vector (6x1) of weight forces and moments
l_{CD} = Length of line CD
l_{CE} = Length of line CE
l_{DE} = Length of line DE
$\vec{n}_i$ = Unit normal vector at contact point i
$\vec{P}_{B_j}$ = Position vector locating ball j
$\vec{P}_{C_i}$ = Position vector locating contact point i
$\vec{P}_E$ = Position vector locating an operating point after error motion
$\vec{P}_o$ = Position vector locating an operating point before error motion
$\vec{R}_C$ = Vector (6x1) of contact reaction forces
$[T_E]$ = Homogenous transformation matrix representing error motion
x = Coordinate of a point in the x direction
x_D = Coordinate of point D in the x direction
$\hat{x}_D$ = Approximate coordinate of point D in x direction
x_E = Coordinate of point E in x direction
$\hat{x}_E$ = Approximate coordinate of point E in x direction
y = Coordinate of a point in the y direction
y_D = Coordinate of point D in the y direction
$\hat{y}_D$ = Approximate coordinate of point D in y direction
y_E = Coordinate of point E in y direction
$\hat{y}_E$ = Approximate coordinate of point E in y direction
$\vec{\delta}$ = Translation error
$\vec{\delta}_c$ = Vector (6x1) of elastic deformation at contact points
δ_{c_i} = Elastic deformation at contact point i
$\vec{\delta}_E$ = Vector (6x1) of error motion translations and rotations
δ_x = Component of translation error in the x direction
δ_y = Component of translation error in the y direction
ρ = Estimate of repeatability

$\sigma_{\max_i}$ = Maximum tensile stress at contact point *i*

$\tau_{\max_i}$ = Maximum shear stress at contact point *i*

θ = Range of rotational error

$\theta_{\max}$ = Maximum range of rotational error

ν_f = Poisson's ratio for flat surface

ν_s = Poisson's ratio for spherical surface

References

[1] Bosch catalog for TS-2 conveyor system. Bosch Automation Products. 816 E. Third St., Buchanan, MI. 49107. Publication No. 8981500127.

[2] Vallance, R.R. *Precision Connector Assembly Automation.* Ph.D. Dissertation. Massachusetts Institute of Technology. 1999.

[3] Blanding, D.L. *Exact Constraint: Machine Design Using Kinematic Principles.* ASME Press. New York. 1999.

[4] Evans, C. *Precision Engineering: an Evolutionary View.* Cranfield Press. Bedford, UK. 1989.

[5] Jones, R.V. "Anti-Distortion Mountings for Instruments and Apparatus". *Journal of Scientific Instruments.* V. 38. 1961. p. 408-409.

[6] Whipple, R.S. "The Design and Construction of Scientific Instruments". *Transactions of the Optical Society.* V. 22. 1920-1921. p. 3-52.

[7] Brooks, L.S. "Adjustable Instrument Mount". *Journal Optical Society of America.* V. 44. 1954. p. 107-109.

[8] Hog, E. "A Kinematic Mounting". *Astronomics and Astrophysics.* V. 41. 1975. p. 107-109.

[9] Battles, A.E., Linder, B.M., Chang,K.W., and A.H. Slocum. "The Design of a Precision Bilaminar Resonating Transducer Assembly Tool". *Precision Engineering.* V. 15, No. 4. Oct 1993. p. 248-257.

[10] Culpepper, M.L. and A.H. Slocum. "Quasi-Kinematic Couplings: A Low-Cost Method for Precision Coupling of Product Components and the Like in Manufacturing Processes". *Proceedings of the 1999 Annual Meeting of the American Society for Precision Engineering.* Monteray, CA. November, 1999.

[11] Donaldson, R. "The Deterministic Approach to Machining Accuracy". *Proceedings of the SME Fabrication Technolology Symposium.* Golden, CO. November, 1972. (UCRL Preprint 74243).

[12] Slocum, A.H. "Design of Three-Groove Kinematic Couplings". *Precision Engineering.* V. 14, No. 2. April 1992. p. 67-76.

[13] Schmiechen, P. and A.H. Slocum. "Analysis of Kinematic Systems: a Generalized Approach". *Precision Engineering*. V. 19, No. 1. July 1996. p. 11-18.

[14] Van Doren, M. J. *Precision Machine Design for the Semiconductor Equipment Manufacturing Industry.* Doctoral Thesis. Massachusetts Institute of Technology. Cambridge, MA, USA. May, 1995.

[15] Schouten, Rosielle, and Schellekens, "Design of a Kinematic Coupling for Precision Applications", *Precision Engineering* Vol. 20, P. 46-52, 1997.

[16] Slocum, A.H. "Design of New Precision Machine Elements". *Initiatives of Precision Engineering at the Beginning of a Millennium.* 10th International Conference on Precision Engineering (ICPE). July 18-20, 2001. p.18-24.

[17] Olasz, J.S. and W.C. MacIndoe. "Surface Finish, Displacement, and Contour Scanner". U.S. Patent and Trademark Office. Patent #4,574,625. March 11, 1986.

[18] Hertz, H. "On the Contact of Elastic Solids". *Miscellaneous Papers by H. Hertz.* Eds. Jones and Schott. London. Macmillan. 1896.

[19] Johnson, K.L. *Contact Mechanics.* Cambridge University Press. Cambridge, UK. 1985.

[20] Slocum, A.H. *Precision Machine Design.* Society of Manufacturing Engineers. 1992.

[21] Craig, J. J. *Introduction to Robotics, Mechanics and Control.* Addison-Wesley. New York. 1989.

[22] Hale, L.C. "Friction-based Design of a Kinematic Coupling for Precision Applications". *Proceedings of the American Society for Precision Engineering Annual Conference.* 1998. p. 45-48.

[23] Hale, L.C. and A.H. Slocum. "Optimal Design Techniques for Kinematic Couplings". *Precision Engineering.* Vol. 25, No. 2. April 2001. p.114-127.

[24] Slocum, A. "Kinematic Couplings for Precision Fixturing – Part 1: Formulation of Design Parameters". *Precision Engineering.* Vol. 10, No. 2. April 1988. p. 85-91.

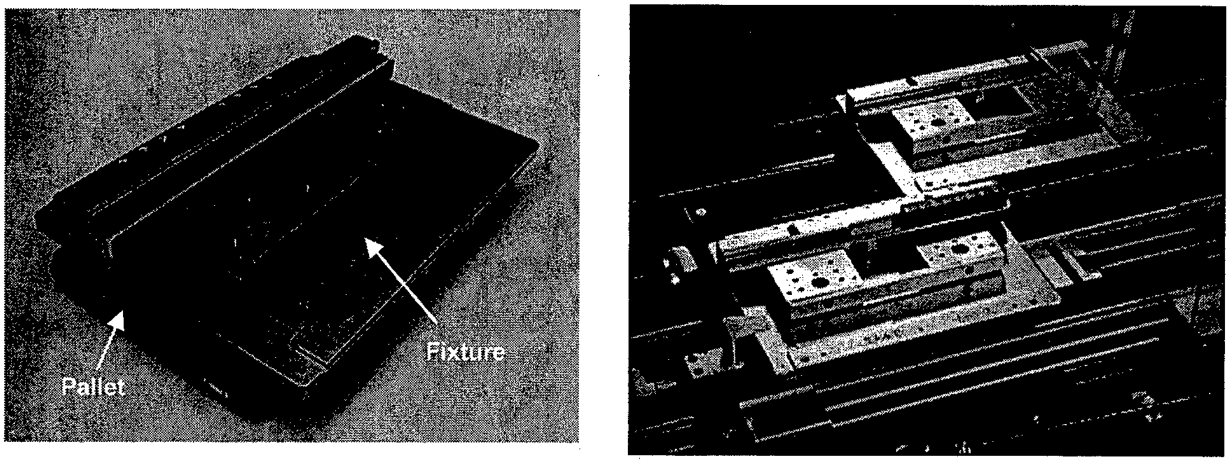

(a) (b)

Fig. 1 (a) Pallet and Fixture for Holding Electrical Connector During Assembly Operations (b) Flexible Assembly System with Conveyors for Non-synchronously Transporting Pallets

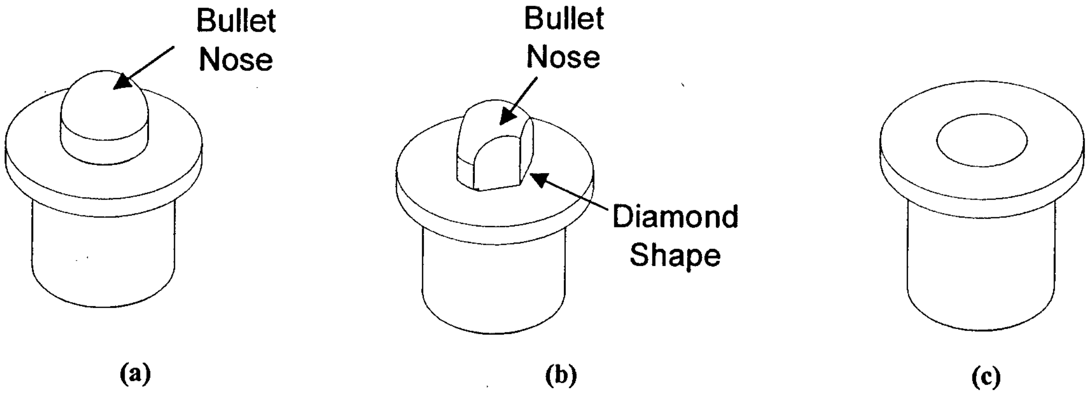
Bullet Nose
Bullet Nose
Diamond Shape
(a)
(b)
(c)

Fig. 2 Commercially Available Positioning Pins and Bushings (a) Round Pin with Bullet Nose, (b) Diamond Pin with Bullet Nose, and (c) Bushing

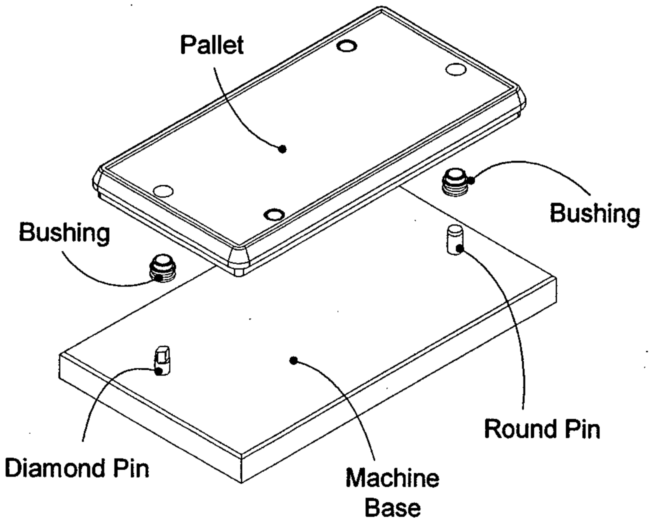
Pallet
Bushing
Bushing
Round Pin
Diamond Pin
Machine Base

Fig. 3 **Position Method in Commercial Pallets Using Pins-In-Holes Approach (Distance Between Pins Equals 287.5 mm (11.321 in))**

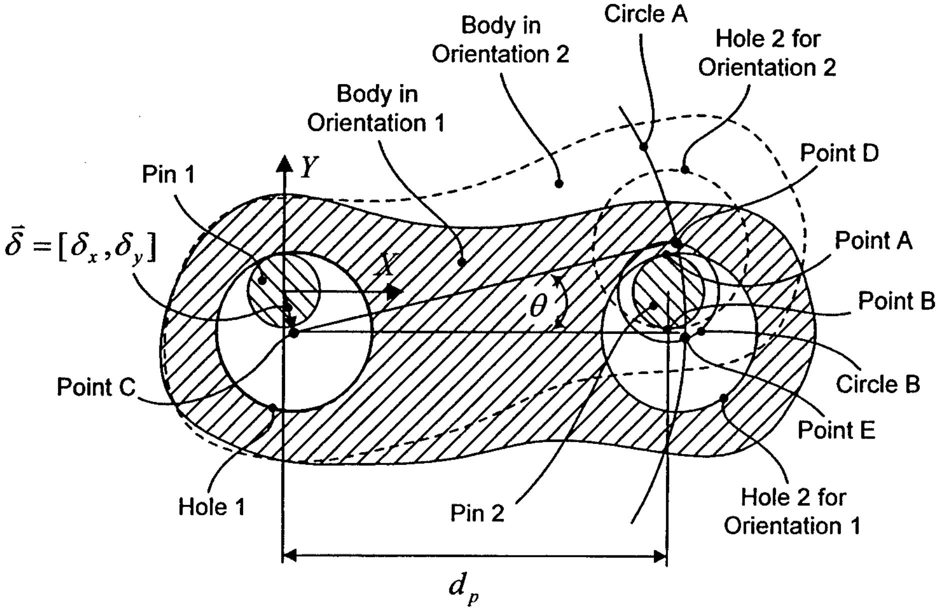
Body in Orientation 2
Circle A
Hole 2 for Orientation 2
Body in Orientation 1
Point D
Pin 1
Y
$\vec{\delta} = [\delta_x, \delta_y]$
X
Point A
θ
Point B
Point C
Circle B
Point E
Hole 1
Pin 2
Hole 2 for Orientation 1
d_p

Fig. 4 Errors in Pin-in-Hole Positioning Technique

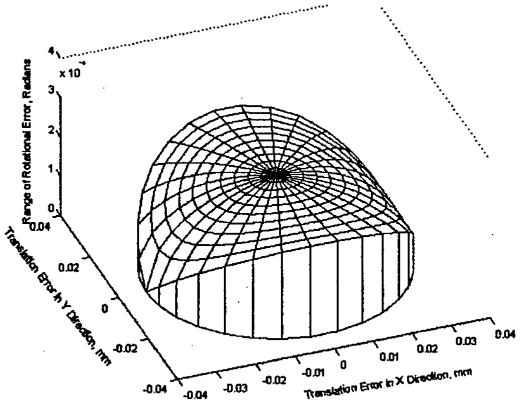

Fig. 5 Limits on Planar Repeatability Errors in Pallet System Using Pins-In-Holes Positioning

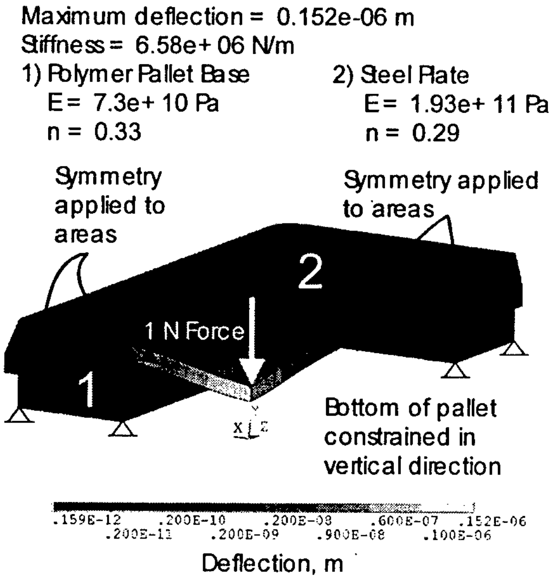
Maximum deflection = 0.152e-06 m
Stiffness = 6.58e+06 N/m
1) Polymer Pallet Base
E= 7.3e+10 Pa
n = 0.33
2) Steel Plate
E= 1.93e+11 Pa
n = 0.29
Symmetry applied to areas
Symmetry applied to areas
2
1 N Force
1
Y
X
Z
Bottom of pallet constrained in vertical direction
.159E-12
.200E-11
.200E-10
.200E-09
.200E-08
.900E-08
.600E-07
.100E-06
.152E-06
Deflection, m

Fig. 6 **Static Stiffness of Common Commercial Pallet Using Finite Element Analysis**

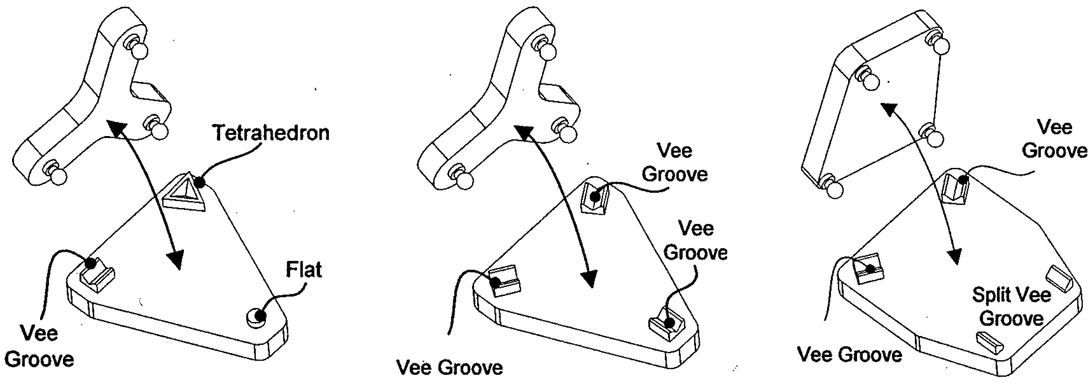
Tetrahedron
Flat
Vee Groove
Vee Groove
Vee Groove
Vee Groove
Vee Groove
Split Vee Groove
Vee Groove

(a) (b) (c)

Fig. 7 Configurations of Kinematic Couplings (a) Kelvin Coupling, (b) Three-groove Coupling, and (c) the New Split-groove Coupling

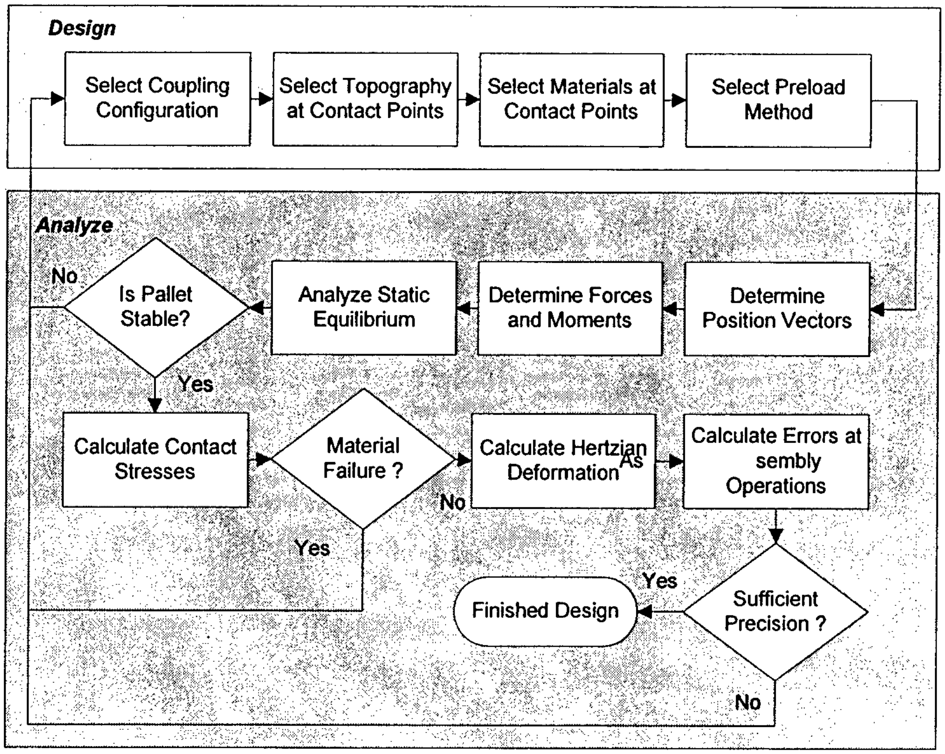
Design
Select Coupling Configuration
Select Topography at Contact Points
Select Materials at Contact Points
Select Preload Method
Analyze
No
Is Pallet Stable?
Analyze Static Equilibrium
Determine Forces and Moments
Determine Position Vectors
Yes
Calculate Contact Stresses
Material Failure ?
Calculate Hertzian Deformation
Calculate Errors at Assembly Operations
No
Yes
Yes
Finished Design
Sufficient Precision ?
No

Fig. 8 **Procedure for Designing Kinematic Couplings for Pallet Systems**

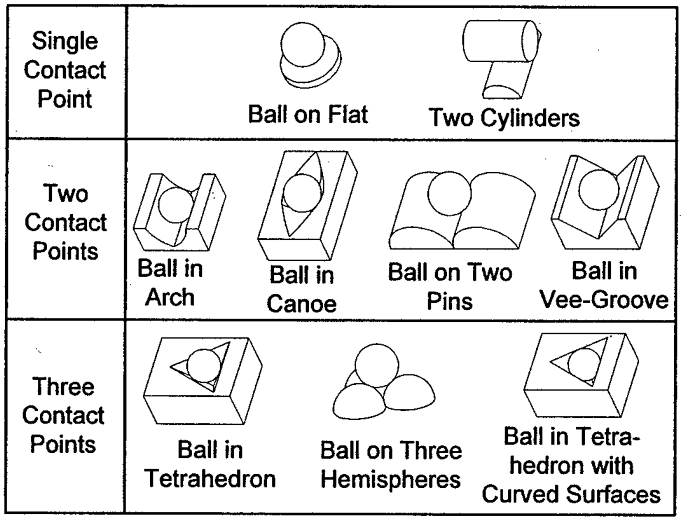
Single Contact Point
Ball on Flat
Two Cylinders
Two Contact Points
Ball in Arch
Ball in Canoe
Ball on Two Pins
Ball in Vee-Groove
Three Contact Points
Ball in Tetrahedron
Ball on Three Hemispheres
Ball in Tetrahedron with Curved Surfaces

Fig. 9 **Alternative Contact Topography for Exact Constraint**

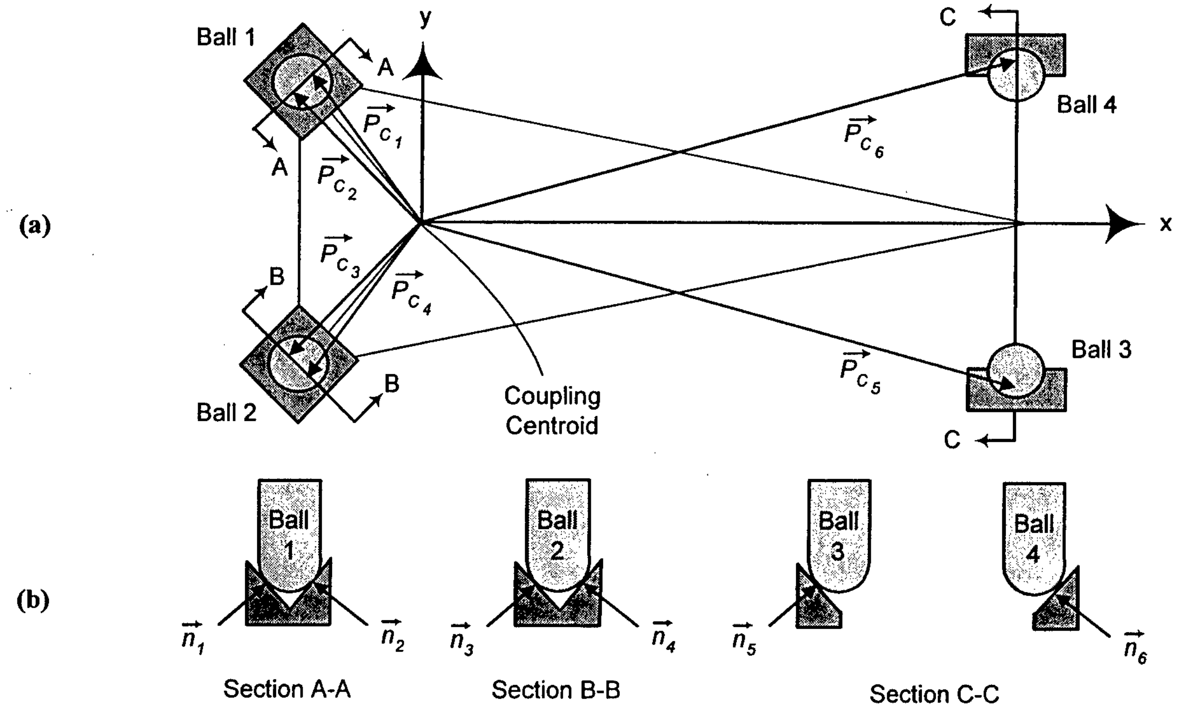
(a)
Ball 1
y
A
A
$\vec{P}_{c_1}$
$\vec{P}_{c_2}$
$\vec{P}_{c_3}$
$\vec{P}_{c_4}$
B
B
Ball 2
Coupling Centroid
C
Ball 4
$\vec{P}_{c_6}$
x
Ball 3
$\vec{P}_{c_5}$
C
(b)
Ball 1
Ball 2
Ball 3
Ball 4
$\vec{n}_1$
$\vec{n}_2$
$\vec{n}_3$
$\vec{n}_4$
$\vec{n}_5$
$\vec{n}_6$
Section A-A
Section B-B
Section C-C

Fig. 10 Model of Split-Groove Kinematic Coupling Using Position and Normal Vectors

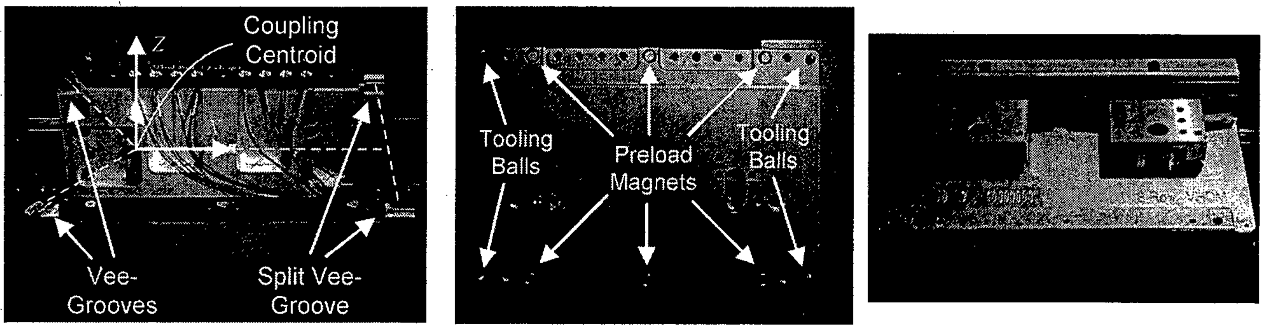
Coupling Centroid
Z
Vee-Grooves
Split Vee-Groove
Tooling Balls
Preload Magnets
Tooling Balls

(a) (b) (c)

Fig. 11 Split-groove Kinematically Coupled Pallet and Assembly Workstation (a) Machine base with vee-grooves and preload magnets, (b) Bottom of fixture plate with tooling balls and preload magnets, (c) Pallet and fixture plate kinematically coupled to machine

Title:
Sr1.eps
Creator:
MATLAB, The Mathworks, Inc
Preview:
This EPS picture was not saved
with a preview included in it.
Comment:
This EPS picture will print to a
PostScript printer, but not to
other types of printers.

Title:
Sr3.eps
Creator:
MATLAB, The Mathworks, Inc
Preview:
This EPS picture was not saved
with a preview included in it.
Comment:
This EPS picture will print to a
PostScript printer, but not to
other types of printers.

(a)

(b)

Title:
Sr5.eps
Creator:
MATLAB, The Mathworks, Inc.
Preview:
This EPS picture was not saved
with a preview included in it
Comment:
This EPS picture will print to a
PostScript printer, but not to
other types of printers.

Title
srall eps
Creator
MATLAB, The Mathworks, Inc.
Preview
This EPS picture was not saved
with a preview included in it
Comment
This EPS picture will print to a
PostScript printer, but not to
other types of printers

(c)

(d)

Fig. 12 Contour Plots of the Conditions for Equilibrium at (a) Contact Points 1 and 2, (b) Contact Points 3 and 4, (c) Contact Points 5 and 6, and (d) Intersection of the Conditions and the Disturbance Region

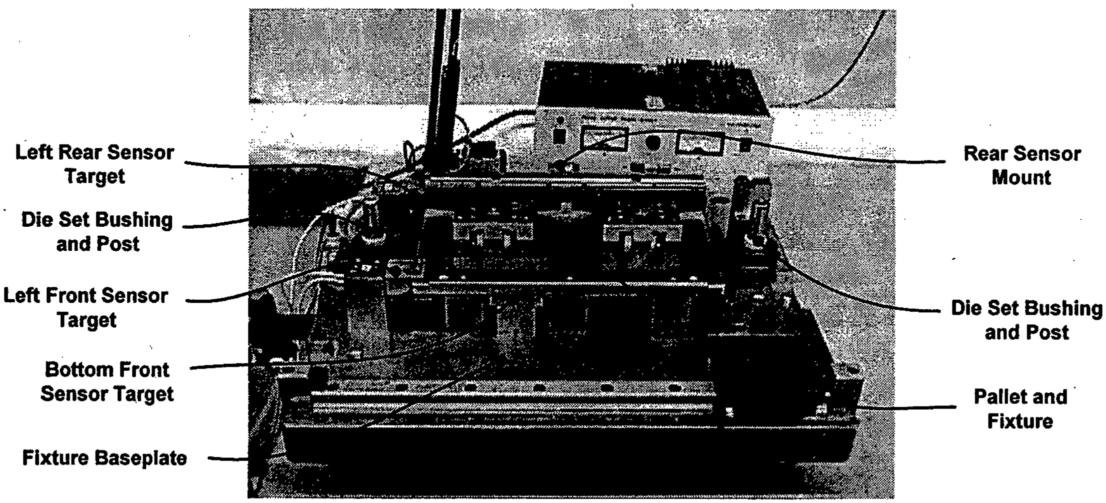
Left Rear Sensor Target
Die Set Bushing and Post
Left Front Sensor Target
Bottom Front Sensor Target
Fixture Baseplate
Rear Sensor Mount
Die Set Bushing and Post
Pallet and Fixture

Fig. 13 Experimental Setup for Measuring Pallet Repeatability

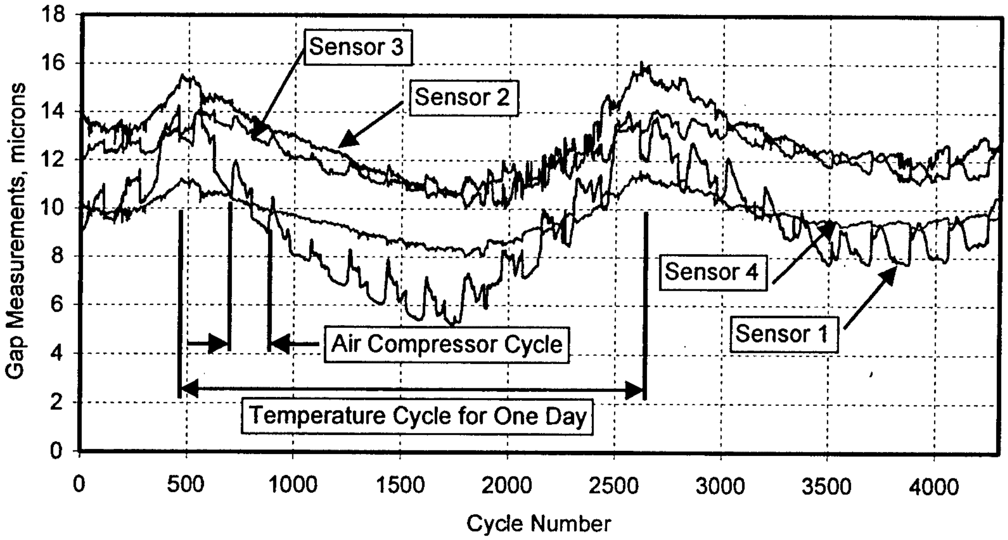

Fig. 14 **Repeatability Measurements for Split-groove Kinematic Pallet**

Captions for Figures

Fig. 1 (a) Pallet and Fixture for Holding Electrical Connector During Assembly Operations (b) Flexible Assembly System with Conveyors for Non-synchronously Transporting Pallets

Fig. 2 Commercially Available Positioning Pins and Bushings (a) Round Pin with Bullet Nose, (b) Diamond Pin with Bullet Nose, and (c) Bushing

Fig. 3 Position Method in Commercial Pallets Using Pins-In-Holes Approach (Distance Between Pins Equals 287.5 mm (11.321 in))

Fig. 4 Errors in Pin-in-Hole Positioning Technique

Fig. 5 Limits on Planar Repeatability Errors in Pallet System Using Pins-In-Holes Positioning

Fig. 6 Static Stiffness of Common Commercial Pallet Using Finite Element Analysis

Fig. 7 Configurations of Kinematic Couplings (a) Kelvin Coupling, (b) Three-groove Coupling, and (c) the New Split-groove Coupling

Fig. 8 Procedure for Designing Kinematic Couplings for Pallet Systems

Fig. 9 Alternative Contact Topography for Exact Constraint

Fig. 10 Model of Split-Groove Kinematic Coupling Using Position and Normal Vectors

Fig. 11 Split-groove Kinematically Coupled Pallet and Assembly Workstation

Fig. 12 Contour Plots of the Conditions for Equilibrium at (a) Contact Points 1 and 2, (b) Contact Points 3 and 4, (c) Contact Points 5 and 6, and (d) Intersection of the Conditions and the Disturbance Region

Fig. 13 Experimental Setup for Measuring Pallet Repeatability

Fig. 14 Repeatability Measurements for Split-groove Kinematic Pallet

Table 1 Dimensions and Tolerance of Pins and Bushing Holes for Industry Standard Pallet

Object	Geometry	Nominal Diameter Dimension	Diameter Tolerance Specification and Tolerance Range
Round Pin	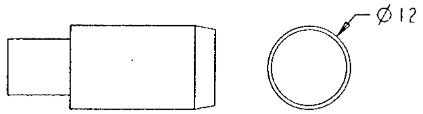	12 mm (0.4724 in)	e7 -0.0305 mm (0.0012 in) -0.0483 mm (0.0019 in)
Diamond Pin	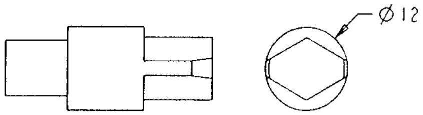	12 mm (0.4724 in)	e7 -0.0305 mm (0.0012 in) -0.0483 mm (0.0019 in)
Round Bushing	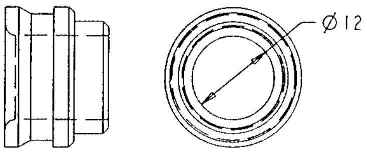	12 mm (0.4724 in)	H7 +0.0178 mm (0.0007 in) -0.0000 mm (0.0000 in)

Table 2 Dimensions of Split-Groove Kinematic Coupling

Parameter	Dimension
Coupling Length	286.91 mm
Coupling Width	203.20 mm
Split Offset	196.85 mm
Groove Angle	$\pi/2$ rad
Ball Diameter	6.35 mm

Table 3 Components of Position Vectors that Locate the Six Contact Points in Coordinate System at Coupling Centroid

Description	Vector		
	X (mm)	Y (mm)	Z (mm)
Contact Point 1	-69.97	102.90	-2.25
Contact Point 2	-73.64	100.30	-2.25
Contact Point 3	-73.64	-100.30	-2.25
Contact Point 4	-69.97	-102.90	-2.25
Contact Point 5	215.11	-100.67	-2.25
Contact Point 6	215.11	100.67	-2.25

Table 4 Components of Normal Vectors at the Six Contact Points

Description	Vector		
	X (mm)	Y (mm)	Z (mm)
Normal Vector 1	-0.5775	-0.4081	0.7071
Normal Vector 2	0.5775	0.4081	0.7071
Normal Vector 3	0.5775	-0.4081	0.7071
Normal Vector 4	-0.5775	0.4081	0.7071
Normal Vector 5	0.0000	0.7071	0.7071
Normal Vector 6	0.0000	-0.7071	0.7071

Table 5 Forces Applied to Split-Groove Kinematic Pallet

Force Description	Force Components			Position Vector		
	X (N)	Y (N)	Z (N)	X (mm)	Y (mm)	Z (mm)
Weight	0.00	0.00	-64.7	71.98	-8.80	7.07
Preload 1	0.00	0.00	-22.3	-28.73	99.31	1.78
Preload 2	0.00	0.00	-22.3	72.87	99.31	1.78
Preload 3	0.00	0.00	-22.3	174.5	99.31	1.78
Preload 4	0.00	0.00	-22.3	-28.73	-99.31	1.78
Preload 5	0.00	0.00	-22.3	72.87	-99.31	1.78
Preload 6	0.00	0.00	-22.3	174.5	-99.31	1.78
Assembly Forces	0.00	0.00	-135	-96.84 to 225.3	-44.37	89.10

Captions for Tables

Table 1 Dimensions and Tolerance of Pins and Bushing Holes for Industry Standard Pallet

Table 2 Dimensions of Split-Groove Kinematic Coupling

Table 3 Components of Position Vectors that Locate the Six Contact Points in Coordinate System at Coupling Centroid

Table 4 Components of Normal Vectors at the Six Contact Points

Table 5 Forces Applied to Split-Groove Kinematic Pallet

Precision Engineering
Journal of the International Societies for Precision Engineering and Nanotechnology
25 (2001) 235–244

ELSEVIER

PRECISION ENGINEERING

Manufacturing of cast monolithic hydrostatic journal bearings

Markku S. Kotilainen, Alexander H. Slocum*

Massachusetts Institute of Technology, 77 Massachusetts Avenue, Room 3-455, Cambridge, MA 02139, USA

Received 10 July 2000; accepted 5 October 2000

Abstract

In this work a self-compensating hydrostatic journal bearing design, which eliminates all but one precision-manufacturing step, was manufactured and tested. Novel manufacturing methods for different sizes are introduced. The bearing sensitivity to manufacturing errors was analyzed computationally using statistical methods. These results were used to show that the introduced manufacturing methods are more cost effective than the traditional precision manufacturing methods for hydrostatic bearings, even when the performance variation is taken into account. Manufactured bearings were tested and the experimental results were compared with theoretical results and satisfactory agreement was achieved. © 2001 Elsevier Science Inc. All rights reserved.

Keywords: Hydrostatic bearings; Surface self-compensation; Cost quality analysis

1. Introduction

In order to carry a load, a multi recess hydrostatic bearing supplied with a single pressure source requires compensation devices. These devices are also known as restrictors and they allow the recess pressures to differ from each other. These devices, when properly selected and tuned, can deliver excellent bearing performance. However, these devices add to the complexity of the bearing and they are sensitive to manufacturing errors. These devices must often be tuned specifically for each bearing and are therefore expensive to install and maintain [1,2].

Self-regulating or self-compensating bearings do not need any external devices to achieve load-carrying capability and they do not add to the total degrees of freedom of the system. Self-compensating hydrostatic bearings have been used for a reasonably long time, one of the earliest references being [3]. The basic idea introduced in [3] was extended in [4] and used in industrial grinding applications. However, in many cases the proposed designs require multiple precision manufacturing steps such as EDM and grinding in addition to precision shrink fit [5]. One design which does not need a precision shrink fit is the groove compensated bearing [6]. However, in groove compensated bearing the depth of the grooves is crucial and therefore economical manufacturing methods used in this work can not be utilized.

All of these hydrostatic bearing designs can be designed and manufactured to yield excellent performance, but all of them have assumed that the bearing features have to be precisely machined; hence their implementation remains expensive. In fact, in [7] it was shown that the performance differences offered by the various compensation methods and designs are not large; consequently, the most important factor is cost reduction and increase in design and manufacturing robustness.

In this work a self-compensating hydrostatic bearing design, where all the necessary geometry can be cast on the internal surface of the bearing, was manufactured. This bearing can then be shrink fitted into a bore, after which the internal surface can be machined. Only a single hydraulic line is necessary for the entire bearing regardless of the number of pockets or recesses. This makes the bearings extremely simple to install, maintain and replace. Casting is in general a low precision manufacturing method and therefore the tolerances of the surface geometry are not very good. However, as will be shown in this paper, they can still yield excellent performance and the random variation in the bearing geometry does not render the bearing unusable. It will be shown that typical casting tolerances have a very small or almost insignificant effect on the bearing performance.

The bearing geometry manufactured in this work is shown in Fig. 1. This type of bearing was introduced in

---

* Corresponding author. Tel.: +1-617-253-0012; fax: +1-617-258-6427.

E-mail address: slocum@mit.edu (A.H. Slocum).

0141-6359/01/$ – see front matter © 2001 Elsevier Science Inc. All rights reserved.
PII: S0141-6359(01)00075-7

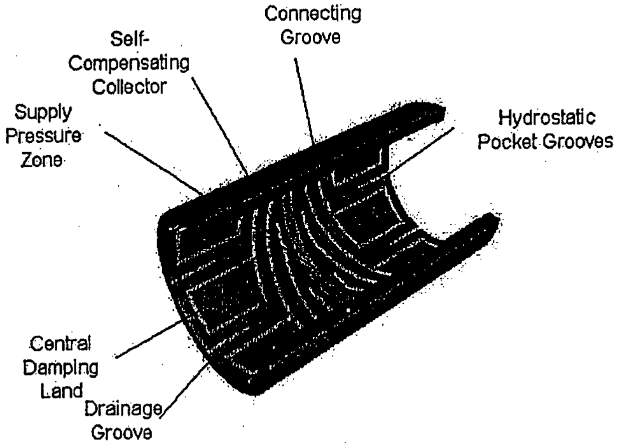

Fig. 1. Cut open view of the bearing.

[7,8,9,10], but the geometry was machined on the outer surface of the spindle shaft.

2. Manufacturing methods

In order to manufacture the internal surface geometry shown in Fig. 1, different casting and molding methods where explored. The most convenient and economically viable methods, especially for small quantities, are processes where the mold is broken after the part material has cooled. Such methods are, for example, sand casting and investment casting. Sand casting, in this case, requires a special core box to make the sand core with the desired geometry. Investment casting requires patterns for each produced part and due to the part geometry traditional pattern making methods were not applicable. Rapid prototyping methods offered the required versatility to produce the investment casting patterns. These methods were selected for producing two different size prototype bearings.

Sand casting was chosen to manufacture the 6" prototype bearings out of CDA 937 bronze alloy (80% Cu, 10% Sn and 10% Pb). In order to make the sand core with the internal diameter grooving geometry, a special core box was needed. The geometry of the grooving is such that the sand cannot be packed in a standard box, which is split in the middle into two halves, without breaking the core when opening the box. In other words, the geometry does not "draw". The box must be cut into multiple pieces in order to make the sand core with the required geometry. The following procedure was developed to make the core box:

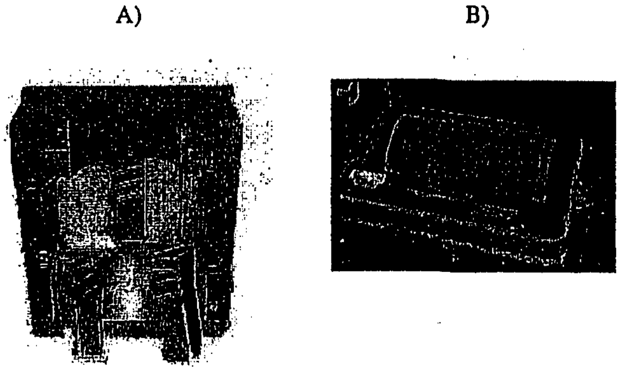

Fig. 3. A) Core-box, B) Sand core in the mold.

- Stereolithography model of the negative of the internal diameter geometry of the bushing, as shown in Fig. 2, is made.
- Epoxy is poured on the model and it is attached to the wooden frame of the core box.
- Cut the epoxy and wood into pieces in such a way that the packed sand can be removed to form the core for the casting as shown in Fig. 3.

The finished sand core is shown in Fig. 3 with the rest of the sand mold. After the bearing material is poured and cooled, the sand can be broken off and the desired geometry is achieved as shown in Fig. 4. After the bushing is cast it must be cleaned and machined into its final dimensions. These machining operations are relatively simple because the grooving can be left as cast, provided that no large residuals have been left into the grooves. For all of the prototype bushings cast (10 pieces) wire brushing the grooves was enough to clean them. The process was deemed

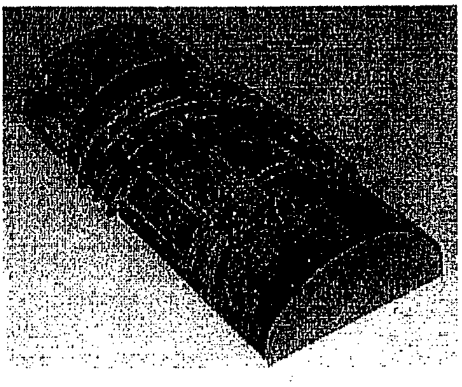

Fig. 2. Stereolithography negative of internal surface geometry.

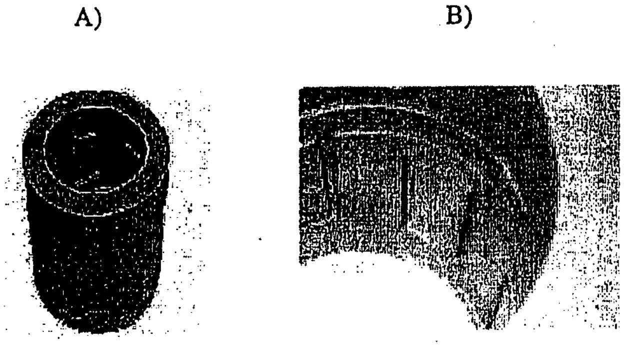

Fig. 4. A) Cast bushing, B) Groove detail.

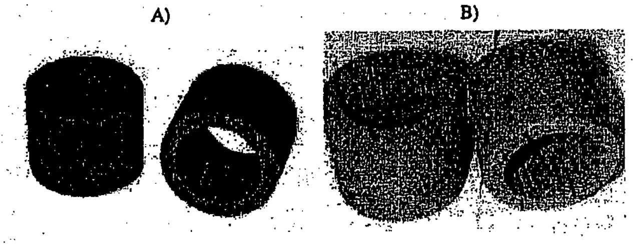

Fig. 5. A) 3D-Printed wax pattern, B) Investment cast part.

very useful for production of small or large quantities of bearings, should the need ever arise.

Investment casting was chosen as the manufacturing method for the 1.25" bushings out of CDA 872 copper alloy (89% Cu, 5% Si, 2.5% Fe, Mn, Zn, Sn). Sand casting of this size bearing becomes very difficult because the core geometry (grooves) are very intricate. The wax patterns needed for the investment casting mold were produced by 3D-Printing, which is a relatively new rapid prototyping technology. Another possibility would have been stereolithography, but this was not chosen for economic reasons.

In 3D-Printing, the part is formed layer by layer in a similar fashion to stereolithography. The part is formed by spraying binder on a bed covered by powder consisting of cellulose and sugar. After each layer is bound, the bed is lowered and next layer is formed. After the part is finished it is cleaned of excess powder and infiltrated with glue or wax. If the part needs to be investment cast afterwards, wax must be used, because the glue can form poisonous gases as the mold is emptied. Infiltration with wax is a manual process. After the waxing, the parts are baked in an oven for a few hours to make the wax penetrate all areas of the part and also to remove excess wax and make the part more durable. The finished 3D-Printed part is shown in Fig. 5.

The grain size of the 3D-Printing powder used was fairly large and therefore the surface finish of the cast part was not very good. The cast prototype bushing is shown in Fig. 5. The internal and the external surfaces of the bushings will be machined but the groove surfaces are left as cast. The surface finish of the grooves is not of concern at lower speeds when the flow is laminar (and therefore the surface finish does not affect the flow) and even at high speeds the friction losses generated in the channels represents a small portion of the total losses.

The investment casting of the wax pattern requires nothing unusual. The primary parameters of interest are the formation of the grooves and to make certain that the metal has enough free space to flow around the grooves and fill the spaces in between the grooves. This is done by designing the external diameter to be large enough. The yield with prototype bushings was about 80% which is little less than a typical investment casting yield.

Table 1
Groove width measurement statistics

Statistic	Value
Average	0.206"
Standard deviation	0.008"
Maximum Width	0.227"
Minimum Width	0.186"
Average Error	0.006"
Average Relative Error%	3%

3. Dimensional variation and its effect on bearing performance

The actual dimensional variation was measured from the manufactured parts. Table 1 summarizes the groove width measurement results.

This information is used to determine the effect of manufacturing errors to the bearing performance. This is done by statistical methods (Monte-Carlo method), as will be explained later. To effectively use statistical methods, the distribution of the dimensional variation must be determined. The standard distribution that most manufacturing errors are suggested to follow is the normal or Gaussian distribution. Most statistical process control methods assume or invoke normal distribution by the central limit theorem [11]. In this case, however, due to the non-standardness of the manufacturing methods, it was necessary to test if the measured data followed a normal distribution. This was done by the Chi-Square (χ^2) goodness of fit test. Another test must be performed before the Chi-Square test to determine that the variation in the data is random and does not have underlying trends. This was done by a run-test [12]. It was found that the variation is random and follows the normal distribution.

The static bearing performance is modeled with a hydraulic resistance network, where the bearing geometry is lumped into equivalent hydraulic resistances. More details about this modeling method can be found from [13] as applied to linear bearings. The hydraulic resistance is calculated with the assumption of one dimensional, fully developed, highly viscous flow between two flat plates. With these assumptions the Navier-Stokes equations reduce to [14]

$$\mu_f \frac{d^2u}{dy^2} = \frac{dp}{dx} \tag{1}$$

from which the hydraulic resistance can be integrated

$$R = \frac{\Delta p}{Q} = \frac{12\mu_f L}{h^3 w} \tag{2}$$

where p, L, w, Q, h, μ_f are the pressure, land length (in the direction of flow), land width, flow rate, clearance between surfaces and viscosity, respectively. If the area which is lumped into a single hydraulic resistance is small enough, the assumptions are very accurate [7,15]. How the bearing

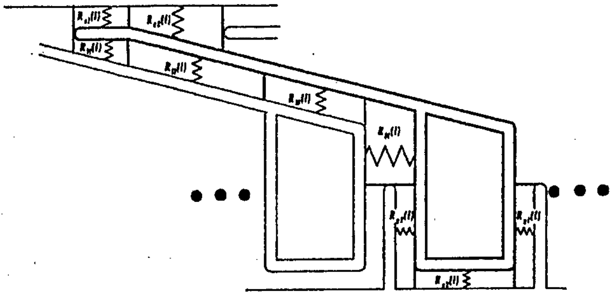

Fig. 6. Lumped parameter model.

geometry is discretized and the equivalent hydraulic resistance network is shown in Fig. 6 and Fig. 7 respectively. Only the bearing land areas are assigned hydraulic resistance, the grooves are deep enough (>15 times the clearance) so that the hydraulic resistance in them can be neglected.

The resistances R_c, R_l and R_g of Fig. 7 are the equivalents of the multiple parallel resistances

$$R_c = \frac{1}{\frac{1}{R_{c1}} + \frac{1}{R_{c2}}} \tag{3}$$

$$R_l = \frac{1}{\frac{1}{R_{l1}} + \frac{1}{R_{l2}} + \frac{1}{R_{l3}} + \frac{1}{R_{l4}}}$$

$$R_g = \frac{1}{\frac{1}{R_{g1}} + \frac{1}{R_{g2}} + \frac{1}{R_{g3}}}$$

There are 3N unknown flow rates, where N is the number of pockets in a bearing. 3N equations are needed to solve for these 3N flow rates. First, N equations are obtained by setting the total pressure drops of the upper loops to zero.

$$R_c(i)Q(i) + R_lQ(N+i) - R_c(i+1)Q(i+1) = 0 \quad i = 1, 2, \ldots, N \tag{4}$$

The second set of N equations are obtained by setting the flow rates into each central node to zero (Kirschoff's law)

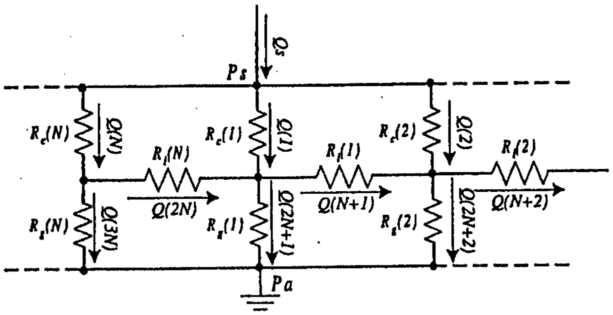

Fig. 7. Equivalent circuit.

$$Q(i) + Q(N+i-1) - Q(2N+i) - Q(N+i) = 0 \quad i = 1, 2, \ldots, N \tag{5}$$

The third set of equations is obtained setting the pressure drop across the compensators and pocket land equal to the difference between the supply and atmospheric pressure.

$$R_c(i)Q(i) + R_g(i)Q(2N+i) = P_s - P_a \quad i = 1, 2, \ldots, N \tag{6}$$

By simultaneously solving the Equations 4, 5 and 6 the unknown flow rates are obtained. Once the flow rates are obtained the pocket pressures are

$$P(i) = P_s - R_c(i)Q(i) \quad i = 1, 2, \ldots, N \tag{7}$$

Once the pressures are known the effective or average pressure on each land can be calculated. This average pressure times the area of each land is the force on each land. These forces can then be divided into components according to whichever co-ordinate system is chosen and then summed to obtain the resulting bearing force. The algorithm for solving the bearing force is the following

- Input bearing geometry and displacement.
- Calculate the hydraulic resistances for each land patch according to Equation 2.
- Form the system of equations to solve for flow rates (Equations 4–6).
- Solve for the flow rates.
- Calculate the pocket pressures according to Equation 7.
- Form the pressure field in the bearing.
- Integrate the pressure field to obtain bearing force.

This model is used to calculate the effect of manufacturing variations to the bearing performance. The same model can also be used to design bearings. This lumped parameter model can model the static behavior well, but if hydrodynamic effects are thought to be significant more advanced modeling methods are required. Next each of the land widths is assigned a probability density function (pdf), which is obtained from measuring the bearings or estimated if the variation is not known. This is conceptually shown in Fig. 8.

Since the manufacturing errors followed the normal distribution, the pdf can be written as

$$f(x) = \frac{1}{\sigma_x\sqrt{2\pi}} e^{-0.5\left(\frac{x-\mu_x}{\sigma_x}\right)^2} \tag{8}$$

where σ_x is the standard deviation and μ_x is the mean. These two parameters define the pdf and can be estimated by the sample mean and the sample standard deviation [12].

When assigning manufacturing errors it is best to assign the error in the direction where actual errors could occur. For example, the width of the element number 4 in Fig. 8 does not make a difference since this dimension exists only for modeling purposes. Instead the length (direction of the

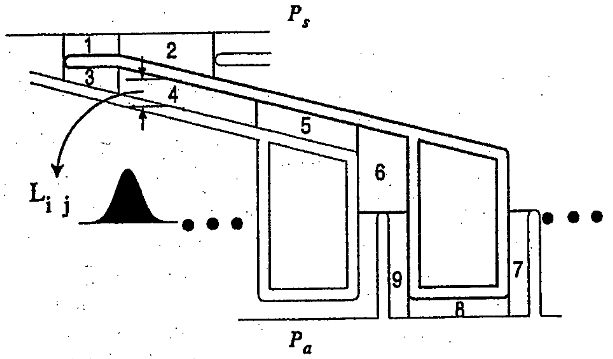

Fig. 8. Assigning pdf's to land widths.

flow) of element number 4 is a real dimension and the variation should be assigned to it. There are few assumptions one can make on how the manufacturing errors form and how they should be assigned. It is reasonable to argue that to a certain extent the manufacturing error is due to shrinkage or similar phenomena and is therefore a function of the dimension or some percentage of that dimension value. In other words, the longer the land width the larger the error. However this is not reasonable for all manufacturing methods; for example in EDM only the grooves are machined, which are a constant width resulting in constant error (constant mean and standard deviation) no matter what the land width is (due to tool error and positioning error). In the following analysis both methods are used when reasonable. Also a distinction should be made for mean error and deviation. Mean error is an error that is a constant offset from a desired value and the deviation represents the centered probability distribution around that point. The mean error is implemented as a constant offset in either direction, meaning too wide or too shallow land widths. The symbol used for this offset is $\Delta\mu$. It is also assumed that the groove width acts as a buffer dimension to keep the bearing geometry consistent with the bearing outside dimensions.

After all the assumptions are defined, the Monte-Carlo method draws random values from the pdf's assigned to each particular dimension. The combination of these values are then used to calculate a single value of output measure, for example the bearing resultant force. This is then repeated multiple times and each solution is stored in a histogram. This histogram then represents the probability distribution function for the output measure.

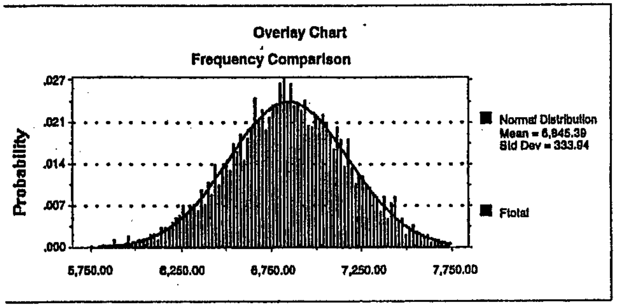

Fig. 9. Bearing force distribution with ecc = 0.1, $\Delta\mu = -4$, $\sigma = 3\%$ of groove width.

Table 2
Summary of the results for $\Delta\mu = 4$, $\sigma = 3\%$ of the land widths case

Eccentricity	F_{nominal}	μ_F	σ_F	ϕ_{nominal}	μ_ϕ	σ_ϕ
0.1	6832	6843	328	−28.1	−28.1	2.9
0.2	13139	13146	314	−28.2	−28.3	1.4
0.3	18563	18567	288	−28.5	−28.5	1.0
0.4	22966	22974	266	−28.8	−28.8	0.7
0.5	26387	26398	251	−29.1	−29.1	0.6

In the case of the 6" bearing the measured data will be used to perform the analysis. The standard deviation and the mean offset are $\sigma = 3\%$, $\Delta\mu = 4\%$ respectively. These correspond to approximately 0.2 mm errors, which is a reasonable number for this size casting. Fig. 9 shows the distribution at eccentricity = 0.1 together with the overlaid normal distribution with the computed mean and standard deviation. Table 2 summarizes the results at different eccentricities.

As can be seen the mean value in the presence of manufacturing errors in within 0.2% of the nominal value even for the low eccentricity. The standard deviation is within 5% of the nominal value for all the eccentricities.

For the 1.25" bearing, the land width data is not available. Therefore the values from the 6" bushing are used to represent the most likely error distributions. The values for the mean offset and the standard deviation are $\sigma = 3\%$, $\Delta\mu = 4\%$ of the groove width. This corresponds to approximately 0.1 mm, which is reasonable for the manufacturing method used. Results are summarized in Table 3.

Again the mean value in the presence of the manufacturing errors deviates less than 1.2% from the nominal value. The standard deviation is less than 5% from the nominal value, even for the small eccentricity. The significance of the standard deviation decreases as the eccentricity is increased, because it remains approximately constant. This suggests that for precision applications where only very low eccentricities are desirable, the manufacturing accuracy becomes more important. When the load is zero, a perfect bearing would have zero eccentricity. If this is not the case the bearing rotation center is not the geometrical center. This does not matter in the case where the bearing geometry (grooves) are stationary. In the case that the ge-

Table 3
Summary of the results for $\Delta\mu$ −4, $\sigma = 3\%$ of the land widths case

Eccentricity	F_{nominal}	μ_F	σ_F	ϕ_{nominal}	μ_ϕ	σ_ϕ
0.1	211.4	208.7	9.2	−46.2	−46.4	2.6
0.2	413.2	408.0	9.6	−46.0	−46.3	1.4
0.3	597.4	589.9	9.5	−45.7	−45.9	0.9
0.4	759.4	749.8	9.7	−46.4	−45.7	0.7
0.5	895.6	884.1	9.8	−45.2	−45.5	0.6

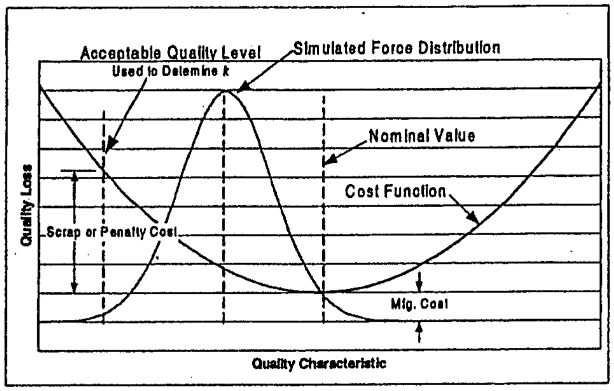

Fig. 10. The derivation of expected cost.

ometry is on the rotating element this will make the shaft center rotate around in the bore. However, the radius of this circle is fairly small, even at the 3σ limit the radius is less than 0.4 μm.

It seems that the bearing size does not have a significant effect on the sensitivity of the bearing to manufacturing errors. This can be expected if the errors introduced are relative to bearing size (groove or land widths). In the case of absolute errors the larger bearing is naturally less sensitive to errors.

4. Estimated total cost

It was attempted to derive a variable that would combine the effects of manufacturing quality with the cost of the particular manufacturing method. Very often the cost vs. quality comparison is made on a qualitative basis, based on existing knowledge or experience between manufacturing methods. Assumptions very often also include the sensitivity to manufacturing errors, which are not necessarily very well known. In this work a cost function concept by Taguchi [16] is combined with the derived bearing force probability density function to yield estimated total cost. This is done in terms of mathematical expectation.

Taguchi argues that it is important to think quality in terms of the loss imparted to society during product use as a result of functional variation and harmful effects. Taguchi defines quality as loss due to functional variation and further argues that the loss is minimized (as it should be) when performance is at the design nominal and that the cost increases as the performance deviates from the nominal. In many cases a quadratic loss function is appropriate [11]. It is not enough to define some arbitrary function to make any meaningful comparisons. This function has to be somehow consistently related to the performance of the product. One way to do this is to define some acceptable quality level or variation from nominal and associate a cost to the product when this variation is exceeded. This cost can be, for example, scrap cost or some penalty cost at that point. This way the loss function becomes:

$$L(x) = k(x - x_0)^2 \tag{9}$$

where x is the quality characteristic, x_0 the intended target value and k the factor used to calibrate the cost function. To define a cost function from the loss function the manufacturing cost is added to the loss function. It could be argued that in the case of the bearing the loss function should not exist beyond the nominal value, meaning that no loss should be associated with the bearing if it carries more load than intended. This argument makes sense in most cases, but philosophically it could be argued that resources are wasted if the performance is better than nominal. The latter approach is used here. The quadratic function will be used in this case.

$$C(x) = k(x - x_0)^2 + M \tag{10}$$

where M is the manufacturing cost. The expected cost is defined as the expected value of the cost function. The probability density function used will be the one computed earlier. The quality characteristic will be the bearing force. This way the probable performance of the bearing is related to the cost function. Fig. 10 shows the cost function and the quality characteristic distribution which, in this case, is the bearing force F.

The expected value of the cost becomes

$$\begin{aligned} E(C(F)) &= \int_{-\infty}^{\infty} C(F)p(F)dF \\ &= \int_{-\infty}^{\infty} [k(F - F_0)^2 + M] \\ &\quad \frac{1}{\sigma\sqrt{2\pi}} e^{-0.5\left(\frac{F-\mu}{\sigma}\right)^2} dF \end{aligned} \tag{11}$$

where σ and μ are the mean and standard deviation calculated earlier. By expanding the square and taking into account the following relations

$$\begin{aligned} &\int_{-\infty}^{\infty} p(x)dx = 1 \\ &\mu = \int_{-\infty}^{\infty} xp(x)dx \\ &\psi^2 = \int_{-\infty}^{\infty} x^2p(x)dx = \sigma^2 + \mu^2 \end{aligned} \tag{12}$$

the expected value becomes

$$ETC = E(C(F)) = k(\sigma^2 + (\mu - F_0)^2) + M \tag{13}$$

where

$$k = \frac{X}{(1 - \vartheta)^2 F_0^2} \tag{14}$$

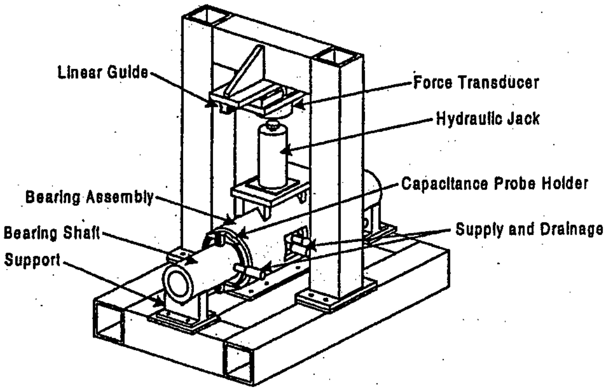

Fig. 11. General view of the 6" prototypes test set-up.

where X is the penalty cost and, ϑ is the fraction of nominal value at which the penalty cost is applied, σ is the calculated standard deviation and μ is the calculated mean. *ETC* stands for expected total cost.

Here the penalty cost is set at manufacturing cost M at 10% deviation from the nominal value. The *ETC* is a function of eccentricity. The smaller the eccentricity at which the *ETC* is calculated the higher the value will be. Here the *ETC* will be calculated at a small eccentricity of 0.1. The estimated total costs becomes 1.65 and 1.2 times the manufacturing cost for the 1.25" and 6" bearings respectively. When this cost is used in cost versus quantity analysis, it is concluded that the methods used in this work are more cost effective than other conceivable manufacturing methods. For smaller sizes it is possible to injection mold the bearings out of plastic. This method becomes more cost effective than at larger quantities (approximately more than 300 bearings).

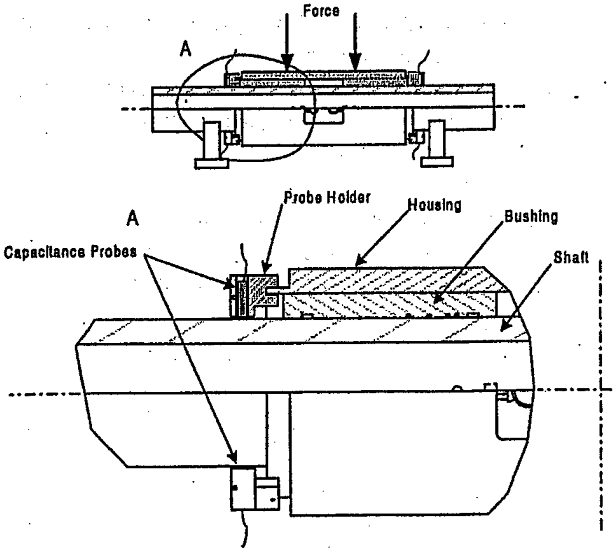

Fig. 12. Detailed view.

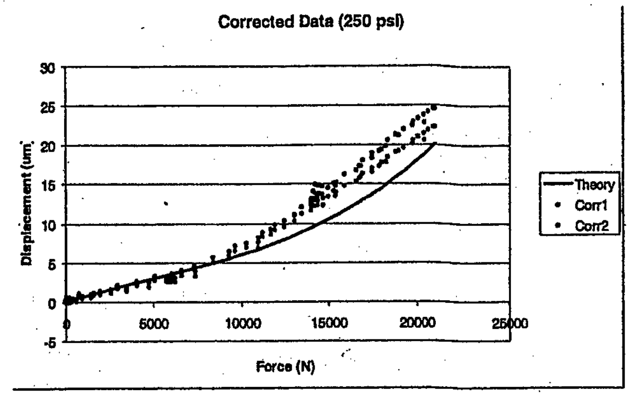

Fig. 13. Corrected force-displacement curves at 250 psi with 50k force transducer. (Corr1 = corrected results of the probe 1 (left), Corr2 = corrected results of the probe 3 (right)).

5. Testing

The static stiffness of both the 1.25" and the 6" prototypes were tested in order to get experimental proof that the economical manufacturing methods do indeed work. In addition, the error motion of the 1.25" prototype was measured.

Fig. 11 shows the general view of the test bed and Fig. 12 shows a detailed view of the bearing assembly for the 6" prototype. The displacement measurements were taken with capacitance probes and the force with force transducer. The data was collected with a data acquisition board on a personal computer.

Due to the very high stiffness of the bearing system the elastic deflections of the shaft had to be subtracted from the test results, even though the test set-up was designed in such way that the effect of these deflections is minimized. The elastic deflections of the shaft were calculated with a simple beam finite element model which takes the shear deformations into account. The word corrected in some of the figures refers to this subtraction of elastic deflections of the

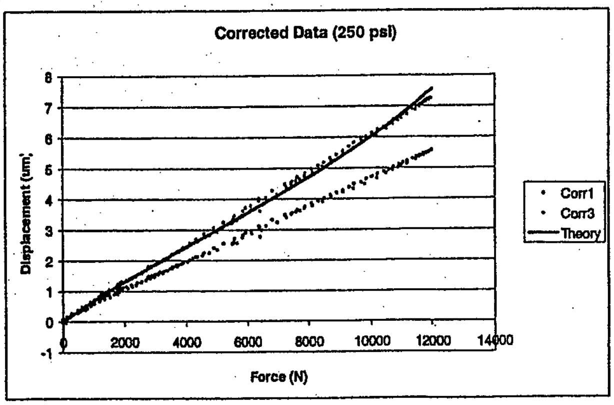

Fig. 14. Corrected force-displacement curves at 250 psi supply pressure and the 5k force transducer. (Corr1 = corrected results from probe 1 (left), Corr3 = corrected results from probe 3 (right)).

Table 4
Initial stiffness at 250 psi

Measure	Value	Unit
Predicted Initial Stiffness	1770	N/μm
Measured Initial Stiffness	1915	N/μm
Difference	7.6	%

test set-up. The force-displacement curve is shown in Fig. 13.

The agreement is excellent until about 10 000 N. At loads greater than about 10 000 N the theory predicts the bearing to be stiffer than the measurements indicate. This can be expected due to the model that neglects curvature effects in a bearing gap. Also the procedure to predict the correction and the way the theoretical curve is computed is not entirely correct. The bending of the shaft makes the bearing clearance vary along the bearing which in turn has an effect on the bearing pressure distribution which in turn effects the load capacity and therefore the displacement of the bearing and the shaft. This is clearly an iterative problem. In order to solve this problem the bearing model has to be coupled with a beam model. When designing a bearing for a certain application this should be taken into account, but due to the inaccuracies of the testing and the parts it does not add any information in this case. In addition, usually only the small displacements are of concern because hydrostatic bearings are operated at small eccentricities.

To get an even better idea of the force-displacement behavior this measurement was repeated with the less noisy 5k lbs force transducer for the smaller displacements of interest. Fig. 14 shows these results. In this case it seems that the forcing device was not quite centered and the bearing assembly tilted slightly. Agreement is still very good and the probe that deviates more from theory actually shows stiffer bearing than the theory.

As can be seen, the bearing behaves very linearly when displacements are small. This justifies the use of a single number to describe the stiffness of the bearing. It must be noted, however, that this number is only the initial stiffness and in the case of large displacements the non-linearity of the behavior must be taken into account. Table 4 shows the initial stiffness as predicted and measured with a 250 psi supply pressure. The measured initial stiffness is taken to be the average of the two measured and plotted in Fig. 14. The agreement is entirely satisfactory and it can be concluded that the bearing with cast hydrostatic features behaves as would be expected of a bearing with machined hydrostatic features. Fig. 15 shows the test set-up for the 1.25" bearing.

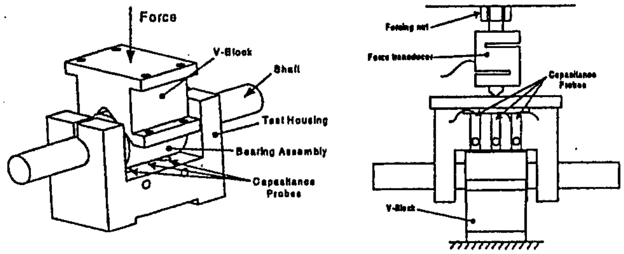

Fig. 15. General and side view of the test set-up. General view is rotated upside down for clarity.

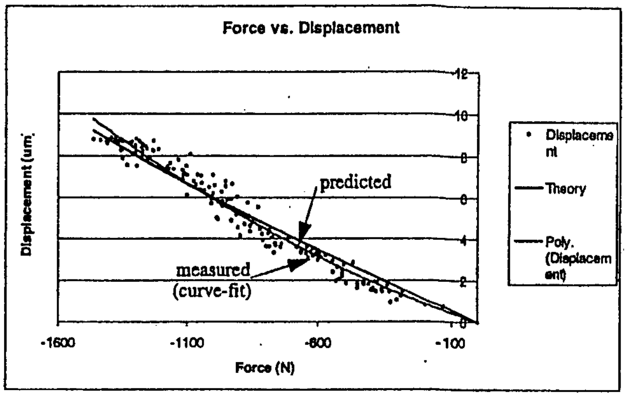

Fig. 16. Force displacement results at 500 psi.

The force-displacement curve is shown in Fig. 16 together with the predicted curve and the curve fit for the measurements, for the 1.25" prototype. The agreement between the measured and theoretical values is excellent except for the relatively high noise. This noise is due to the too large force transducer and the vibrating forcing structure. The agreement is good enough so that it is not necessary to redo the test with a more sensitive force transducer.

Here again the displacement was only measured up to approximately 10 μm, which is approximately one half of the bearing clearance. This is the most interesting part of the bearing behavior from an application point of view. Also the tilting motion resulted in capacitance probes touching the bearing at larger forces.

The initial stiffness (taken as a linear fit at 500N) is presented in Table 5. The maximum relative error between the curve fit and the predicted data was 24.4% and the average relative error 8.4%. The maximum error occurred at small displacement and the absolute value of the error was only 0.14 μm.

The error motion of the 1.25" prototype was measured by the two probe rotating sensitive direction method and the error motions were computed from a least squares circle (LSC) [17]. This was done by solving the following unconstrained optimization problem.

Table 5.
Initial stiffness of the 1.25" prototype

Measure	Value
Predicted Stiffness	170 N/μm
Measured Stiffness (curve fit)	185 N/μm
Relative Error	8.1%

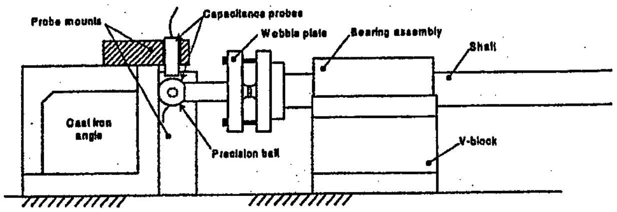

Fig. 17. The error motion test set-up.

$$\min\left(\sum_{i=1}^{n}\{[(x_i-x_0)^2+(y_i-y_0)^2]^{1/2}-R\}^2\right)$$

$$\text{w.r.t } x_0, y_0, R \qquad (15)$$

where subscript i refers to a measured point and the optimization variables are the coordinates of the center point (x_0, y_0) and the radius of the LSC (R).

Some special arrangements had to be made in order to measure this bearing, since it does not have a thrust bearing. The test set-up consists of the bearing assembly, V-block, shaft, wobble plate, precision ball and a precision cast iron angle. The whole set-up is assembled on a surface plate which is at a very slight angle from the horizontal (approximately 0.0005:1). This slight tilt together with gravity is used to preload the shaft against the cast iron angle. The precision ball contacts the cast iron angle and acts as a thrust bearing. The ball is a 1" diameter grade 5 steel ball (spherity of the ball is within 5 microinches or 0.127 μm). The wobble plate is used to offset the ball from the center of the rotation. The viscous forces due to the fluid flowing in the grooves is enough to rotate the shaft slowly (10–20 s/rev depending on the pressure). Therefore, no external drive is needed to rotate the shaft. The motion is measured with two capacitance probes. The data is collected with a National Instruments PMCIA data acquisition card and processed with Labview software and saved into a ASCII file for further analysis. A drawing of the test set-up is shown in Fig. 17. This set-up measures both radial and angular error motions combined without separating them.

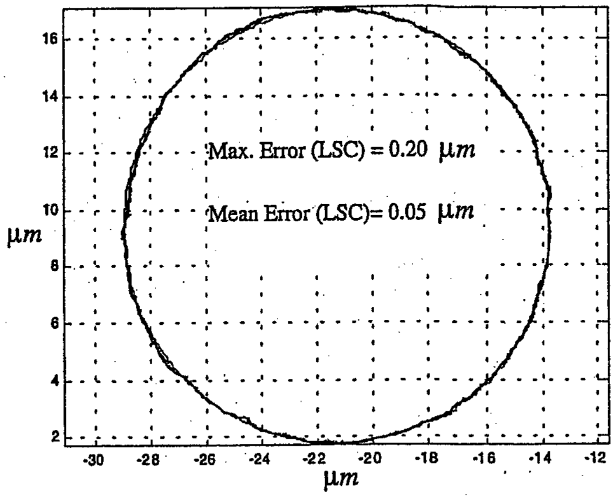

Fig. 19. Error motion for multiple revolutions.

Possible error sources in the measurement are the environment noise, the ball spherity errors, probe alignment, friction force caused by the ball touching the cast iron angle and the pump pressure pulsations. The pump pressure pulsations are inherent to a hydrostatic system, but by carefully designing a hydraulic system with sufficient accumulators, this effect can be made smaller.

In Fig. 18 the motion trace for a single revolution is shown. The maximum deviation from LSC is 0.17 μm and the mean deviation 0.055 μm.

In Fig. 19 the motion trace for multiple revolutions is shown. The maximum deviation from LSC is 0.20 μm and the mean deviation 0.05 μm. This test was run at 6 rpm and there are 10 revolutions in the error motion trace.

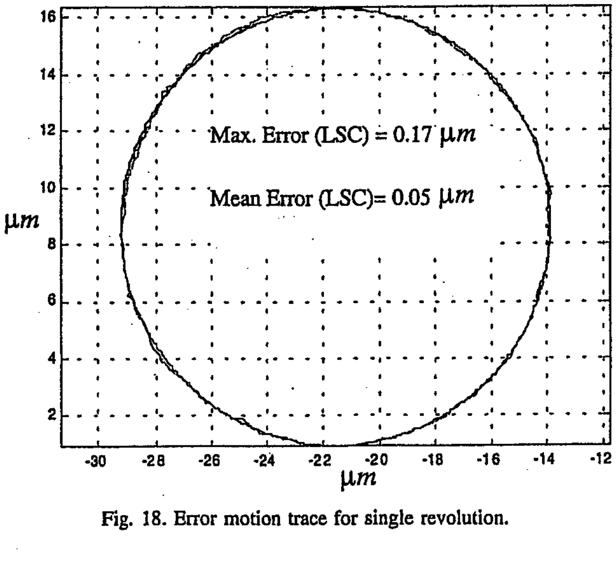

Fig. 18. Error motion trace for single revolution.

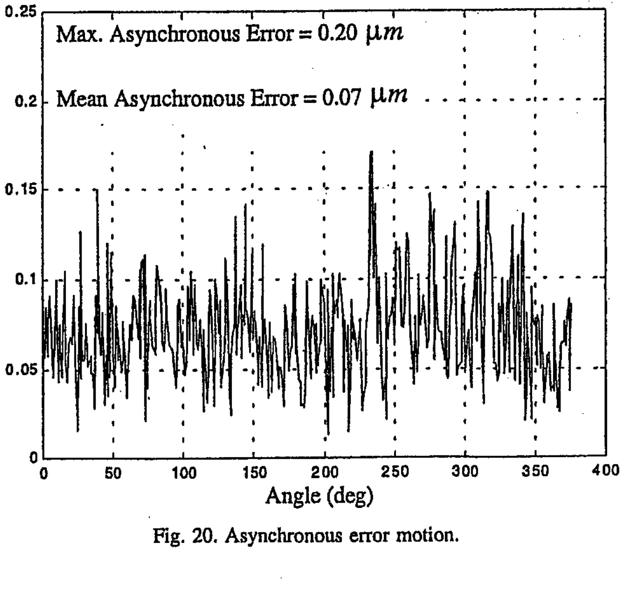

Fig. 20. Asynchronous error motion.

By looking at the error motion trace it seems that the largest deviations from the LSC are of fairly short wavelength. This would seem to indicate a scratch with a burr on its edges in the bearing surface or a dimple either in the ball or in the bearing surface. A fairly large surface feature would be necessary in the bearing for it to produce a significant deviation, because of the error averaging effect of the oil film. The cylindricity and roundness tolerance for the internal surface was 5 μm. This indicates an error reduction by a factor of approximately 25.

The asynchronous error motion for the error motion trace of Fig. 19 is shown in Fig. 20. The maximum asynchronous error motion is 0.20 μm and the mean asynchronous error motion is 0.07 μm. Spectral analysis of the asynchronous error motion does not reveal any specific frequencies at which the error occurs.

6. Conclusions

In this work two novel manufacturing methods for monolithic self-compensating hydrostatic bearings were introduced. Only one precision manufacturing step is required to implement these bearings. Manufacturing methods were very low cost and not highly accurate. It was shown that the accuracy of the surface features is not of concern and that even when quality is taken into account the methods introduced are very cost effective. Prototypes were manufactured with both methods and tested. Good agreement between computed theoretical results and the experimental results was achieved. Error motions of the smaller prototype were measured and the average error motion was found to be less than 0.05 μm and the maximum error motion less than 0.2 μm. Both of these values are the same order of magnitude as the ball spherity and measuring environment noise.

References

[1] Bassani R, Piccigallo B. *Hydrostatic Lubrication,* Elsevier Press, Amsterdam, 1992.

[2] Slocum A. Precision Machine Design, Elsevier Press, New Jersey, 1992.

[3] Hoffer, US Patent #2,449,297 September 1948.

[4] Hedberg OJ, US Patent #3,754,799 August 1973.

[5] Devitt A, Slocum AH. Method for manufacturing externally pressurized bearing assemblies, US Patent #5,488,771, February 6, 1996.

[6] Arneson HGE. *Hydrostatic Bearing Structure.* US Patent #3,305,282, February 21, 1967.

[7] Wasson K. *Hydrostatic Machine Tool Spindles,* MIT PhD. Thesis in Mechanical Engineering, Cambridge, 1996.

[8] Wasson K. *Integrated Shaft Self-Compensating Hydrostatic Bearing.* US Patent #5,700,092, December 23, 1997.

[9] Wasson KL, Lienhard JHV, Slocum AH. Thermal performance of hydrostatic radial bearings for precision machine yool applications, ASME WAM, Nov 1993.

[10] Schaffa R, McCabe JT, Wasson K. Advanced hydrostatic bearings for a new class of machining spindles. Advanced Technology Program Motor Vehicle Manufacturing Technology Public Workshop, National Institute of Standards and Technology, NISTIR 6079, October 1997.

[11] DeVor R, Chang T, Sutherland J, *Statistical Quality Design and Control,* Prentice Hall, New Jersey 1992.

[12] Bendat J, Piersol A, *Random Data: Analysis ans Measurement Procedures,* John Wiley & Sons, Inc, New York, 1971.

[13] Slocum AH, Scagnetti PE, Kane NR, Brünnner C. Design of self compensated water-hydrostatic bearings, Precision Eng, Vol 17, No 3, 1995, pp 173–85.

[14] Fay J, *Introduction to Fluid Mechanics,* MIT Press, Cambridge MA, 1994.

[15] Kotilainen M. *Design and Manufacturing of Modular Self-Compensating Hydrostatic Journal Bearings,* MIT PhD. Thesis in Mechanical Engineering, Cambridge, 2000.

[16] Taguchi G, Elsayed A, Hsiang T. *Quality Engineering in Production Systems,* McGraw-Hill, New York, 1989.

[17] ANSI/ASME B89.3.4M 1985, *Axes of Rotation, Methods for Specifying and Testing.* ASME New York 1985.

A Hybrid 5-Axis CNC Milling Machine

Seung-Kil Son, Taejung Kim, Sanjay E. Sarma[†] and Alexander Slocum
Department of Mechanical Engineering
Massachusetts Institute of Technology
Cambridge, MA 02139

ABSTRACT

5-axis CNC milling machines are important in a number of industries ranging from aerospace manufacturing to consumer-die-mold machining. Hopes of higher stifness, better mobility, and smaller footprints have lead designers recently to explore new alternatives such as parallel kinematic machines, especially in the context of high speed machining, where these attributes are critical. However, many researchers, including us, have shown that most of the promised advantages of parallel machines occur within a relatively small region of their workspace. We discuss some of the kinematic and structural challenges to extracting machining performance from serial and parallel machines. We describe a new hybrid 5-axis machine tool which combines serial and parallel mechanisms, and compare it with standard, purely serial and purely parallel configurations such as Euler angle machines and a hexapod. In particular, we consider singularities, reversal characteristics, manipulability and manufacturability. We show that hybrid machines can benefit from the advantages of serial and parallel mechanisms while avoiding most potential pitfalls. However, hybrid structures can suffer from the manufacturing problem of over-constraint. We show that the degree of over-constraint depends on machine size. We have designed a small hybrid 5-axis motion platform, the MIT-SS-1, which can tolerate this over-constraint through a novel layout of axes. We show preliminary results of this new machine tool.

1. INTRODUCTION

Machine tool users perpetually seek faster, stiffer, more compact and more accurate machines. In addition, machine tools with 4 or 5 axes and greater reach and dexterity are becoming more and more important as the complexity of consumer parts grows, and as the automotive and aerospace industries face greater performance challenges. The hexapod, shown in Figure 1, and the larger class of machines referred to as parallel kinematic machines (PKM's), have recently received increased attention in the context of machining. When hexapod machines first emerged as a possible machine tool configuration in the early nineties, there was considerable excitement in the machine tool user community about their potential. Unfortunately, the trade-offs in the design of hexapod are mathematically inescapable, and this usually leads to quirks in performance—such as an oddly shaped workspace or varying speed capability in the workspace. Consider for example, the trade-off between stiffness, workspace size and machine-tool footprint. A feature much anticipated of hexapods in machine tool magazines a few years ago was greater reach, stiffness and accuracy for a machine tool of relatively small footprint [1]. However analysis suggests that the stiffness of the hexapod is very sensitive to its location in the workspace, and indeed that the stiffness and accuracy drop rapidly as the spindle moves away from the "sweet-spot" of the machine

---

[†] Corresponding author. Professor Sanjay E Sarma, 35-010, MIT, Cambridge MA 02139, USA.
TEL: (617) 253 1925; FAX: (617) 253 7549; E-Mail: sesarma@mit.edu

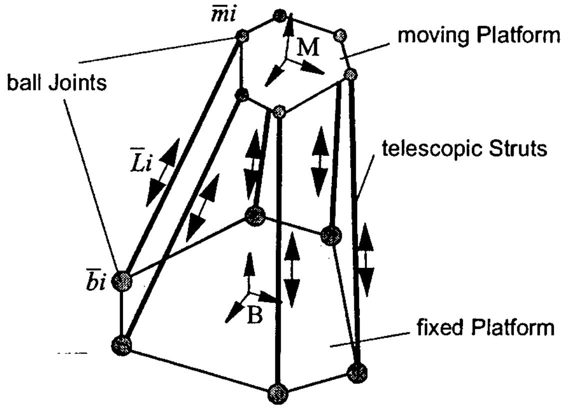

Figure 1 Stewart Platform

[2]. In fact the stiffness vanishes completely in certain configurations known as singular configurations.

At the same time, serial mechanisms have a number of drawbacks which do make PKM's attractive. One major problem with serial machines is that serially stacked-up axes tend to balloon in size—joints lower in the serial chain, which carry the higher joints, must be larger and stiffer, and this effect cascades serially. A stack-up of 3 axes, which is necessary in a 5-axis machine, is always limiting because to achieve static stiffness, the structure needs to be quite substantial, which reduces dynamic performance. PKM's, on the other hand, have less moving mass because they don't suffer from this form of stack-up. Another common problem in 5-axis serial machines, which has as yet received little attention in the machine-tool literature, is "manipulability" loss. Many 5-axis machine tools today have a degree of freedom known as the C-axis. The attraction of the C-axis is that it is compact, and mitigates the stack-up problem — but results in loss of performance. When the spindle is oriented parallel to this axis, it may enter a state similar to gimbal lock. In a sense, this loss of manipulability is a mathematical dual of the kinematic singularity.

In many ways, PKM's and serial machines are the opposites of each other. For example, while it is the solution of the forward kinematics of PKM's which is difficult, it is the inverse kinematics of serial machines which pose the real challenge[†]. While serial machines have the problem of axis stack-up, and therefore more error build-up, PKM's have extra passive joints in the structure, providing more scope for compliance build-up. There are other such dualities, and some researchers have argued that a hybrid concept, which combines the benefits of parallel and serial machines, avoiding the pitfalls of both, may be the ideal configuration [3]. In this paper we describe the MIT-SS-1, which is a hybrid 5-axis structure designed specifically to avoid the pitfalls of parallel and serial machines. We also list the kinematic and structural problems that machine designers must be aware of in the synthesis of serial, parallel or hybrid machines, and we show how the MIT machine addresses these problems.

This paper is organized as follows. In Section 2 we present a brief review of the literature surrounding new parallel structures. In Section 3, we list a series of kinematic and structural considerations that must be kept in mind in the design of machines, both serial and parallel. In Section 4 we go through the reasoning process of selecting a kinematic structure that minimizes the downsides of both serial and

---

[†] There are no passive joints in serial machines, making it easier to find an end-effector position and orientation from known actuator coordinates. Passive joints in PKM's generally make it difficult to find an end-effect position and orientation from actuator coordinates (and there may be multiple solutions) , but it is easier to find active joint coordinate from known end-effector coordinate.

PKM's. We describe the MIT Hybrid Structure in Section 5, and show how it fares with the remaining considerations. In particular, we point out the problem of over-constraint and show that it can be addressed with a novel axis layout. In Section 6 we summarize some of the performance targets for this machine. We describe a moving-bridge variant of the structure in Section 7, which can be used as a 4-axis machine for manufacturing long aerospace spars or marine components. We conclude in Section 8.

2. LITERATURE REVIEW

Over the last decade, PKM's have garnered much attention in machine tool research area because of their inherently high structural rigidity and low inertia. The machine tool industry and research universities have developed and evaluated various type of PKM's in an effort to adopt the advantages of parallel mechanisms for 5-axis machine tools. Several prototypes including the *Triaglide* by ETH and *HexaM* by Toyota have been reported to have comparable performance to conventional machine tools [4,5]. There are over 20 hexapod machine tool designs in existence world-wide, and many more in existence for pick-and-place applications. A broad discussion about machine tool applications of parallel mechanism and existing prototypes in industry is available in [6]. The website [7] contains an ongoing list of machines.

In designing PKM's, the most time-consuming process is often the conceptual design phase because it determines the fundamental structural characteristics on which machine performance and manufacturing costs depend. A design methodology using connectivity which is defined as the degrees of freedom (dof) associated with the joints of the limb in parallel manipulators was introduced by L. Tsai [8]. Once the connectivity of each limb is decided, a joint type can be assigned and feasible configurations of limb mechanisms can be enumerated using combinatorial analysis. From an engineering point of view, G. Pritschow and K-H. Wurst describe a systematic design process for parallel manipulators using 3-dof arm elements [9]. By constraining the joint type, infeasible design candidates can be removed at conceptual design. One of the most critical challenges in the design of PKM's is that of actuator singularities in the workspace. A. Karger and M. Husty [10] demonstrate all possible actuator singularities in the original Stewart-Gough platform. When the Jacobian matrix or inverse Jacobian matrix loses rank, the mechanism loses its mobility or rigidity and the configurations are called kinematic or actuator singularity [2,11].

Several researchers have qualitatively or quantitatively evaluated PKM's for use in machine tools considering stiffness, acceleration and dynamic performance. Tlusty *et. al.* show that PKMs with fixed length struts are possibly comparable to the conventional Cartesian machine tools in particular applications in [12]. El-Khasawneh and P. Ferreira [2] compare the advantages and disadvantages of serial and parallel mechanisms qualitatively and also develop kinematic theory related to stiffness near singularities. They were among the first to suggest hybrid serial-parallel concepts as an approach to melding the advantages of serial and PKM's. In [3] the same authors also describe a hybrid 3-axis platform. Tonshoff and Grendel [13] observe that in production engineering, most applications of parallel mechanisms have been in the role of robots and positioning devices. For machine tool applications, they too compare drive mechanisms, and suggest the use of fixed strut and rotary arm joints as favorable for tasks which require high forces and high speeds.

Q. Tu and J. Rastegar [14] argue that the complicated kinematics of PKM's create a need for stiff actuators and for proper tracking control, and that they cause more frequent actuator reversals which occur when actuators change their directions of motion. Friction characteristics become very complicated near zero velocity regions and controllers without friction compensation cannot recognize and compensate these changes. This induces trajectory errors. Accurate friction compensation is difficult to implement [15]. B. Armstrong-Helouvry, P. Dupont and C. Wit [16] broadly discuss existing compensation methods for motion control with friction in their survey paper.

The study of PKM's, and our work, also draws significantly from the robotics community. Some valuable resources where various types of singularities are described are [11]. The robotics community has also studied manipulability in many contexts [17,18].

3. KINEMATIC AND STRUCTURAL CHALLENGES OF SERIAL AND PARALLEL STRUCTURES

In this section we list the kinematic and structural challenges that must be addressed in the design of a machine tool. The considerations shown here include standard kinematic theory, new kinematic observations and some practical considerations gathered from our experience in using and designing machine tools.

3.1. Singularities in serial and parallel machines

Let X be the end-effector configuration and Θ be the active joint angles of a machine tool, which are specified by 5-tuples.

$$X = \begin{bmatrix} x \; y \; z \; a \; b \end{bmatrix}^T \tag{1}$$

$$\Theta = \begin{bmatrix} \theta_1 \; \theta_2 \; \theta_3 \; \theta_4 \; \theta_5 \end{bmatrix}^T . \tag{2}$$

where x, y, and z are the translational Cartesian coordinates of the machine, and a and b are the rotational coordinates, in some pre-selected reference frame attached to the world, and where θ_i are the displacement of the 5 linear or rotary actuators in the machine. In 5-axis machine, the degree of freedom associated with the space about tool axis is not in out interest. The relationship between X and Θ can be written as

$$F(X, \Theta) = O \tag{3}$$

where F is a 5 dimensional column vector. By differentiating Equation 3 with respect to time, we have:

$$F_X\dot{X} + F_\Theta\dot{\Theta} = O \tag{4}$$

where $F_X = \frac{\partial F}{\partial X}$ and $F_\Theta = \frac{\partial F}{\partial \Theta}$.

If F_X is not singular, the Jacobian, J, of the mechanism, which is useful for investigating kinematic properties, such as manipulability, kinematic and actuator singularities of the mechanism, can be obtained by using F_X and F_Θ as in Equation 5.

$$J(X, \Theta) = -F_X^{-1}F_\Theta \tag{5}$$

so that $\dot{X} = J\dot{\Theta}$. Likewise, we define, $J^{-1} \equiv -F_\Theta^{-1}F_X$, when F_Θ is not singular. When $|F_X|$ or $|F_\Theta|$ becomes zero, the structure experiences either kinematic or actuator singularities.

3.1.1. Actuator Singularities in PKM's

Actuator singularities are a well-studied phenomenon in the robotics literature [11]. The amount the tool deflects in the face of cutting forces is determined by the static and dynamic stiffness of the system. In some configurations of parallel mechanisms, actuator forces are not transmitted to the end-effector and the end-effector can not resist external forces in some directions. These configurations are called actuator singularities and they can be investigated by looking at the Jacobian. In general, near singularities, the stiffness of the structure is usually much lower than far away from singularities. The workspace of the machine where high stiffness is achieved can therefore be related to the location of the points of singularity.

The torques and forces, T, on the end-effector are related to actuator torques and forces, G, as follows [2].

$$T^T \Delta X = G^T \Delta \Theta . \tag{6}$$

The equation above can be written in terms of the Jacobian and the actuator forces as follows:

$$T = J^{-T} G . \tag{7}$$

Clearly, when J^{-1} or F_{Θ} loses rank, the end-effector loses the capability of resisting force or torque in some direction. It can also be shown that in the neighborhood of these singularities, the machine becomes mechanically disadvantaged [2]. Joint compliances become magnified, and machine stiffness is greatly compromised. This problem is especially severe in PKM's because these mechanisms have *many passive joints*, whose compliances add up.

3.1.2. Kinematic singularities in serial machines

Interestingly, actuator singularities don't occur in serial mechanisms. However, a dual of the actuator singularity exists for serial machines, which we refer to as a kinematic singularity. Essentially, serial machines instantaneously lose a degree of freedom. Paths except very special ones which pass these configurations cannot maintain velocity tracking, which is a serious drawback, especially in high-speed machines. *A large number of serial machines today suffer from this drawback.*

The effect can be demonstrated though the Jacobian. In some configurations, the rank of Jacobian matrix drops, and in these configuration, the mechanism looses manipulability in some directions [19]. When the end-effector velocity is known, the required actuator velocity can be obtained with from Equations 4 and

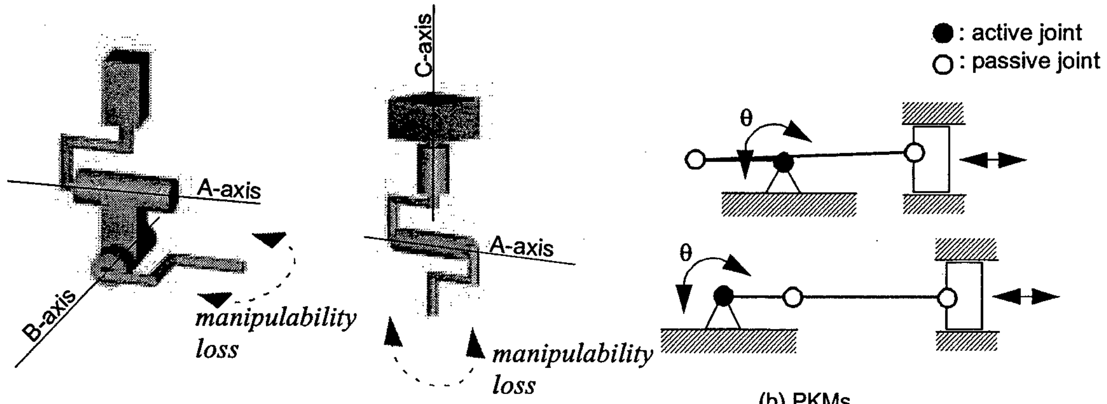

(a) Euler-angle machine tools

(b) PKMs

Figure 2 Kinematic singularity configurations

5 as shown in Equation 8:

$$\dot{\Theta} = J^{-1}\dot{X} = \frac{1}{|J|}adj(J)\dot{X} \tag{8}$$

Equation 8 implies that infinite actuator velocity is required at a kinematic singularity to achieve any end-effector velocity.

This singularity is very common in conventional Cartesian 5-axis machine tools which incorporate two rotational axes. The nomenclature for axes is as follows: rotation axes aligned (in home position) parallel to the *x*, *y* and *z* axes are referred to as the A-, B- and C- axes respectively. In 5-axis serial machines, two of these three rotational axes are typically used as shown in Figure 2-(a). This implies that there are configurations of the rotational axes in which the spindle axis is aligned with one of the two rotational axes. Let $\vec{q}$ be the unit vector aligned with spindle axis and q_x, q_y, q_z be its components. Let a, b, c be the Euler angles corresponding to A, B, and C axes. Vertical type Euler angle machine tools use only (a, c) or (b, c) axis pairs, and horizontal type Euler angle machine tools use only a, b. In the case of vertical machines, because $q_z = cos(a)$, differentiating q_z with respect to time leads to:

$$\dot{q}_z = -sin(a)\dot{a} \tag{9}$$

From Equation 9, it shows that a finite $\dot{q}_z$ cannot be achieved when the orientation angle, a, becomes zero. The spindle axis is aligned with *z*-axis in this configuration, and one degree of freedom has been lost. This can be a serious problem because it usually occurs in the middle of the orientation workspace. In the case of horizontal machines, q_x can be expressed in terms of b:

$$\dot{q}_x = cos(b)\dot{b} \tag{10}$$

When b becomes $\pi/2$, a finite $\dot{q}_x$ cannot be obtained. In general, such singularities cannot be avoided in 5-axis serial machine tools. The challenge is to place the points of singularity outside the workplace. The use of C-axes in machine tools is usually the source of the problem. Most 5-axis CNC machine tools in the field today are C-axis machines, and consequently, suffer from this debilitating problem. Note that this problem occurs regardless of whether the axes are stacked together, or are at different locations in the serial chain. The temptation of using a C-axis arises from the fact that the C-axis is a more compact addition to a serial 3-axis or 4-axis machine than an A-axis or a B-axis. Given the inertial and structural stack-up challenges associated with serial machines, which we will discuss later, this compactness of C-axis machines is often the only way to achieve 5-axis motion without reducing machine performance. Kinematic singularities also occur in PKM's, as shown in Figure 2-(b).

3.2. Manipulability

In the robotics community, manipulability at a given configuration is defined as the ability to change the position and orientation of the end-effector in an arbitrary direction [11]. Complete loss of manipulability was defined above to be a kinematic singularity. Even if the singularity position has not been reached, manipulability can be limited in some configurations, and this can be quantitatively measured with one of: 1) minimum eigen value, 2) the condition number or 3) the determinant of the Jacobian†. Manipulability can be visualized with the velocity ellipsoid when the mechanism is not in a singular configuration. The more anisotropic this ellipsoid, the more difficult it is to plan tool paths. Manipulability for position and orientation can be investigated independently with the condition that either orientation or position is fixed [20,21].

---

†. The minimum eigen value of the Jacobian measures the worst-case end-effector velocity. The condition number and the determinant of the Jacobian are measures of isotropy in workspace.

Position manipulability can be investigated with the condition, $\dot{a} = 0$ and $\dot{b} = 0$. We partition the inverse of the Jacobian Matrix into $J^{-1} = [A\ B]$ where A is 5×3 and B is 5×2. $\dot{\Theta}$ can be written as

$$\dot{\Theta} = [A\ B]\ \dot{X} = A\dot{X}_t \text{ where } \dot{X}_t = [\dot{x}\ \dot{y}\ \dot{z}]^T. \tag{11}$$

Let $H = (A^T A)^{-1}$ and V be an orthonomal matrix of H. Multiplying Equation 11 and its transpose leads to:

$$\dot{\Theta}^T \dot{\Theta} = \dot{X}_t^T H^{-1} \dot{X}_t = \dot{X}_{tv}^T D^{-1} \dot{X}_{tv} \tag{12}$$

where D is a diagonal matrix which consists of the eigenvalues of H and $\dot{X}_{tv} = V^T \dot{X}_t$. With the actuator constraint of $\dot{\Theta}^T \dot{\Theta} = 1$ and Equation 12, velocity ellipsoid for position manipulability can be obtained as:

$$\frac{\dot{x}_v^2}{\lambda_{t1}} + \frac{\dot{y}_v^2}{\lambda_{t2}} + \frac{\dot{z}_v^2}{\lambda_{t3}} = 1\ . \tag{13}$$

where λ_{ti} is $D(i, i)$. Equation 13 describes an ellipsoid whose axes lie along the eigen vectors, V.

Orientation manipulability can be investigated with the condition $\dot{x} = 0$, $\dot{y} = 0$ and $\dot{z} = 0$. The procedure is similar to that of position manipulability. Because there are only 2 dof in orientation, 2-dimensional expression is possible. Therefore orientation manipulability can be visualized with velocity ellipses on a 2-dimensional plane.

Figure 3 shows the manipulability of Hexel Corporations's Hexapod in *x-A axis* workspace when *B-* and *C-axis* orientations are zero, *y=0* and *z=0.4m.* The velocity ellipsoids of translation and rotation in Figure 3-a-1 and 3-a-2 show a great deal of anisotropy, which implies that the change of the end-effector position and orientation is not easy in the eigen vector direction associated with the minimum eigen value. In the case of translation, the minimum condition number is 2.76 and maximum condition number is 3.10. Minimum eigen values are almost the same in the *x-A* workspace. The volume of the ellipsoid varies between 0.66 and 0.71. In the case of rotation, the condition number is very high (7.6 ~ 9.59). The minimum eigen values are very small (0.21 ~ 0.22). In summary, the hexapod is a highly non-isotropic machine tool.

This has serious implications on tool paths. If a certain constant cutting speed is desired, as might be the case in high-speed machining, the manufacturing engineer has little option but to pick the worst-case speed everywhere. This means that the actual performance of the machine, in practical terms, may be very poor. The alternative is to go as fast as possible everywhere. This is a difficult path planning problem which is not available in most CAM systems.

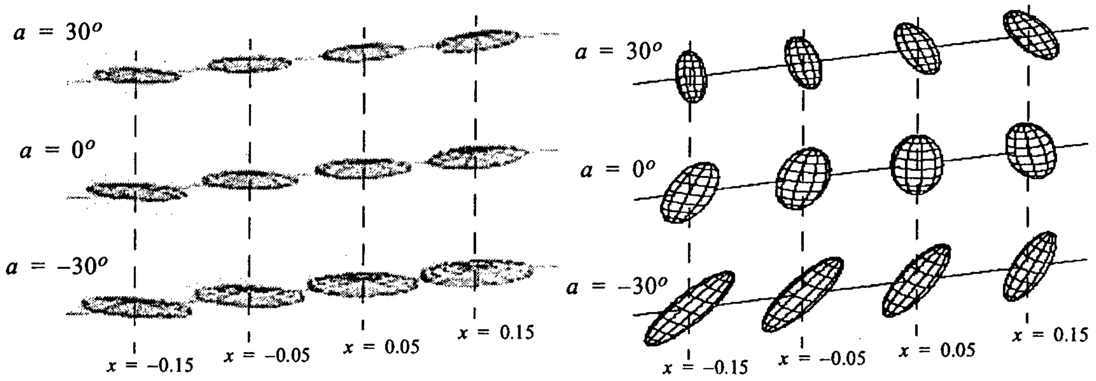
a = 30°
a = 0°
a = −30°
x = −0.15
x = −0.05
x = 0.05
x = 0.15
a = 30°
a = 0°
a = −30°
x = −0.15
x = −0.05
x = 0.05
x = 0.15

a-1) Translation a-2) Rotation

a) Velocity ellipsoids

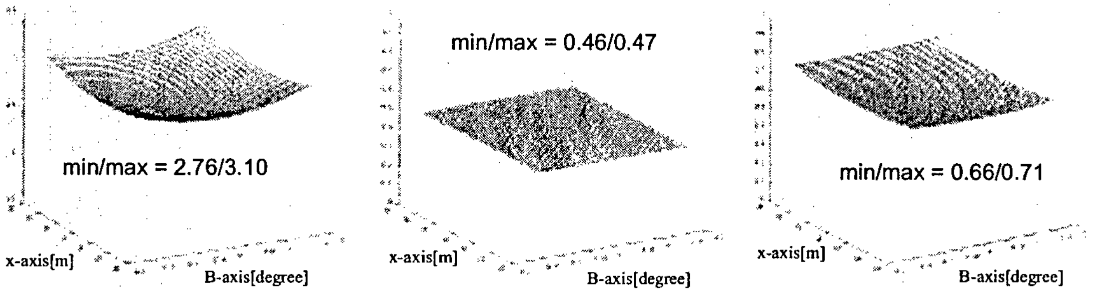

b-1) Condition number b-2) Minimum eigen value b-3) Volume of the ellipsoid

b) Position manipulability

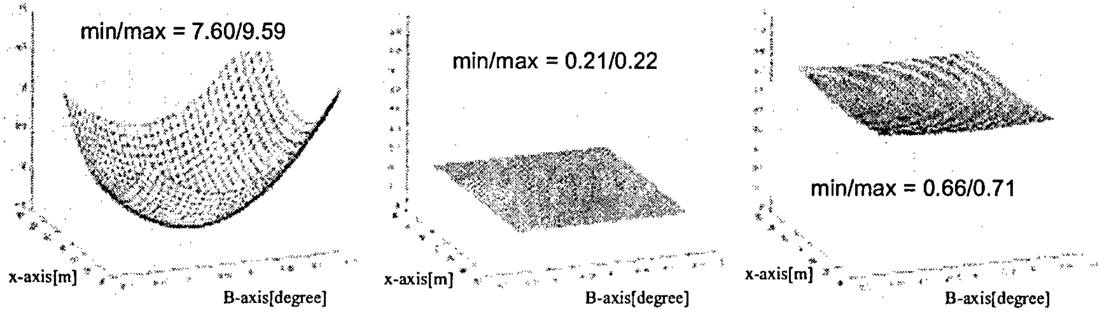

c-1) Condition number c-2) Minimum eigen value c-3) Volume of the ellipsoid

c) Orientation manipulability

Figure 3 Manipulability of the Hexapod

3.3. Reversals in PKM's

When joints in mechanisms reverse their direction of motion, as commonly occurs during circular interpolation, the joint velocity goes to zero. These states have a highly non-linear friction characteristic. Joint-reversals are known to limit the precision of motion of linear axes, and have been studied in the context of linear axes and repetitive control [15]. In serial machines, reversal states are relatively easy to compute—they occur, for example, at the *x*- and the *y*- extremes of a circle in an *x-y* plane for a Cartesian machine. In PKM's, reversals are more critically limiting: *reversals may occur even while the end-effector is moving in a straight line.* This is a severe drawback because the linear datum is one of the most important entities in engineering. In PKM's, reversals can occur at both, active and passive joints. We limit our analysis here to reversals at active joints, although reversals at passive joints too can cause errors. Avoiding reversals while executing typical straight-line trajectories is therefore very important.

3.3.1. Actuator Reversals

Joint velocities can be related with end-effector velocities as shown.

$$\begin{bmatrix}\dot{\theta}_1 & \dot{\theta}_2 & \dots & \dot{\theta}_n\end{bmatrix}^T = J^{-1}\begin{bmatrix}\dot{x} & \dot{y} & \dot{z} & \dot{a} & \dot{b}\end{bmatrix}^T \text{ where } n \geq 5 \tag{14}$$

Each active joint velocity can be expressed as a combination of Jacobian elements and the end-effector velocity. When all the coefficients of a row of the inverse Jacobian are equal to zero, the active joint experiences zero velocity and hence undergoes reversal for any end-effector velocity combinations. We call this extreme case a *reversal-singularity.* Equation 15 relates *i-th* active joint and the end-effector velocity.

$$\dot{\theta}_i = J_{i1}^{-1}\dot{x} + J_{i2}^{-1}\dot{y} + J_{i3}^{-1}\dot{z} + J_{i4}^{-1}\dot{a} + J_{i5}^{-1}\dot{b} \text{ for } i = 1 \dots n \tag{15}$$

A reversal occurs in a configuration in which the joint velocity changes sign. When a reversal-singularity arises, a reversal is almost inescapable. For example, Figure 4-(a) shows the reversal singularities and reversal directions of the Hexel Hexapod when the end-effector moves on *x-y* plane without tilting ($\dot{z} = 0$, $\dot{a} = 0$, $\dot{b} = 0$). The dimensional information of Hexel's Hexapod which was investigated in this paper is presented in Appendix A. When the tangent of the tool path is aligned with any reversal direction as shown in Figure 4-(a), the joint experiences zero velocity. Tool paths for such machines need to be generated very carefully to reduce reversals; however, it is impossible to avoid reversals in most tool paths. Cartesian machine tools have no reversal-singularities if orientation is fixed and more importantly, the reversal directions are parallel with driving axes. This makes it easy to generate reversal free *straight* tool paths.

3.3.2. Reversal-free workspaces in PKM's

It is possible to show that a closed tool path induces actuator reversals with any non-redundant mechanism. However, the number of actuator reversal occurrences depends on the kinematics of the machine. For example, there will be at least 12 reversals in the Hexel's Hexapod while the end-effector is travelling in the closed tool path on the *x-y* plane—however, Cartesian machine tools experience only 4 reversals under same conditions. A rectangular flat surface can be milled on a Cartesian CNC machine tool without reversals (except at the ends of the paths) using zig-zag tool paths. For hexapods, however, reversal characteristics partition space into closed cells; a reversal free path is impossible, for a reasonably sized flat surface, using a hexapod. Figure 5-(a) shows four zig-zag tool paths on a hexapod, and the

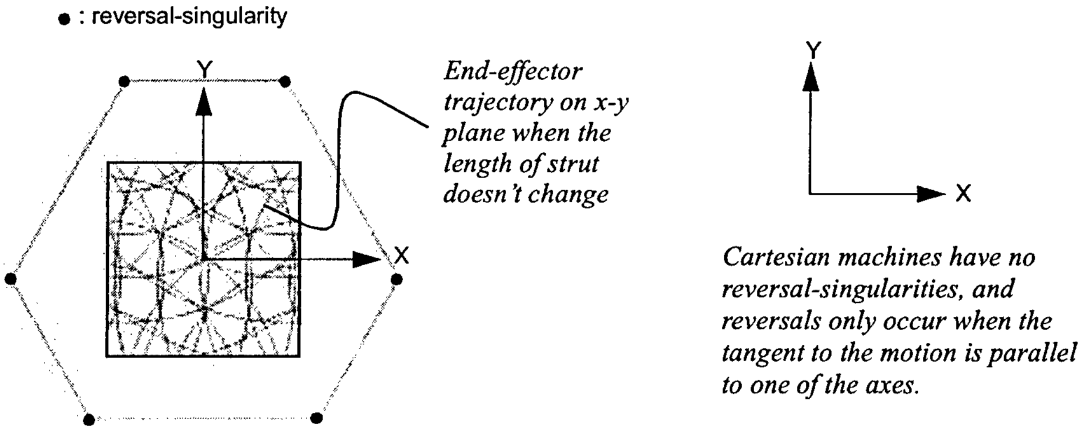

End-effector trajectory on x-y plane when the length of strut doesn't change

Cartesian machines have no reversal-singularities, and reversals only occur when the tangent to the motion is parallel to one of the axes.

(a) Hexapod

(b) Cartesian machine tool

Figure 4 Reversal directions and reversal singularities

reversal lines that they will encounter. Figure 5-(b) shows the reversal-free reachable area for a starting point at the edge of the workspace of the hexapod. These characteristics can be very debilitating, and it is desirable that PKM's are designed in such a way that they reduce reversals.

3.4. The challenges of joint performance in PKM's

The performance of joints poses additional challenges in the design of PKM's. First, because parallel machine tools have extra passive joints (the hexapod has 6 actuators, 6 spherical joints and 6 universal joints), and because each joint adds compliance, error motions and friction to the structure. Furthermore, hexapods, in particular, use spherical joints and telescoping struts. The characteristics, and challenges of designing with several types of joints are compared qualitatively in [22].

Telescoping joints also have other problems. First, they have varying bending stiffness depending on the length to which they are extended. We describe the sources of bending moment later in this section. Consider the situation in which the telescope doubles in length. The the maximum stiffness variation will be about 800% along the *y-axis* because beam bending stiffness is proportional to $1/length^3$. Even though bending a strut may appear a non-sensitive direction, it can be significant for a precision machine tool. In related work, Tlusty *et. al.* [12] compared 2-dof planar parallel structures with fixed-length struts and telescoping-struts for machine tool applications in by considering acceleration capability, workspace, and stiffness variation. They suggest that fixed-length struts have better kinematic characteristics than telescoping struts for machine tool applications.

Second, telescoping joints have the problem of thermal expansion. Fixed-length struts do not have the same problem because there is no frictional heat generated directly in the strut — all the heat is generated at the joints, which are pre-loaded. Thermal expansion in prismatic joints can be compensated, an example, by pre-tensioning the ballscrew. Telescoping joint lengths must, however, be measured and compensated for either directly, using lasers within the screws, or indirectly, with temperature sensors and expansion estimation.†

---

†The Giddings & Lewis Variax, for example, uses laser interferometers within each strut. The placement of lasers is not trivial in general because bending in screws can occlude the laser.

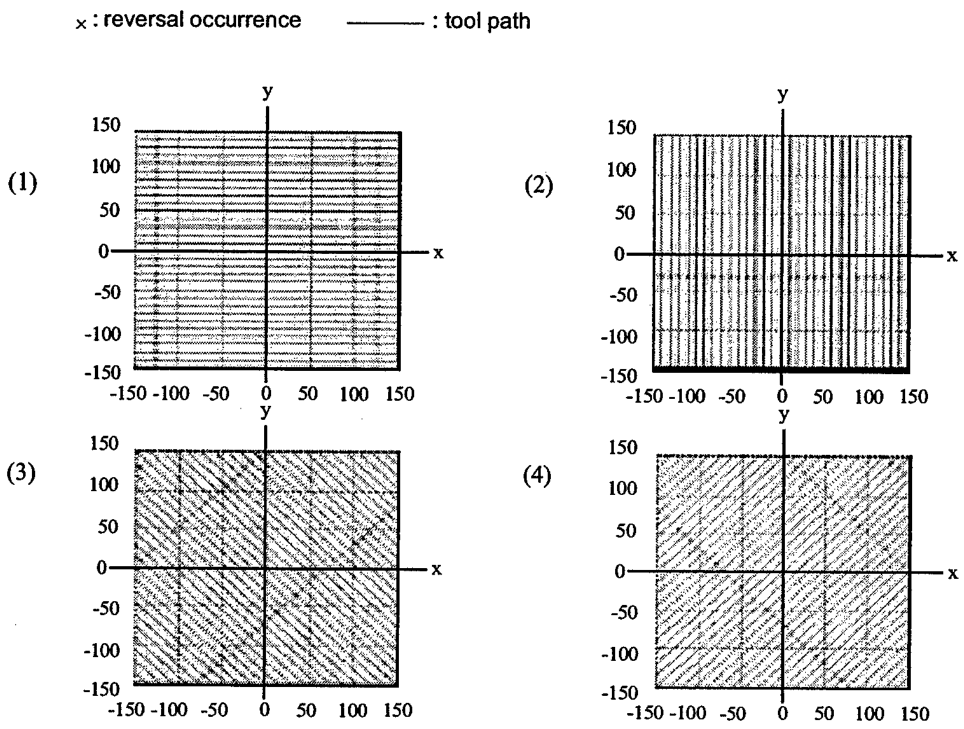

(a) Example of reversal occurrences in the Hexel's Hexapod

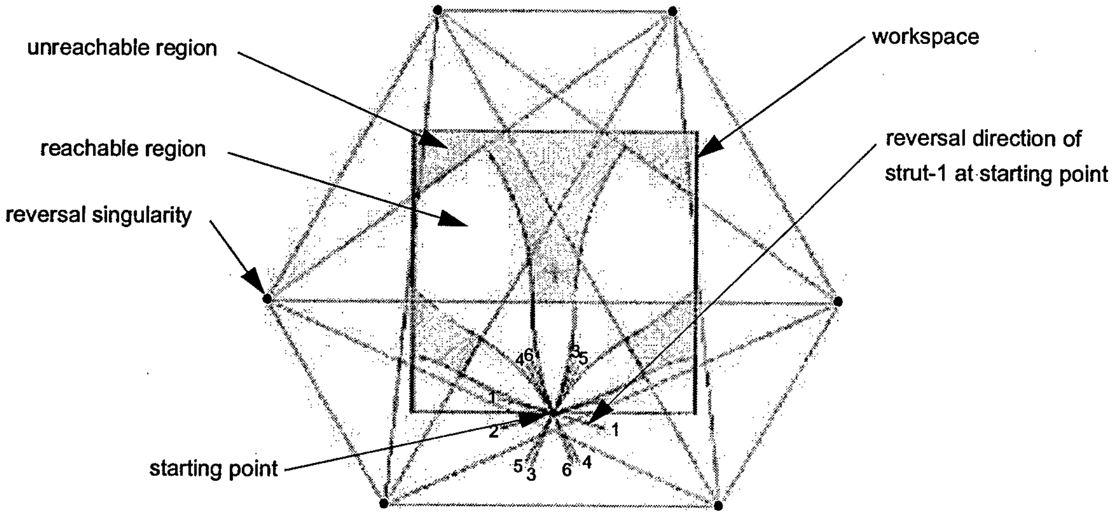
unreachable region
reachable region
reversal singularity
starting point
workspace
reversal direction of strut-1 at starting point
1
2
3
4
5
6

(b) Reachable workspace without reversal occurrences

Figure 5 Example of reversal occurrences in the Hexel's Hexapod

A final class of problems relates to friction. PKM structures are elegant because in the absence of friction, all the forces in the joint are purely compressive or purely tensile, theoretically leaving the telescoping elements, or struts, unburdened by a bending load. This is achieved by the use of screw shafts acting as both actuators and the struts. The struts themselves need support no bending loads in theory because no bending loads are expected in the structure — in the absence of friction, the loads must all be tension or compression, and the struts could be failry slender. Unfortunately, in practice, it is difficult to reduce friction beyond a point in sphere-joints as the state-of-the art stands today. Our experience has shown that the friction in the joints does in fact cause the struts to bend, and this severely affects the stiffness of the hexapod. In the absence of a reaction mass in the moving platform, this loss of stiffness greatly reduces the ability of the machine to reject vibration during the cut.

3.5. Summary

We have pointed out a series of potential problems related to the design of both serial and parallel machines in this section. The challenge is to design a machine tool that meets the following conditions:

- No actuator singularities in the workspace (a PKM problem)
- Well behaved stiffness in the workspace (primarily a PKM problem)
- No kinematic singularities in the workspace (primarily a serial machine problem)
  - This requires that there not be a C-axis
- No reversal-singularities in the *x-y* workspace
- Large reversal free region
- No telescoping joints
- No spherical joints

4. THE HYBRID CONCEPT

The proposed hybrid type 5-axis CNC milling machine incorporates serial as well as parallel elements. We begin by listing the possible configurations and explaining our choice of machine topology.

4.1. Serial/parallel axis distribution

A 5-axis CNC milling machine requires at least 5 actuators. The hexapod actually has six actuators, making it more dextrous than necessary — the sixth axis is degenerate with the axis of symmetry of the rotating tool, and the extra degree of freedom is usually constrained in software. Since the cost of a machine is related to the number of actuators, the design of a hybrid 5-axis machine with 5 actuators offers an immediate potential advantage over the hexapod.

Table 1: Potential hybrid configurations

	Type I	Type II	Type III	Type IV	Type V	Type VI
Serial	5	4	3	2	1	0
Parallel	0	1	2	3	4	5
Total dof	5	5	5	5	5	5

Several combinations of axis distribution for 5-axis CNC milling machines are possible, as shown in Table 1.

Fully serial structures and fully parallel structures belong to Type I and Type VI respectively. The Type II structure is impractical. Therefore Types III, IV, and V are the only real candidate distributions for 5-axes. Furthermore, we eliminate the Type III structure from consideration on the grounds that stacking 3 dof serially is the very challenge we seek to avoid. We are therefore only left with two distributions of parallel and serial axes, Types IV and V.

Parallel structures with less than 6 degrees of freedom need constraining elements which limit the mechanism in the other directions. Type V structures consist of a 1-dof serial structure and a 4-dof parallel structure which needs 2-dof constraints. Such constraining structures must be carefully designed because they may determine the overall stiffness of the parallel structure. A 4-dof parallel structure using a passive constraining leg was introduced in [23]. The overall stiffness depends critically on the passive leg which is intended to resist bending and twisting moments, and the passive leg must be large enough to achieve the required structural stiffness. On the other hand, Type IV structures are attractive because experience with 3-axis machines shows that a serial 2-axis stack-up can be achieved without significantly enlarging the structure. We can therefore limit our search to Type IV structures.

Amongst Type IV structures, where 3 dof are attained with a parallel structure and 2 dof are attained serially, the next question is which of the three translational and two rotational degrees of freedom must be assigned to the serial and parallel components of the machine respectively. One option is to place both the rotational degrees of freedom on the serial mechanism. However, this leads to the problem alluded to in Section 3.1.2: from an engineering point of view, the stack-up of two revolute pairs in a machine tool requires that one of the two be a C-axis, which leads to kinematic singularities. Stacking an A- and a B-axis one on top of another is challenging because each structure is large by itself. We therefore conclude that a workable combination of degrees of freedom, based on our analysis, is a Type IV structure configured as shown in Figure 6 (a).

Given that we intend to avoid higher degree joints, the best way to achieve two translational and one rotational degree of freedom in a parallel mechanism is through a planar mechanism which is also greatly facilitated by the configuration in Figure 7. The machine layout then is reduced to the form shown in Figure 6 (b): the planar mechanism delivers 3 dof in the plane, and the serial mechanism below delivers the two out-of-plane motions. Assuming that this can be engineered, we have achieved a configuration which avoids a 3-axis serial stack-up by using a parallel mechanism, and uses a serial mechanism for a more manageable 2-axis stack-up.

4.2. Configuration Design

The kinematics of 3-dof planar type parallel mechanisms have been well investigated in a number of

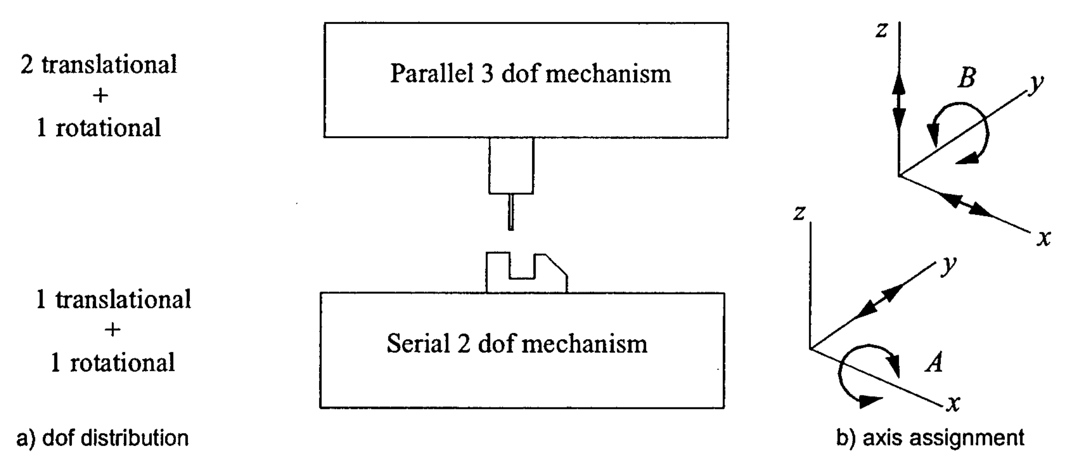
2 translational
+
1 rotational
Parallel 3 dof mechanism
1 translational
+
1 rotational
Serial 2 dof mechanism
z
B
y
x
z
y
A
x
a) dof distribution
b) axis assignment

Figure 6 Type IV structures for MIT-SS-1

papers in the kinematics literature [24,25,26]. Of all the types of planar mechanisms possible, we will only consider those in this paper which use three similar actuators. In other words, we will avoid, for example, driving one degree of freedom with a linear ball-screw and two with rotary actuators. The reason for this decision is modularity. Three broad configurations remain, which are shown in Figure 7.

The 3 types of planar parallel mechanisms shown in Figure 7 are well known, and are referred to as RRR, RPR, and PRR types where the R's and P's represent rotational and prismatic joints respectively. A new consideration now enters the selection process. Cutting forces can be usually considered as disturbances with random characteristics. The reflected force of disturbances on the actuator must be small enough to achieve good tracking performance. RRR mechanisms do not satisfy this consideration for machine tool applications because they need a high gear ratio. Furthermore, they place a large bending moment in the struts in the plane. We further eliminate the RPR structure from our considerations on the grounds that it has a telescoping joint which poses limitations as discussed in Section 3.4.

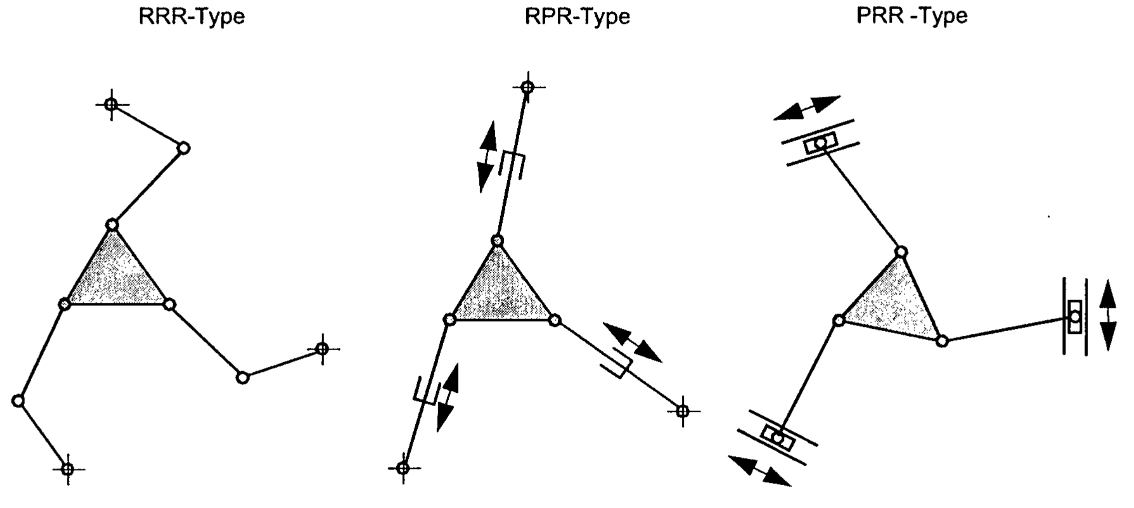
RRR-Type
RPR-Type
PRR -Type

Figure 7 Planar type parallel mechanisms

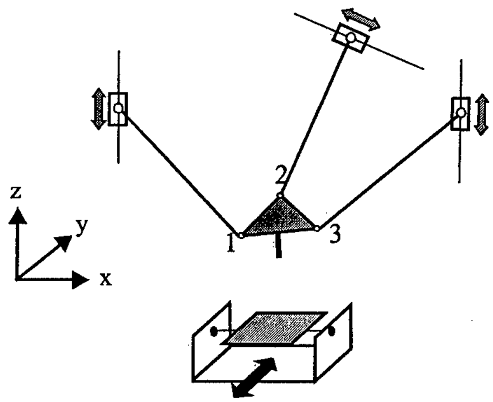

Figure 8 PRR Type Hybrid Structure

Figure 8 shows the remaining configuration, namely the PRR type parallel mechanism, in the context of the axis distribution discussed in the previous section. This PKM has also been pointed out by Ferreira that in a special configuration—when joints 1 and 2 in Figure 8 coincide, the forward kinematics of this mechanism can also be solved in closed form [27]. We do not take advantage of this feature in our machine because the combination of these joints poses other challenges related to bearing design, and to collisions between the struts.

5. The MIT-SS-1 Hybrid Stewart Platform Machine

We have designed a 5-axis CNC milling machine (called the MIT-SS-1) based on the hybrid mechanism described above, with the philosophy of minimizing complexity and error motions by placing the axes

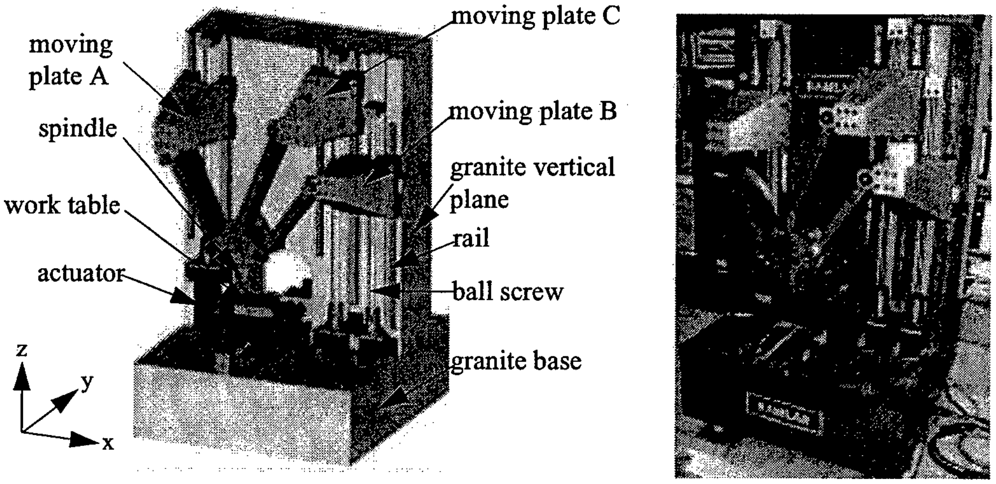
moving plate A
spindle
work table
actuator
moving plate C
moving plate B
granite vertical plane
rail
ball screw
granite base
z
y
x

a) Solid model of MIT-SS-1 b) Prototype

Figure 9 The MIT-SS-1, PRR Type Hybrid CNC Milling Machine

parallel in a plane [28]. The machine is now under construction at MIT. Figure 9 shows a solid model of MIT-SS-1 and a working prototype which is being fabricated. The planar parallel mechanism is installed on the vertical plane and the serial mechanism is installed on the horizontal plane. The MIT-SS-1 has been developed for small parts less than 6.0×10^6 mm^3, and the machine size is very small (0.9m by 1.0m by 1.5m: WxDxH). The machine frame consists of two simple rectangular blocks of solid granite. The granite has good damping and thermal stability. However, Young's modulus of granite is lower than that of materials typically used for machine tool frames, so the sections need to be massive. The frame configuration of the SS-MIT-1 is so simple that the stiffness can be enhanced simply by increasing the thickness of the granite. The vertical plane and the horizontal plane are joined by bolting. The actuators are installed on the frame so that they are not burdened with their own weights. All rails for the parallel structure are installed on the same plane—this reduces the one significant challenge posed by the planar Stewart Platform, namely over-constraint. We will analyze this problem more carefully later. Once one rail is assembled, other rails can be installed precisely, and easily, using the carriage itself as the fixture because all rails on the vertical plane are required to be parallel. In this way, manufacturing errors are minimized.

In the selection of the configuration of this machine, we showed how we could avoid some important kinematic and structural problems. We now examine the inverse kinematics, the stuffiness (and singularities), the workspace, the reversal characteristics and the over-constraint problem of the machine.

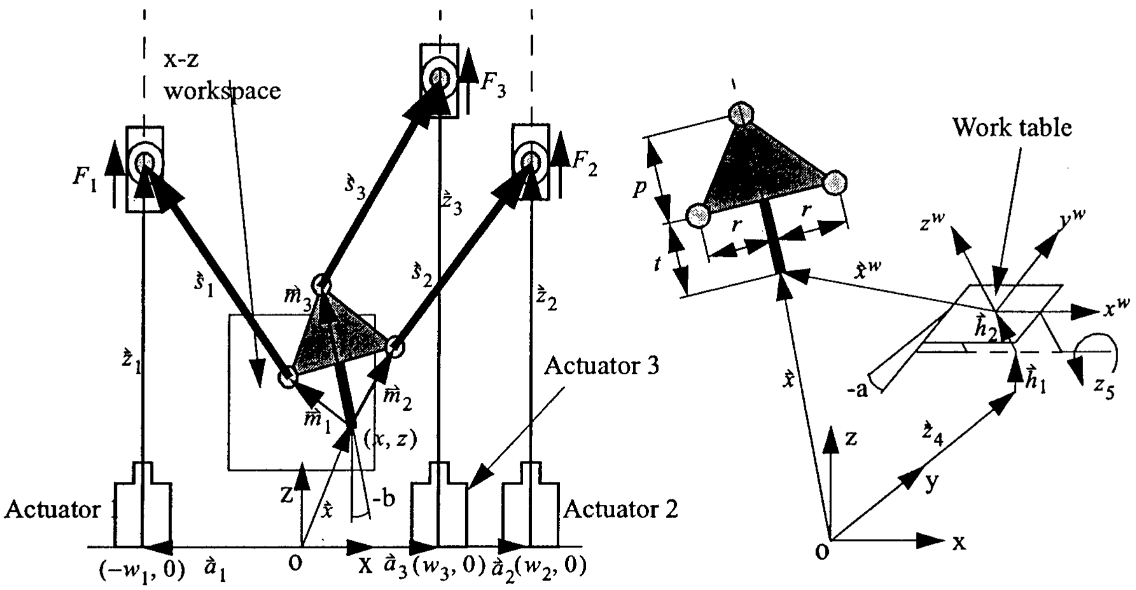

(a) a parallel structure on the vertical plane (b) a serial structure on the horizontal plane

Figure 10 Schematic diagram of MIT-SS-1

5.1. Kinematics

Typically, serial mechanisms have simpler forward kinematics and parallel mechanisms have simpler (but not trivial) inverse kinematics. In the MIT-SS-1, a serial mechanism as well as a parallel mechanism are incorporated. The serial mechanism is elementary for both forward and inverse kinematics. The planar parallel mechanism as shown in Figures 9and 10 has more complex kinematics. We derive the inverse kinematics here for control purposes. A closed form solution to the forward kinematics has not been found. Figure 10 shows the schematic diagram of MIT-SS-1. Let θ_i be the coordinate of the *i-th* actuator. From figure 10-(a), we can derive the vector equations to get the active joint angles.

$$\vec{a}_i + \vec{\theta}_i = \vec{x} + \vec{m}_i + \vec{s}_i \text{ for } i = 1, 2, 3 \tag{16}$$

From Figure 10-(b), the work table coordinate, $\vec{x}^w$, can expressed with a rotation matrix and vector relations.

$$\vec{x}^w = \bar{R}_o(\vec{x} - \vec{h}_1 - \vec{h}_2 - \vec{\theta}_4) \tag{17}$$

where $\vec{x}^w = \begin{bmatrix} x^w \\ y^w \\ z^w \end{bmatrix}$, $\bar{R}_o = \begin{bmatrix} 1 & 0 & 0 \\ 0 & cos(a) & -sin(a) \\ 0 & sin(a) & cos(a) \end{bmatrix}$, $\vec{x} = \begin{bmatrix} x \\ 0 \\ z \end{bmatrix}$, $\vec{h}_1 = \begin{bmatrix} 0 \\ 0 \\ h_1 \end{bmatrix}$, $\vec{h}_2 = \begin{bmatrix} 0 \\ h_2 sin(a) \\ h_2 cos(a) \end{bmatrix}$, and $\vec{z}_4 = \begin{bmatrix} 0 \\ \theta_4 \\ 0 \end{bmatrix}$

From Equation 17, $\vec{x}$ can be written as:

$$\begin{bmatrix} x \\ 0 \\ z \end{bmatrix} = \begin{bmatrix} x^w \\ y^w cos(a) + z^w sin(a) + h_2 sin(a) + \theta_4 \\ -y^w sin(a) + z^w cos(a) + h_1 + h_2 cos(a) \end{bmatrix}. \tag{18}$$

The vectors $\vec{s}_i$, associated with the struts can be derived as following.

$$\vec{s}_1 = \begin{bmatrix} s_{1x} \\ 0 \\ s_{1z} \end{bmatrix} = \begin{bmatrix} -w_1 - x + r cos(b) - t sin(b) \\ 0 \\ z_1 - z - r sin(b) - t cos(b) \end{bmatrix} \tag{19}$$

$$\vec{s}_2 = \begin{bmatrix} s_{2x} \\ 0 \\ s_{2z} \end{bmatrix} = \begin{bmatrix} w_2 - x - r cos(b) - t sin(b) \\ 0 \\ z_2 - z + r sin(b) - t cos(b) \end{bmatrix} \tag{20}$$

$$\vec{s}_3 = \begin{bmatrix} s_{3x} \\ 0 \\ s_{3z} \end{bmatrix} = \begin{bmatrix} w_3 - x - (t+p) sin(b) \\ 0 \\ z_3 - z - (t+p) cos(b) \end{bmatrix}. \tag{21}$$

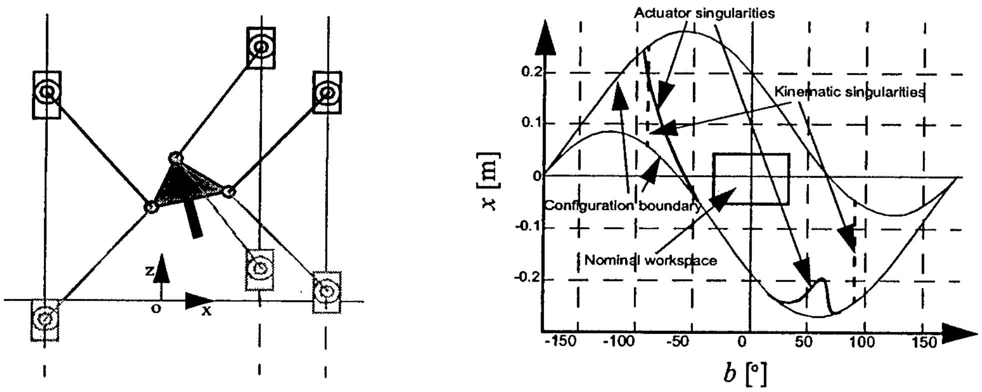

(a) possible configurations

(b) singularity map

Figure 11 Kinematic analysis

The length of each strut, l_i, is fixed, which leads to the inverse kinematics of MIT-SS-1. The actuator coordinates, $\theta_1, \theta_2, \theta_3$, can be expressed in terms of reference coordinates, x, z, b:

$$\theta_1 = z + r\sin(b) + t\cos(b) \pm \sqrt{(l_1^2 - s_{1x}^2)} \tag{22}$$

$$\theta_2 = z - r\sin(b) + t\cos(b) \pm \sqrt{(l_2^2 - s_{2x}^2)} \tag{23}$$

$$\theta_3 = z + (t+p)\cos(b) \pm \sqrt{(l_3^2 - s_{3x}^2)} \tag{24}$$

Equations 22, 23, and 24 show that there are two roots for each actuator, which implies that a total of eight possible configurations of struts exists for each desired tool position. Figure 11-(a) shows all possible configurations for each strut. All the moving plates must be higher than the end-effector to avoid collision with the mechanical components which are installed on the horizontal plane.

The actuator coordinate, θ_4, along the y axis can be obtained by using Equation 18. The actuator coordinate θ_5 is equal to the table orientation, $-a$ as follows:

$$\theta_4 = -y^w\cos(a) - z^w\sin(a) - h_2\sin(a) \tag{25}$$

$$\theta_5 = -a \tag{26}$$

Now all actuator coordinates can be expressed in terms of table coordinates. When the table coordinates are given, actuator coordinates can be easily obtained with from Equations 22~26. Differentiating these equations with respect to time gives us the inverse Jacobian as shown below. Details are presented in Appendix B.

$$\begin{bmatrix}\dot{\theta}_1 & \dot{\theta}_2 & \dot{\theta}_3 & \dot{\theta}_4 & \dot{\theta}_5\end{bmatrix}^T = J^{-1}\begin{bmatrix}\dot{x}^w & \dot{y}^w & \dot{z}^w & \dot{a} & \dot{b}\end{bmatrix}^T \tag{27}$$

Actuator and kinematic singularities of the MIT-SS-1 can be investigated by setting the determinant of the Jacobian and its inverse to zero respectively:

$$|J| = 0 \tag{28}$$

$$|J^{-1}| = 0 \tag{29}$$

Figure 11-(b) shows the singularity map of the MIT-SS-1 on the *x-B* space. Kinematic singularities occur when b is equal to $\pm 90^0$, for any value of x. Solid lines in Figure 11-(b) show the actuator singularities. When the end-effector is at the solid line, the three extension lines of the struts meet at one point and the structure cannot resist a force; this is called a torque singularity. The nominal work-space is described as a shaded rectangular box. From the figure, we know that the workspace does not include a singularity. However, the structure loses stiffness nearer the singularity points, as discussed below.

5.2. Stiffness Analysis

We limit our attention to the parallel structure because it is the more compliant of the two structures. The overall stiffness of the machine structure depends most on the joint stuffiness because joints are usually the most compliant elements in these machines. There are several engineering methods for increasing stiffness, such as using a pre-load, and using roller bearings instead of ball bearings. We used a linear motion system with angular contact bearings in the prismatic joints and tapered roller bearings in the rotational joints. The stiffness along the x and z directions are investigated by studying the Jacobian derived in Equation 27 and the machine element stiffness. There are tapered roller bearings at each end of the strut. The radial deflection of a preloaded roller bearing is proportional to the $(load)^{0.9}$ [29]. For simplicity, we assume that the deflection and load-relation is linear. Therefore we can consider the roller bearings as linear springs. Let the bearing stiffness at the end-effector side be k_{se}, the bearing stiffness of the moving plate side be k_{sm}, and the stiffness of struts be k_{st}. The struts are intended to resist only compression or extension forces in the plane (although they will be subject out-of-plane loads). Since all the bearings are linked serially, the overall stiffness of i-th strut, k_i, can be written as:

$$1/k_i = 1/k_{se} + 1/k_{sm} + 1/k_{st} \tag{30}$$

The overall structural stiffness of the system can be shown to be $J^{-T}K_{st}J^{-1}$ where K_{st} is a diagonal matrix with elements k_i, $K_{st}(i, i) = k_i$. The displacement vector $\vec{d}_1$ for the *x, z* and *B-axis* can be derived using the overall structural stiffness and applied external load $\vec{F}_{ext}$.

$$\vec{d}_1 = \begin{bmatrix}\delta_{1x} & \delta_{1z} & \delta_{1b}\end{bmatrix}^T = K_{st}^{-1}\vec{F}_{ext} \tag{31}$$

We assume that control with position feedback from the moving plate position is ideal, which means that the stiffness of linear guide systems is infinite and the moving plates are fixed along the z direction. We need to introduce a new Jacobian with respect to w_1, w_2, and w_3, where w_1, w_2, w_3 are the distance between the origin and the prismatic joints, because moving plates can deflect along the x direction also. Let the stiffness of the linear guide systems be k_{tr} and new Jacobian be J_{tr}. The displacements of end-

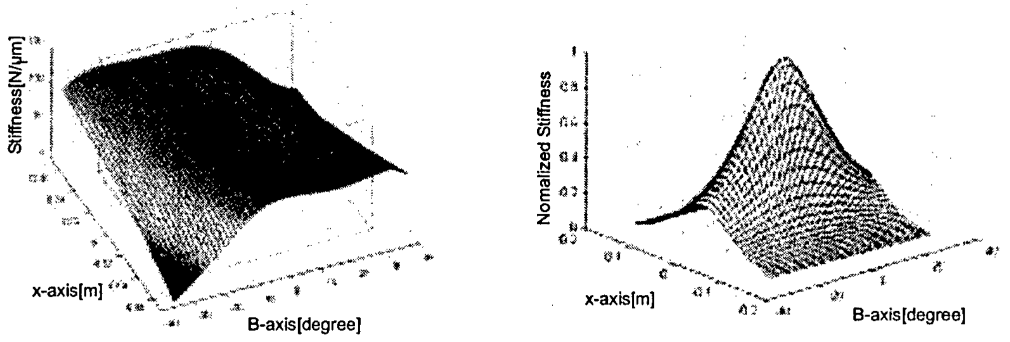

a) MIT-SS-1 b) Hexapod

Figure 12 Stiffness map of the parallel structure

effector, $\vec{d}_2$, caused by the moving plate displacement is

$$\vec{d}_2 = \begin{bmatrix} \delta_{2x} & \delta_{2z} & \delta_{2b} \end{bmatrix}^T = K_{tr}^{-1}\vec{F}_{ext} . \tag{32}$$

We can investigated the stiffness characteristic of the parallel structure with Equations 31 and Equation 32. Figure 12-(a) shows the stiffness the *x-B* workspace. The stiffness map is quite flat in the middle of the workspace; however as the end-effector approaches the lower left corner and the upper right corner, the stiffness drops rapidly because the configuration of the parallel structure is getting closer to an actuator singularity. Figure 12-(b) shows the stiffness map of the Hexel Hexapod at the level of *z=0.4m*. The stiffness variations of the Hexapod are very much greater, and the stiffness drops far more rapidly as the end-effector moves away from the middle of the workspace. In other words, the fact that we use a

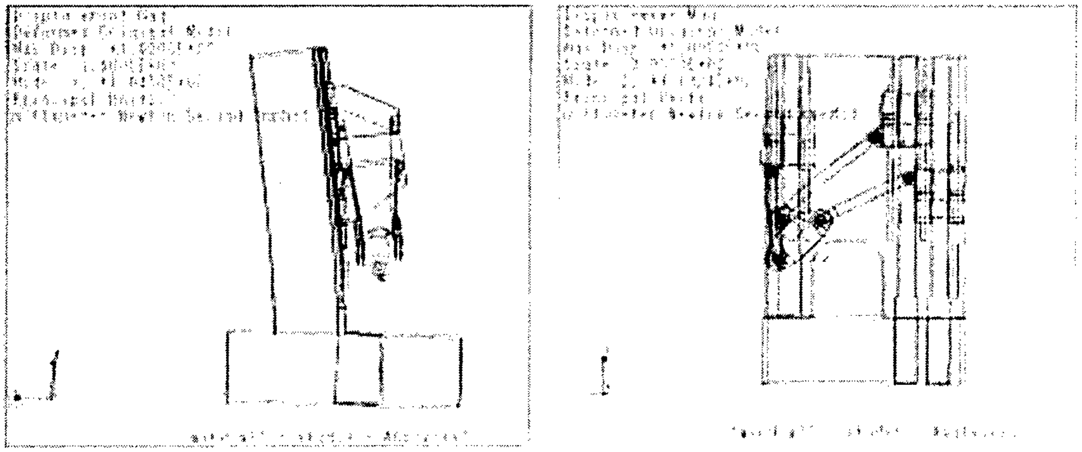

1st mode 2nd mode

Figure 13 Modal analysis

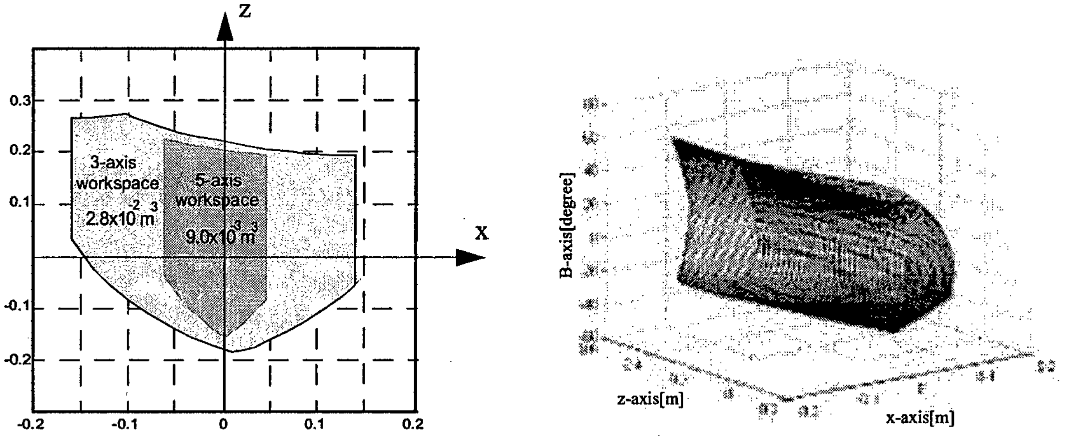

(a) workspace on x-z plane

(a) workspace in x-z-B

Figure 14 Workspace of MIT-SS-1

lower order parallel mechanism makes the behavior of our machine more constant. However, even in our case, we must select the workspace to avoid the more severely compromised portions of the configuration space.

We investigated the stiffness of the machine along the y direction and computed the modal stiffness in several postures of the end-effector using finite element analysis. The results show that the stiffness along y-axis is about $35.0N/\mu m$ and the 1st mode frequency is $104.5Hz$. Variation in the angular postures does not affect the stiffness very much because the 1st mode shape depends on the vertical-plane stiffness as shown in Figure 13-(a). We can achieve a higher modal frequency rather easily by increasing the thickness of the vertical plane. The 2nd mode, which is dominated by strut bearing compliance, is $113.2Hz$. This is much higher than one would encounter with conventional machine tools, where the typical value is in the range of 30-50 Hz.

5.3. Workspace

Parallel mechanisms usually have limited orientation space because singular configurations are closely related with end-effector tilting. We assigned the greater stroke, $\pm 100^o$, for the serial structure and the smaller stroke, $\pm 30^o$, to the parallel structure.

We can examine the workspace of MIT-SS-1 by considering axis travel limitations. The rotational axis and the translational axis in serial structures don't affect the other axis travelling limits. On the other hand, the rotational axis and the translational axis in the parallel structure *do* affect the other axis travel limits. We are therefore interested in the workspace of the parallel structure installed on the vertical plane. Figure 14-(a) shows the x-z workspace with/without end-effector tilting, and Figure 14-(b) shows the workspace in several end-effector tilted positions (the tilt degree corresponds to the vertical axis). As the orientation, b, approaches $80^o/-60^o$, the $x-z$ workspace decreases because of collision between struts, the end-effector and mechanical stops.

When we compute the workspace while considering the tilting of the B axis, we refer to it as the 5-axis workspace. When the end-effector is not tilted, we will refer to the extent of the workspace as the 3-axis

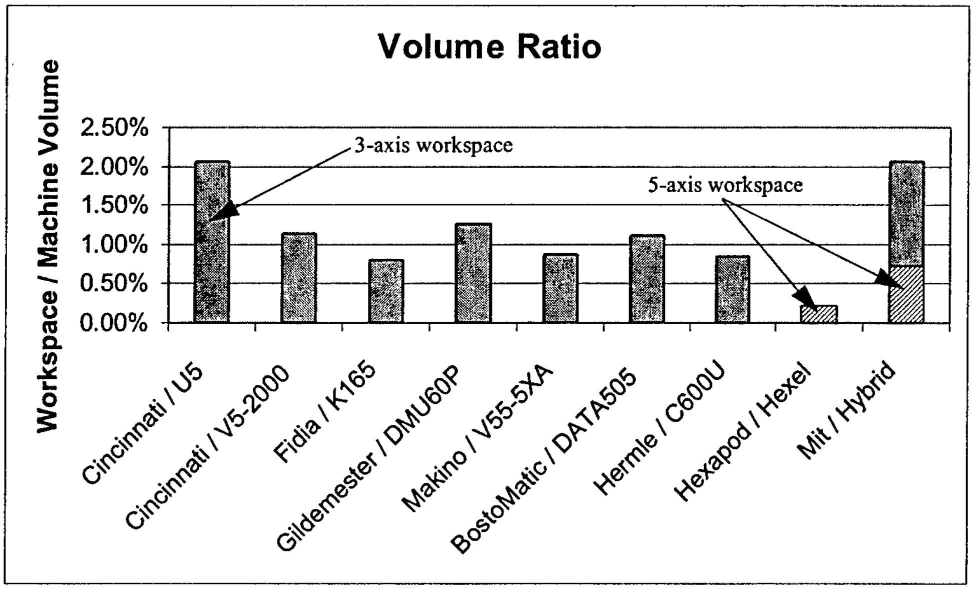

Table 2: Volume ratio between workspace and machine volume

workspace. The 5-axis workspace is shown in Figure 14-(a), and its area is, as expected, smaller than 3-axis workspace. Since machine tool vendors typically supply information regarding only the travel length of each axis, we compared the volume ratio of MIT-SS-1 with that of commercial 5-axis CNC milling machines based on the 3-axis workspace. The term "volume ratio" here represents the ratio of the workspace volume to the machine volume. Table 2 shows that commercial 5-axis CNC milling machines have a volume ratio of 1%. In the case the Cincinnati U5, which is a gantry type serial machine with a fixed table, and the whole structure can move along the $x-axis$ up to 4.0 m. If the $x-axis$ travelling length is increased, the volume ratio is improved. This type of machine is applicable to large workpiece applications. The volume ratio of the MIT-SS-1 is about 2.1%, and is almost identical with that of machine "U5". After the addition of ancillary equipment such as an automatic tool changer (ATC) and coolant delivery systems, we expect the volume ratio of our machine to be around 1.5%.

5.4. Manipulability

MIT-SS-1 consists of 4 translational actuators and 1 rotational actuator. We investigate only the position manipulability because the rotational axis (A-axis) has an independent driving mechanism, the velocity of which can be adjusted easily by changing the gear ratio. Figure 15 shows the manipulability of the MIT-SS-1. Velocity ellipsoids in $x-B$ workspace are shown in Figure 15-a. Quantitative measures are shown in Figure 15-b, 15-c, and 15-d. The condition number is between 1.74 and 2.71; this range is lower than the Hexapod. However, as the end-effector is gets close to $x = -0.06, b = -30^o$ or $x = 0.04, b = 30^o$, the condition number increases rapidly and the volume of the velocity ellipsoid and the minimum eigenvalue goes down rapidly. The results imply that MIT-SS-1 loses manipulability when the strut ends (end-effector side) move away from the middle of the workspace.

5.5. Reversals in plane

Analysis of reversal characteristics on the *x-y* plane reveals that the hybrid configuration does not have

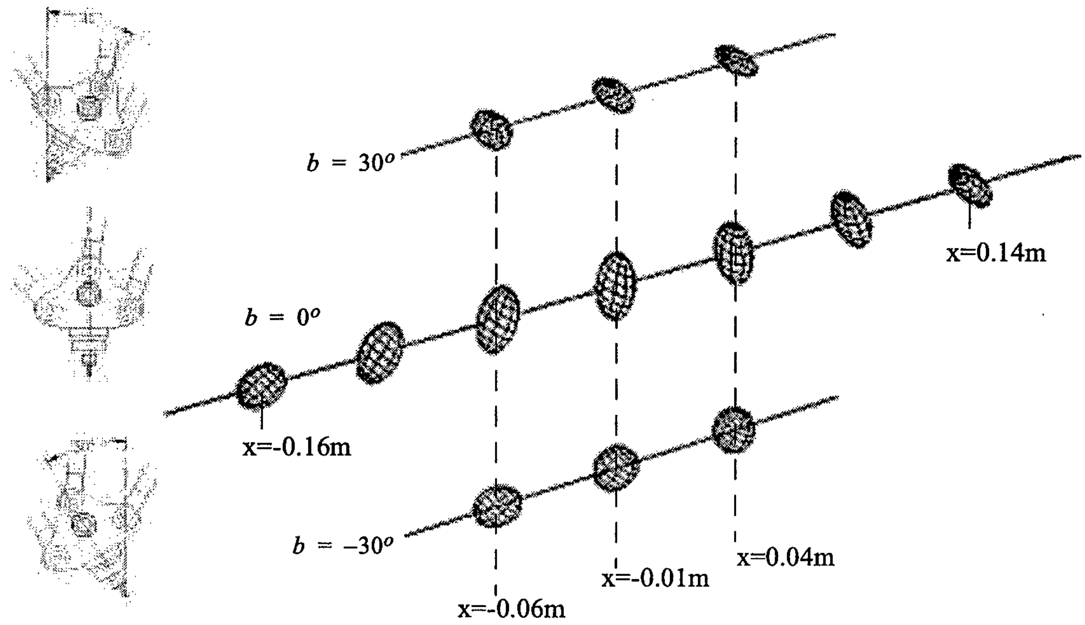
b = 30°
b = 0°
b = −30°
x=-0.16m
x=0.14m
x=-0.06m
x=-0.01m
x=0.04m

a) Velocity ellipsoids of MIT-SS-1

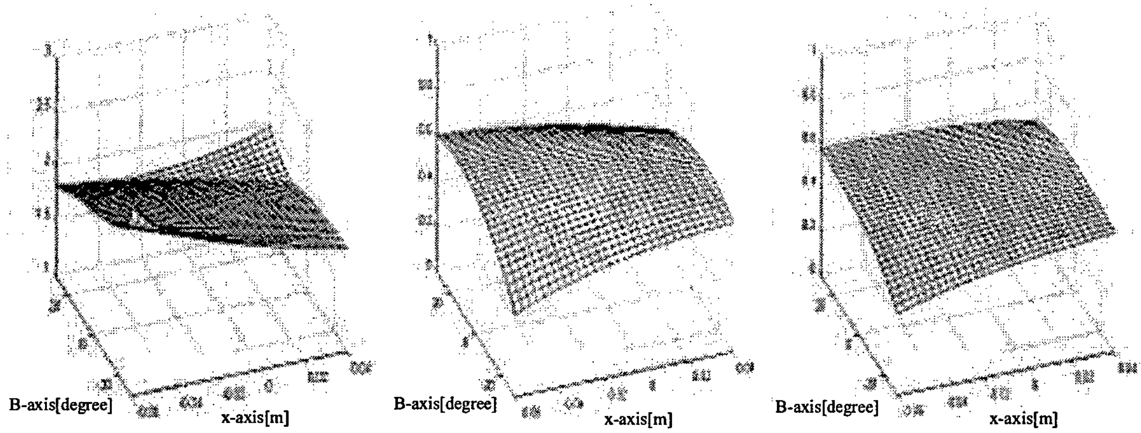

Min =1.74

Max=2.71

b) Condition number

Min =0.36

Max=0.64

c) Volume of the ellipsoid

Min =0.37

Max=0.58

d) Minimum eigenvalue

Figure 15 Position manipulability of MIT-SS-1

reversal problems within the workspace. For the case of a 3-dof planar-type parallel mechanism in which all prismatic joints are aligned with the z-axis, the reversal directions are same with the Cartesian machine tool and the reversal-singularities occur as straight lines as shown in Figure 16. Therefore, the reversal characteristics are effectively the same as those of a Cartesian machine tool. The reversals of a tool path can be easily checked, and reversal-free tool paths exist for any plane.

5.6. Structural over-constraint

An elegant aspect of hexapods is that they are perfectly constrained: six degrees of freedom are determined by six actuators, and assembly involves no over-constraint. The one serious disadvantage of planar PKM of the type proposed here is that they are fundamentally over-constrained structures. From a practical point of view it is impossible to achieve perfect parallelism between three rotational axes, and between prismatic joints. Only if the misalignments are small enough that the bearing and strut compliances can absorb them will the mechanism will work as expected. What these acceptable manufacturing tolerances are depends on two factors: 1) the tolerances we seek from the machine tool, and 2) the allowable load limits of the structural elements when they are forced into an over-constrained assembly. In our machine, the second factor dominates. An important feature of the MIT-SS-1 is the fact that all three prismatic joints have been designed to lie on a single ground surface. This greatly reduces the tolerance stack-up and limits the extent of the over-constraint problem. Figure 17 shows the evolution of the machine topology in response to these manufacturing concerns.

Joint bearings with rolling elements are usually the most compliant structural elements and have low allowable load limits because the rolling elements fail easily under heavy loads. Examples of recommended load limits and compliances of a deep groove ball bearing and a tapered roller bearing are available in [29,30]. Struts also have compliances. The struts can be modeled as rigid solids with springs as shown in Figure 18. The real joint positions on each strut are determined by assuming that the assembly is at the extreme of its manufacturing tolerance. The end-effector must be in equilibrium after assembly. The end-effector is much stiffer than the strut and the bearing assembly, and it can be considered a rigid solid because it consists of one solid steel body. If the equilibrium position of the end-effector can be determined, we can calculate the forces applied to the joints. The values of these forces will tell us if the over-constraint is acceptable. The remainder of this section will show how to compute

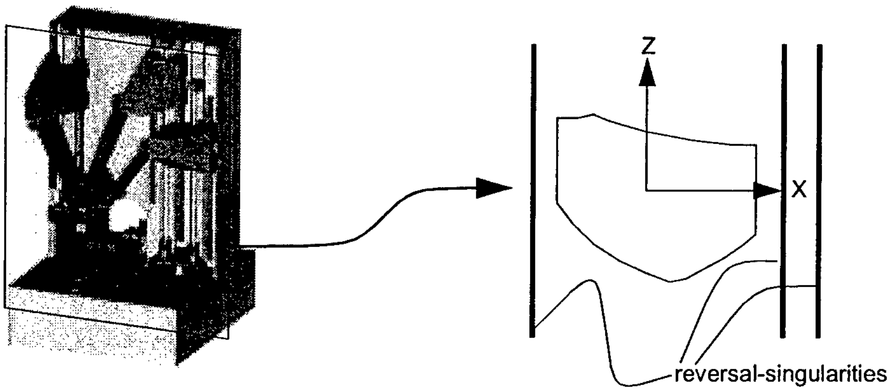

The MIT-SS-1 has reversal-singularity lines outside the workspace. Within the workspace, all reversals occur when the tangent to the path is parallel to the x and the y axes.

Figure 16 Reversal characteristics of MIT-SS-1

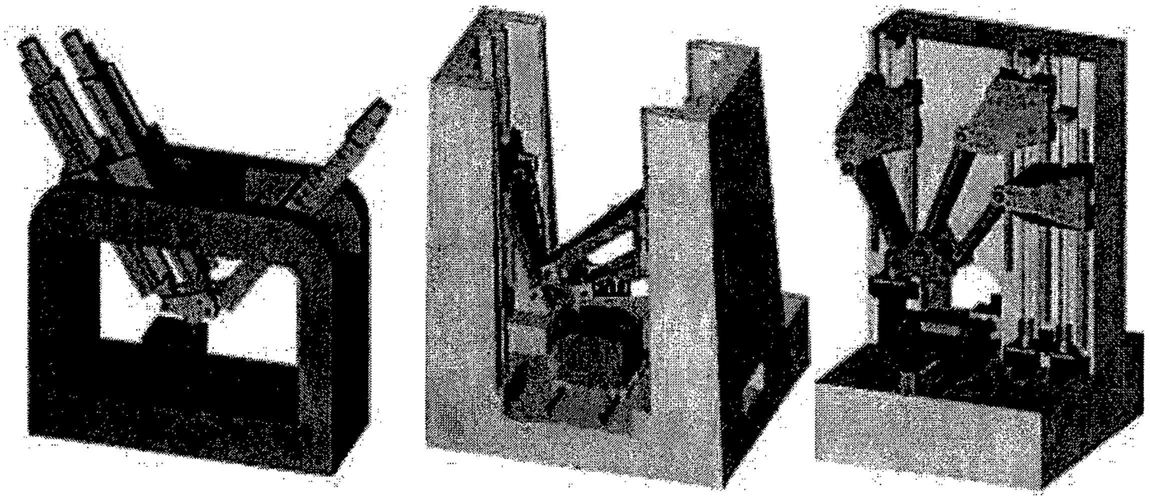

a) Preliminary concept *b) Reduced stack-up* *c) Reduced stack-up*

The design (a) was the first concept with no manufacturing considerations. The design (b) attempted to reduce the misalignments between two of the three prismatic joints by placing them on the same datum. The design (c) all three linear guides on the same plane, reducing stack-up further and in particular, overcomes the over-constraint problem.

Figure 17 Evolution of the MIT-SS-1 to reduce misalignment errors: design for manufacture

the equilibrium position and the required assembly forces at the joints because the system is not statically determinate.

Let the ideal joint positions of the moving plate be D_i, and its equilibrium positions after the assembly be R_i. Figure 19 shows the end-effector displacements due to manufacturing errors. Equilibrium position, R_i, can be obtained from D_i if displacement vector, $\hat{u}_i$, is obtained. We need 3 translational and 3 rotational parameters to describe the end-effector because a rigid body has 6-dof in space. Let us attach a body-fixed coordinate to joint-1. Then the end-effector can be described with the translation of the joint-1 position, $\hat{u}_1$, and the rotation, $\theta\hat{w}$ where $\hat{w}$ is the unit vector along the rotation axis. Rotation matrix R_o, can be expressed as [11]:

$$R_o = e^{\hat{w}\theta} = \begin{bmatrix} 1 - v_\theta(w_y^2 + w_z^2) & w_x w_y v_\theta - w_z s_\theta & w_x w_z v_\theta + w_y s_\theta \\ w_x w_y v_\theta + w_z s_\theta & 1 - v_\theta(w_x^2 + w_z^2) & w_y w_z v_\theta - w_x s_\theta \\ w_x w_z v_\theta - w_y s_\theta & w_y w_z v_\theta + w_x s_\theta & 1 - v_\theta(w_x^2 + w_y^2) \end{bmatrix} . \tag{33}$$

where $v_\theta = 1 - cos(\theta)$ and $s_\theta = sin(\theta)$. Typical manufacturing errors with modern CNC machines are well under 30 µm. We can assume that the amount of rotation, θ, is small enough that $v_\theta \cong 0, s_\theta \cong \theta$. The rotation matrix can be simplified in the following form:

$$R_o = I + \begin{bmatrix} 0 & -w_z\theta & w_y\theta \\ w_z\theta & 0 & -w_x\theta \\ -w_y\theta & w_x\theta & 0 \end{bmatrix} = I + \begin{bmatrix} 0 & -\theta_z & \theta_y \\ \theta_z & 0 & -\theta_x \\ -\theta_y & \theta_x & 0 \end{bmatrix} = I + \hat{\theta} \tag{34}$$

The displacement vector, $\vec{u}_i$, of the joints can be obtained using $\hat{\theta}$:

$$\vec{u}_i = \vec{u}_1 + \theta\vec{w} \times \vec{p}_i = \vec{u}_1 + \hat{\theta}\vec{p}_i \tag{35}$$

The spring deformation vector, $\vec{q}_i$, can be written as:

$$\vec{q}_i = \vec{u}_i - \vec{e}_i = \vec{u}_1 + \hat{\theta}\vec{p}_i - \vec{e}_i\,. \tag{36}$$

Potential energy in the springs can be obtained by using $\vec{q}_i$:

$$V = \Sigma\frac{1}{2}\vec{q}_i^T\overline{K}_i\vec{q}_i = \Sigma\frac{1}{2}[\vec{u}_i - \vec{e}_i]^T\overline{K}_i[\vec{u}_i - \vec{e}_i] = \Sigma\frac{1}{2}[\vec{u}_i^T\overline{K}_i\vec{u}_i + \vec{e}_i^T\overline{K}_i\vec{e}_i - 2\vec{u}_i^T\overline{K}_i\vec{e}_i] \tag{37}$$

where $\overline{K}_i = Diag(k_{ix}, k_{iy}, k_{iz})$.

We apply the virtual work theorem for this static system: $F_{ext}\delta e = \delta V$.

$$\delta V = \Sigma\delta\vec{q}_i^T\overline{K}_i\vec{q}_i = \Sigma[\delta\vec{u}_1 + \delta\hat{\theta}\vec{p}_i]^T\overline{K}_i\vec{q}_i = \Sigma\delta\vec{u}_1^T\overline{K}_i\vec{q}_i + \Sigma[\delta\hat{\theta}\vec{p}_i]^T\overline{K}_i\vec{q}_i \tag{38}$$

where $\delta\vec{q}_i = \delta\vec{u}_1 + \delta\hat{\theta}\vec{p}_i + \hat{\theta}\delta\vec{p}_i - \delta\vec{e}_i = \delta\vec{u}_1 + \delta\hat{\theta}\vec{p}_i$.

There is no work done by the surroundings because no external forces exist. δV should be equal to zero.

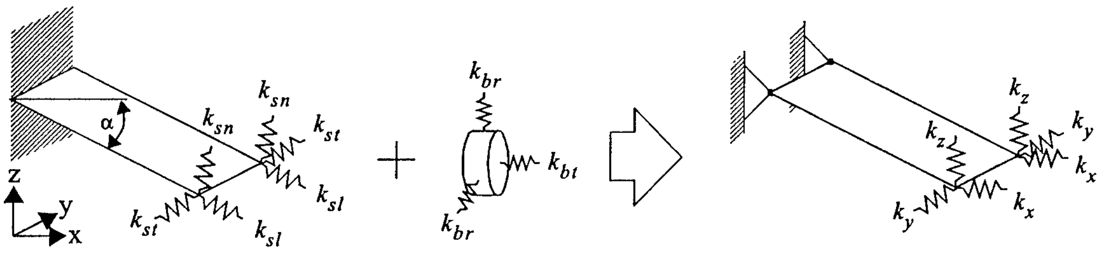

strut compliance

bearing compliance

$$1/k_y = 1/k_{st} + 1/k_{bt}$$
$$1/k_x = 1/(k_{sl}c_\alpha + k_{sn}s_\alpha) + 1/k_{br}$$
$$1/k_z = 1/(k_{sl}s_\alpha + k_{sn}c_\alpha) + 1/k_{br}$$

Figure 18 Model for strut and joint bearings

Equation 39 and Equation 40 below can be derived with the condition that $\delta\bar{u}_1^T$ and $\delta\bar{\theta}$ are arbitrary.

$$\Sigma\bar{K}_i\vec{e}_i = \Sigma\bar{K}_i\vec{u}_1 + \Sigma\bar{K}_i\bar{E}_x\vec{p}_i\theta_x + \Sigma\bar{K}_i\bar{E}_y\vec{p}_i\theta_y + \Sigma\bar{K}_i\bar{E}_z\vec{p}_i\theta_z \qquad (39)$$

where $\bar{E}_x = \begin{bmatrix} 0 & 0 & 0 \\ 0 & 0 & -1 \\ 0 & 1 & 0 \end{bmatrix}$, $\bar{E}_y = \begin{bmatrix} 0 & 0 & 1 \\ 0 & 0 & 0 \\ -1 & 0 & 0 \end{bmatrix}$, and $\bar{E}_z = \begin{bmatrix} 0 & -1 & 0 \\ 1 & 0 & 0 \\ 0 & 0 & 0 \end{bmatrix}$.

$$\Sigma\hat{p}_i\bar{K}_i\vec{e}_i = \Sigma\hat{p}_i\bar{K}_i\vec{p}_1 + \Sigma\hat{p}_i\bar{K}_i\bar{E}_x\vec{p}_i\theta_x + \Sigma\hat{p}_i\bar{K}_i\bar{E}_y\vec{p}_i\theta_y + \Sigma\hat{p}_i\bar{K}_i\bar{E}_z\vec{p}_i\theta_z \qquad (40)$$

where $\hat{p}_i = \begin{bmatrix} 0 & -p_{iz} & p_{iy} \\ p_{iz} & 0 & -p_{ix} \\ -p_{iy} & p_{ix} & 0 \end{bmatrix}$.

Combining Equations 39 and 40 leads to Equation 41.

$$\begin{bmatrix} [\Sigma\bar{K}_i] & [\Sigma\bar{K}_i\bar{E}_x\vec{p}_i] & [\Sigma\bar{K}_i\bar{E}_y\vec{p}_i] & [\Sigma\bar{K}_i\bar{E}_z\vec{p}_i] \\ [\Sigma\hat{p}_i\bar{K}_i] & [\Sigma\hat{p}_i\bar{K}_i\bar{E}_x\vec{p}_i] & [\Sigma\hat{p}_i\bar{K}_i\bar{E}_y\vec{p}_i] & [\Sigma\hat{p}_i\bar{K}_i\bar{E}_z\vec{p}_i] \end{bmatrix} \begin{bmatrix} [\vec{u}_1] \\ \theta_x \\ \theta_y \\ \theta_z \end{bmatrix} = \begin{bmatrix} [\Sigma\bar{K}_i\vec{e}_i] \\ [\Sigma\hat{p}_i\bar{K}_i\vec{e}_i] \end{bmatrix} \qquad (41)$$

With Equation 41 the displacement of the position D_1, $\vec{u}_1$, and the rotation angle, $[\theta_x\ \theta_y\ \theta_z]^T$, can be

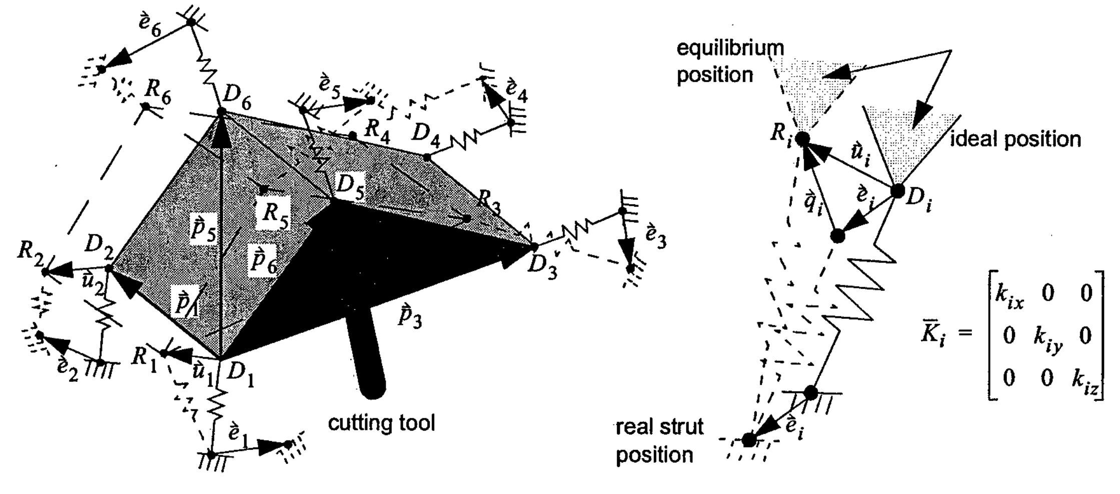
$\vec{e}_6$
R_6
D_6
$\vec{e}_5$
$\vec{e}_4$
R_4
D_4
D_5
R_3
R_5
$\vec{p}_5$
$\vec{p}_6$
$\vec{e}_3$
R_2
D_2
$\vec{u}_2$
D_3
$\vec{p}_1$
$\vec{p}_3$
$\vec{e}_2$
R_1
$\vec{u}_1$
D_1
$\vec{e}_1$
cutting tool
equilibrium position
ideal position
R_i
$\vec{u}_i$
$\vec{q}_i$
$\vec{e}_i$
D_i
$\bar{K}_i = \begin{bmatrix} k_{ix} & 0 & 0 \\ 0 & k_{iy} & 0 \\ 0 & 0 & k_{iz} \end{bmatrix}$
real strut position
$\vec{e}_i$

Figure 19 End-effector displacement by manufacturing errors

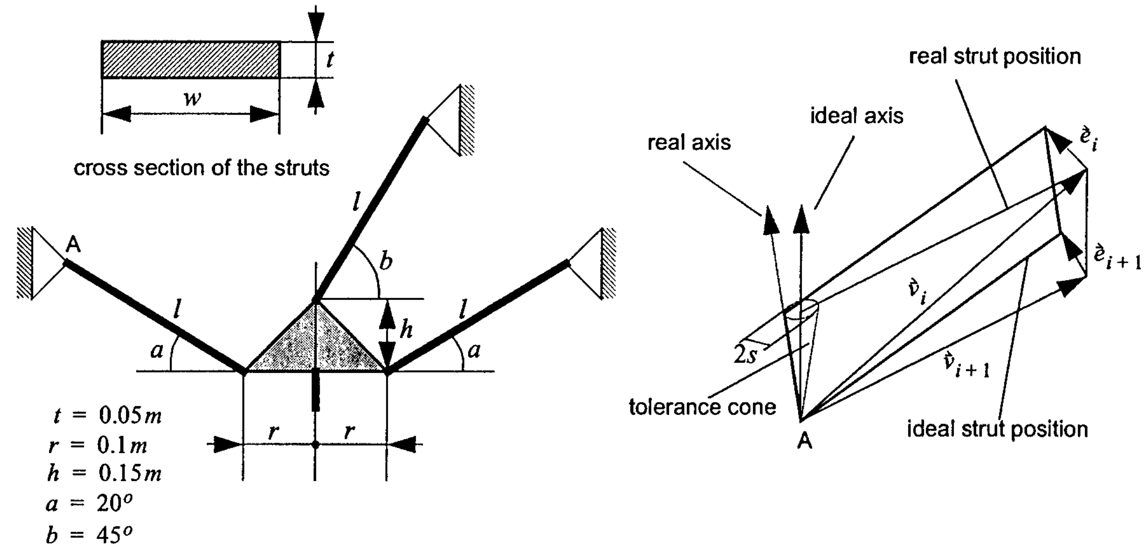
w
t
cross section of the struts
A
l
a
b
h
r
t = 0.05m
r = 0.1m
h = 0.15m
a = 20°
b = 45°
real strut position
ideal axis
real axis
$\hat{e}_i$
$\hat{e}_{i+1}$
$\hat{v}_i$
$\hat{v}_{i+1}$
2s
tolerance cone
A
ideal strut position

(a) structure dimensions (b) strut displacement due to manufacturing error

Figure 20 Schematic diagram of the tested structure

obtained. Now we can derive the spring deformation with Equation 36. And the required assembly forces at each joint places can be obtained with the stiffness matrix and deformation of the joint-i:

$$\begin{bmatrix} F_{ix} \\ F_{iy} \\ F_{iz} \end{bmatrix} = \begin{bmatrix} k_{ix} & 0 & 0 \\ 0 & k_{iy} & 0 \\ 0 & 0 & k_{iz} \end{bmatrix} \begin{bmatrix} q_{ix} \\ q_{iy} \\ q_{iz} \end{bmatrix} . \tag{42}$$

We examined the required assembly forces at each joint location for 3 equal, fixed-length strut planar mechanisms. Figure 20 shows the schematic diagram and the dimensions. We assume that parallelism between ideal rotational axis and real rotational axis is $300\mu m/m$ and that the rotational axis can be *placed randomly on the surface of the tolerance cone.* The width of strut, w, is determined such that it is related to the bending stiffness along the y-direction as shown below:

	l	*w*	*Fr(max) [kN]*	*Fa(max) [kN]*
Case-I	0.5m	0.1m	9.7/4.7/10.0/4.1/10.2/2.9	1.9/1.9/1.8/1.8/1.7/1.7
Case-II	1.0m	0.2m	19.6/7.7/19.8/6.9/18.7/5.8	3.9/3.9/3.7/3.7/3.6/3.6
Case-III	1.5m	0.3m	29.4/10.6/29.5/9.8/27.3/9.2	5.7/5.7/5.6/5.6/5.5/5.5

Table 3: Required assembly forces at each joint for the worst case

$$w = l\left(\frac{4K_y}{Et}\right)^{1/3} . \tag{43}$$

where t is the thickness of the strut. We calculated assembly forces for 3 cases as in Table 3. $F_r(max)$ in the table stands for maximum radial forces and $F_a(max)$ stands for maximum axial forces. There are 6 values of $F_r(max)$ and $F_a(max)$ in each case; the first number is the assembly force at joint-1, the second number the assembly force of joint-2 and so on. The results show that 3-dof planar parallel structures with longer struts need larger assembly forces and the assembly forces increase linearly as the strut length increases. This is because the position errors are linearly dependent on the length of the strut and the stiffness of the strut remains constant. *Required assembly forces of large structures can exceed the permitted load ranges of joint bearings. This implies that planar parallel mechanisms which use radial rolling bearings are not good for large machine tool applications.* On the other hand, these constraints work favorably for small machine tools. For the machine dimensions we have proposed, assembly is possible, and the loads are tolerable.

6. PERFORMANCE TARGETS

The MIT-SS-1 has been designed with the following performance targets in mind:

- Maximum rapid motion speed in work-space: $30 m/min$
- Stiffness: $30 N/\mu m$
- Dynamic performance: $\omega_1 = 70 Hz$
- Acceleration: $2g$

The system will be controlled by an Aerotech UNIDEX 500 motion controller. Several spindles have been sized for the machine but one has not yet been selected. The machine is targeted for high-speed machining of aerospace-type parts.

7. MOVING-BRIDGE 4-AXIS MACHINE

One of the important assets of PKM's is that they can have a "one-sided" configuration. In other words, all the joints can be placed on one ceiling-type platform, which can be moved. When the hexapod first appeared, there was speculation that it could be mounted on a moving gantry or a 2D structure of high stiffness to machine large, 5-axis shapes like boat hulls and aerospace parts. This would correspond to a coarse-fine manipulation strategy common in robotics and precision engineering.

The same strategy can be applied to the MIT-SS-1 as we have described here. The 5-axis machine configuration is easily converted to a 4-axis configuration of almost unlimited length by reducing the serial 2-axis structure to a simple 1-axis stage. Alternatively, the planar PKM in MIT-SS-1 may be attached to a moving bridge. In other papers [31], we have made the argument that most 5-axis tool paths can be reduced, in effect, to 4-axis tool paths. The 5th axis becomes important when the relative angle between the tool and the surface normal must be adjusted to control the physics of the cut. In high-speed situations, this angle must be adjusted to ensure that the cutting load, in terms of feed per tooth, remains constant during the cut. However, in large structures, this is less important, especially during hogging. In these situations, the moving bridge configuration, and the 4-axis reduction of this machine in general, are attractive configurations.

8. CONCLUSIONS

We have investigated the kinematic properties of parallel and serial mechanisms and pointed out several kinematic and structural challenges in the practical deployment of these machines. The hybrid concept uses the advantages of serial and parallel mechanisms, and avoids most of these pitfalls, as we have shown. In particular, the hybrid machine can attain a relatively large workspace without compromising much on stiffness and manipulability, it can be configured in a way to avoid reversals in the workspace, it can be designed with well-understood revolute joints and linear guides, thus avoiding the problems of spherical joints and prismatic joints, and it can be designed with a relatively compact footprint.

We pointed out that a 3-dof planar parallel mechanism with wide struts cannot avoid over-constraints, and is sensitive to manufacturing tolerances. We showed that the effects of these overconstraints can be avoided by placing all the sliding joints on a single plane. However, the effects of these tolerances depend on the size of the structure, so that the hybrid planar mechanism is more applicable to small machine tools and does not scale well with size.

We have designed a small 5-axis CNC milling machine, the MIT-SS-1, which combines a 2-dof serial mechanism and a 3-dof planar type parallel mechanism based on these criteria. The effects of over-constraints are within acceptable ranges and the reversal characteristics of MIT-SS-1 are the same as those of Cartesian machine tools on the x-y plane when there is no end-effector tilting. We can achieve a fairly good volume ratio between workspace and machine volume, low stiffness variation within the workspace, and a low moving inertia. The 1st mode frequency of MIT-SS-1 is high as $104.5Hz$, which implies that MIT-SS-1 has the potential for high-speed machining.

We have demonstrated that hybrid mechanisms are potentially attractive candidates for small 5-axis machine-tool applications. MIT-SS-1 is currently being fabricated, and we will document its performance in a forthcoming paper.

9. ACKNOWLEDGMENTS

Support for this research was provided by Daewoo Corporation, The National Science Foundation under grants DMI 9413936 and DMI 9912558, a grant from the Defense Logistics Agency AQP (#N00014-95-1-5-039).

10. REFERENCES

[1] Tooling and Production Magazine, Putting the Hex(apod) on Machining, Tooling and Production Magazine, September, 1996, pp37-42

[2] B.S. El-Khasawneh and P.M. Ferreira, "On Using Parallel Link Manipulators as Machine Tools," Transactions of NAMRAC XXV, pp 305-310, 1997

[3] B.S. El-Khasawneh and P.M. Ferreira, "The Tetrahedral Tripod," in Parallel Kinematic Machines: Theoretical Aspects and Industrial Requirements, C.R. Boër, L. Molinari-Tosatti, and K.S. Smith, eds. (Springer-Verlag, 1999), pp419-430

[4] M. Hebsacker, T. Treib, O. Zirn and M. Honegger, "Hexaglide 6 DOF and Triaglide 3 DOF Parallel Manipulators," in Parallel Kinematic Machines: Theoretical Aspects and Industrial Requirements, C.R. Boër, L. Molinari-Tosatti, and K.S. Smith, eds. (Springer-Verlag, 1999), pp345-355

[5] F. Pierrot and T. Shibukawa, "From Hexa to HexaM," in Parallel Kinematic Machines: Theoretical Aspects and Industrial Requirements, C.R. Boër, L. Molinari-Tosatti, and K.S. Smith, eds. (Springer-Verlag, 1999), pp357-364

[6] I. Fassi and G.J. Wiens, "Multiaxis Machining: PKMs and Traditional Machining Centers," J. of Manufacturing Process, Vol. 1/No.2, 2000, pp 79-92

[7] Ilian Bonev, http://wwwrobot.gmc.ulaval.ca/~bonev/Bookmarks.html

[8] L. W. Tsai, "Systematic Enumeration of Parallel Manipulators," in Parallel Kinematic Machines: Theoretical Aspects and

Industrial Requirements, C.R. Boër, L. Molinari-Tosatti, and K.S. Smith, eds. (Springer-Verlag, 1999), pp 33-49

[9] G. Pritschow and K-H. Wurst, "Systematic Design of Hexapods and Other Parallel Link Systems," Annals of the CIRP (v46/1, 1997), pp 291-295

[10] Adolf Kargert and Manfred Husty, "Classification of All Self-Motions of The Original Stewart-Gough Platform," Computer-Aided Design, Vol. 30, No. 3,pp. 205-215,1998.

[11] R. Murray, Z. Li and S. Sastry, A Mathematical Introduction to Robotic Manipulation, CRC Press, 1994

[12] J. Tlusty (1), J. Ziegert, S. Ridgeway, "Fundamental Comparison of the Use of Serial and Parallel Kinematics for Machine Tools," Annals of CIRP, Vol. 48, 1999

[13] H.K. Tonshoff and H. Grendel, "A Systematic Comparison of Parallel Kinematics," in Parallel Kinematic Machines: Theoretical Aspects and Industrial Requirements, C.R. Boër, L. Molinari-Tosatti, and K.S. Smith, eds. (Springer-Verlag, 1999), pp295-312

[14] L. Yuan and J. Rastegar, "Optimal integration of smart actuators in parallel and cooperating robots to enhance operating speed and accuracy," Proc. of ASME 2001 Design Engineering Technical Conference, Pittsburgh, PA, September 9-12, 2001

[15] E. D. Tung, "Identification and control of high-speed machine tools," Doctoral thesis in Mechanical Engineering, U.C. Berkeley, 1993.

[16] B. Armstrong-Helouvry, P. Dupont and C. Wit, "A Survey of Models, Analysis Tools and Compensation Methods for the Control of Machines with Friction," Automatica, Vol.30, No. 7, pp1083-1138, 1994

[17] J. K. Salisbury and J. J. Craig, "Articulated Hands: Force Control and Kinematic Issues," The Int. Journal of Robotics Research, Vol. 1, No. 1, Spring 1982, pp4-17

[18] T. Yoshikawa, "Manipulability of Robotic Mechanisms," The Int. Journal of Robotics Research, Vol. 4, No. 2, Summer 1985, pp3-9

[19] R. Martone and B. Roth, "The Effects of Actuation Schemes on the Kinematic Performance of Manipulators," Trans. of ASME, Vol. 119, June 1997, pp212-217

[20] J.W. Kim, C. Park, J. Kim and F.C. Park, "Performance Analysis of Parallel Manipulator Architectures for CNC Machining Applications," MED-Vol.6-2, Manufacturing Science and Technology Vol.2, ASME 1997, pp341-348

[21] K. Kosuge, M. Okuda, H. Kawamata and T. Fukuda, "Input/Output Force Analysis of Parallel Link Manipulators," Proc. of IEEE Int. Conference on Robotics and Automation, 1993, pp714-719

[22] U. Heisel, "Precision Requirements of Hexapod-Machines and Investigation," in Parallel Kinematic Machines: Theoretical Aspects and Industrial Requirements, C.R. Boër, L. Molinari-Tosatti, and K.S. Smith, eds. (Springer-Verlag, 1999), pp131-150

[23] D. Zhang and C. Gosselin, "Kinetostatic Modelling of N-DOF Parallel Mechanisms with a Passive Constraining Leg and Prismatic Actuators." Journal of Mechanical Design, Vol. 123, September 2001.

[24] C. Gosselin and J. Angeles, "The Optimum Kinematic Design of a Planar Three-Degrees-of-Freedom Parallel Manipulator," J. of Mechanisms, Transmissions, and Automation in Design, Vol. 110, March 1988.

[25] J. Sefrioui and C. Gosselin, "Singularity Analysis and Representation of Planar Parallel Manipulators," Robotics and Autonomous Systems, October 1992.

[26] J. Merlet, C. Gosselin and N. Mouly, "Workspace of Planar Parallel Manipulators," Mech. Mach. Theory Vol. 33, No. 1/2, 1998.

[27] P. Ferreira, Personal Conversation. Milan, Italy, September 1999.

[28] Slocum, A. *Precision Machine Design*. Society of Manufacturing Engineers; ISBN: 0872634922. 1992.

[29] Tedric A. Harris, Rolling bearing analysis, 2nd edition, New York: Wiley, 1984.

[30] SKF USA Inc., General Catalog, 1999.

[31] Mahadevan, B., Sarma, S. E. and Marciniak, K. "Collision-Free Finishing Tool Paths from Visibility Data," Accepted for publication in Computer-Aided design. To appear in 2002.

APPENDIX A:

Hexapod information

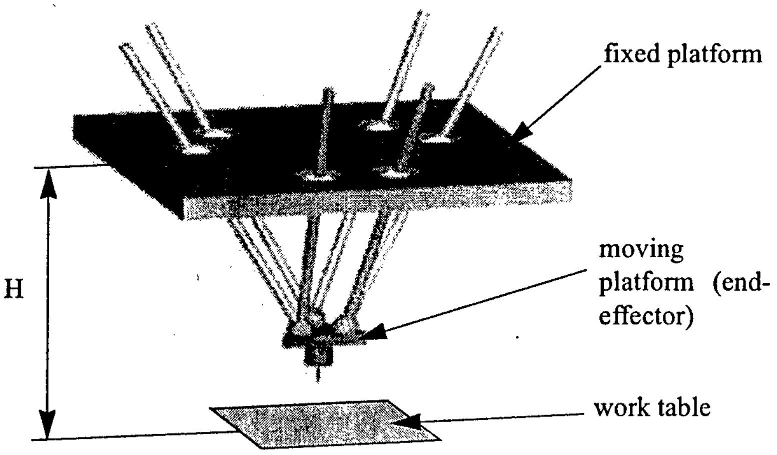
fixed platform
H
moving platform (end-effector)
work table

(a) 6 x 3 type Hexapod

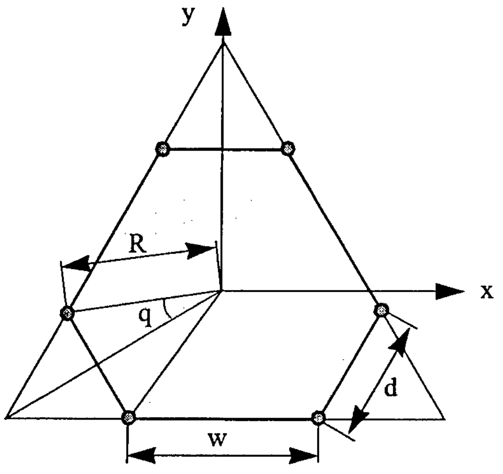

(b) fixed platform

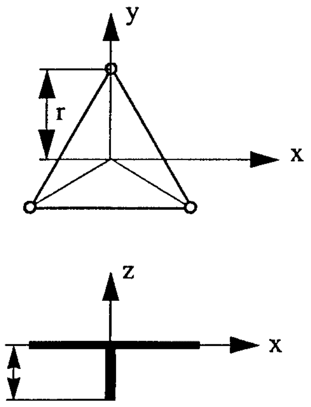

(c) moving platform

Dimension : [m]

w=0.66m r=0.175m
d=0.25m H=1.2m
t=0.2m

APPENDIX B:

Jacobian of MIT-SS-1

$$J^{-1}_{11} = \frac{s_{1x}}{\sqrt{(l_1^2 - s_{1x}^2)}}, J^{-1}_{21} = \frac{s_{2x}}{\sqrt{(l_2^2 - s_{2x}^2)}}, J^{-1}_{31} = \frac{s_{3x}}{\sqrt{(l_3^2 - s_{3x}^2)}}, J^{-1}_{41} = 0, J^{-1}_{51} = 0$$

$$J^{-1}_{12} = -sin(a), J^{-1}_{22} = -sin(a), J^{-1}_{32} = -sin(a), J^{-1}_{42} = -cos(a), J^{-1}_{52} = 0$$

$$J^{-1}_{13} = cos(a), J^{-1}_{23} = cos(a), J^{-1}_{33} = cos(a), J^{-1}_{43} = -sin(a), J^{-1}_{53} = 0$$

$$J^{-1}_{14} = -y^w cos(a) - z^w sin(a) - h_2 sin(a), J^{-1}_{24} = -y^w cos(a) - z^w sin(a) - h_2 sin(a),$$

$$J^{-1}_{34} = -y^w cos(a) - z^w sin(a) - h_2 sin(a), J^{-1}_{44} = y^w sin(a) - z^w cos(a) - h_2 cos(a), J^{-1}_{54} = -1$$

$$J^{-1}_{15} = r cos(b) - t sin(b) + \frac{s_{1x}}{\sqrt{(l_1^2 - s_{1x}^2)}}(r sin(b) + t cos(b)),$$

$$J^{-1}_{25} = -r cos(b) - t sin(b) - \frac{s_{2x}}{\sqrt{(l_2^2 - s_{2x}^2)}}(r sin(b) - t cos(b)),$$

$$J^{-1}_{35} = -(t+p) sin(b) + \frac{s_{3x}}{\sqrt{(l_3^2 - s_{3x}^2)}}(t+p) cos(b), J^{-1}_{45} = 0, J^{-1}_{55} = 0$$

Dimension

$w_1 = 0.2975m$, $w_2 = 0.3075m$, $w_3 = 0.1575m$

$l_1 = 0.4m$, $l_2 = 0.4m$, $l_3 = 0.475m$

$h_1 = 0.1m$, $h_2 = 0.1m$

$t = 0.15m$, $r = 0.095m$, $p = 0.095m$